Civil Engineering and Applied Solutions

Research Article

journal homepage: ceas.journals.umz.ac.ir

CEAS Civil Engineering and Applied Solutions

Numerical Investigation of Fe-SMA Strengthened Masonry Walls under Lateral Loading

Moein Rezapour [a], Mehdi Ghassemieh [a*]

[a] *College of Engineering, School of Civil Engineering, University of Tehran, Tehran, Iran*

ARTICLE INFO

Keywords:
Masonry wall
Shape memory alloy
Post-tensioning
Iron-based

Article history:
Received 02 July 2025
Accepted 27 July 2025
Available online 01 September 2025

ABSTRACT

This study explores the application of Fe-based shape memory alloys (Fe-SMAs) for the seismic strengthening of unreinforced masonry (URM) walls. Due to their unique thermomechanical behavior and cost-effectiveness, Fe-SMAs offer a promising alternative to traditional reinforcement materials. Using Abaqus finite element software, numerical models were developed and validated against experimental results to examine the structural performance of masonry walls reinforced with Fe-SMA strips. Three reinforcement configurations were investigated: vertical, V-shaped, and Λ-shaped layouts, each subjected to different levels of post-tensioning stress ranging from 100 MPa to 400 MPa. The results revealed a substantial improvement in lateral resistance and stiffness across all models. The vertically reinforced walls exhibited the highest gains, with up to a 96% increase in base shear resistance. V-shaped and Λ-shaped reinforcements also showed significant enhancements, mainly due to the bracing effect of the inclined SMA strips. While the failure mode remained primarily diagonal shear in all cases, the introduction of post-tensioning delayed crack initiation and improved energy dissipation capacity. The frictional interaction between the SMA strips and masonry units, augmented by the post-tensioning force, was identified as a key factor in enhancing performance. This study demonstrates that Fe-SMA reinforcement is a viable, innovative technique for retrofitting masonry walls, especially in earthquake-prone regions. The ease of installation, combined with the ability to apply force through thermal activation, makes Fe-SMAs a highly practical solution for improving the safety and resilience of existing masonry structures.

1. Introduction

Masonry materials are among the oldest building materials used in construction. Their abundance, compatibility with most climatic conditions, lack of need for specialized labor during construction, durability, and long-lasting properties are some of the reasons why these materials have continuously been favored in building projects. A large portion of the buildings worldwide are constructed with masonry materials. However, the understanding and knowledge of structural engineers regarding the behavior of such structures are still insufficient, and further research is necessary to accurately understand the behavior of masonry as a structural material. This need is especially felt in countries located on seismic belts, where residents of masonry buildings have suffered irreparable damage in recent earthquakes. Since a significant portion of the world's population lives in these types of structures, finding methods to enhance the resistance of masonry buildings is extremely important.

Recent earthquakes have tragically demonstrated the vulnerability of unreinforced masonry (URM) buildings. For example, during the 2023 Türkiye–Syria earthquake, more than 50,000 people were killed, and over 200,000 buildings were either destroyed or severely damaged, many of which were URM structures. Similarly, in the 2017 Mexico City earthquake, approximately 60% of the collapsed structures were unreinforced masonry buildings. These catastrophic events underscore the urgent need for reliable

* Corresponding author.
E-mail addresses: m.ghassemieh@ut.ac.ir (M. Ghassemieh).

https://doi.org/10.22080/ceas.2025.29594.1022
ISSN: 3092-7749/
How to cite this article: Rezapour, M., Ghassemieh, M. Numerical Investigation of Fe-SMA Strengthened Masonry Walls under Lateral Loading. Civil Engineering and Applied Solutions. 2025; 1(4): 1–15. doi:10.22080/ceas.2025.29594.1022.

seismic retrofitting techniques. Therefore, developing effective and economical solutions, such as the application of Fe-based Shape Memory Alloys (Fe-SMAs), is crucial to improving the resilience of existing masonry infrastructure in earthquake-prone regions.

Understanding the behavior of masonry structures for their strengthening is an inevitable process. Therefore, many studies have been conducted on these structures. Maheri et al. [1], in their experimental research, they demonstrated that the use of a head mortar can lead to increased shear strength and wall out-of-plane stiffness. Similar results were also observed by Nateghi and Alemi [2], based on the effect of head mortar on wall behavior through laboratory tests. Griffith et al. [3] examined the out-of-plane behavior of masonry walls under lateral loads in their studies. They subjected eight unreinforced masonry walls to cyclic static out-of-plane loading. Their observations showed that increasing axial load resulted in less resistance drop in the wall, and this was consistent across all walls. ElGawady et al. [4] demonstrated, based on their experimental tests, that the type of mortar significantly influences the wall's resistance, crack pattern, and ductility. According to experiments by Gouveia and Lourenço [5], the use of reinforcement mesh for unifying the masonry wall can increase the lateral resistance and ductility of the unreinforced masonry wall by up to 30%. Petry and Beyer [6], in a study aimed at providing necessary data to improve numerical models of unreinforced masonry walls, investigated the effect of boundary conditions on masonry wall behavior. They subjected six unreinforced masonry walls with clay units and cement mortar to cyclic loading. Wang et al. [7] studied the effect of reinforcement mesh on masonry walls with openings. Their findings indicated that openings reduce the confinement effect of the reinforcement mesh; however, using reinforcement results in more continuous and ductile behavior compared to unreinforced walls. ElGawady et al. [8] used FRP strips for the seismic retrofit of an unreinforced masonry wall. They applied the FRP strips in a cross pattern to improve the wall's behavior and observed that while the initial stiffness of the retrofitted wall was similar to that of a regular wall, the failure mode shifted from shear to bending, making the wall more ductile. Shabdin et al. [9] found that walls equipped with concrete overlays exhibit relatively high energy dissipation capacity, and their cyclic behavior shows less buckling effect. Various methods have been introduced for strengthening masonry structures. One of these methods involves increasing the axial load applied to masonry walls. In this approach, the structural resistance of the wall is enhanced by increasing the applied axial load. This increase can be achieved through post-tensioning of the wall [10].

According to Sadeghi Marzaleh [11] research, increasing the axial load on a wall can enhance its shear resistance while reducing its displacement capacity. He also observed that excessive compressive stress induced by post-tensioning might change the failure mode from shear to diagonal cracking. This increase in axial load can be applied to the wall using post-tensioning elements such as steel tendons or rebars. Various methods and materials have been introduced for the post-tensioning of masonry walls. Schultz and Scolforo [12] studied the effect of post-tensioning on the out-of-plane behavior of masonry walls subjected to wind loads. They observed that applying post-tensioning significantly improves the wall's resistance to wind loads perpendicular to its plane. Kohail et al. [13] investigated the effect of post-tensioning on a specific type of masonry shear wall made of concrete blocks. Their research mainly focused on how post-tensioning influences the failure mode, permanent deformation, energy dissipation capacity, stiffness, and ductility of masonry walls. Soltanzadeh et al. [14] examined the effect of post-tensioning on shear walls made of confined masonry. Their studies indicated that masonry walls equipped with confined post-tensioning systems exhibit good ductility. Hassanli conducted extensive research on the performance factors of post-tensioned masonry structures [15-18]. To accurately assess this, he proposed modeling methods aimed at predicting the seismic behavior of these post-tensioned walls. The results showed that the numerical models were reasonably accurate, and using these models, they could derive factors for the performance analysis of post-tensioned masonry walls. Laursen and Ingham [19] conducted a study to establish appropriate seismic design criteria for post-tensioned masonry structures. Most of their research focused on the effects of post-tensioning with unbonded tendons on in-plane behavior. Quiroz [20] studied the seismic performance of four historic masonry towers reinforced with unbonded AFRP tendons. Babatunde [21] tested different reinforcement methods on unreinforced masonry walls. One of these methods, which showed a good response to lateral loads, was post-tensioning the wall using FRP materials. Seim et al. used FRP for localized post-tensioning in masonry materials and demonstrated that applying post-tensioning at points with the highest damage potential can significantly improve the seismic behavior of masonry walls [22].

In this article, shape memory alloys are used for the purpose of wall strengthening in buildings. The proposed alloy is iron-based, which is more economical compared to other alloys. These alloys can generate a significant amount of post-tensioning force through heat absorption. Therefore, many researchers have studied this property of shape memory alloys.

Hong et al. [23] researched evaluating the recovery behavior of iron-based shape memory alloys (Fe-SMA) under various constraints. Choi et al. [24] investigated the effect of prestressing embedded Fe-SMA wires on the flexural behavior of mortar beams. Experimental data indicated that the prestressing force could reduce the resulting stress by approximately 28% in both tensile and compressive parts of the mortar beams. Shahverdi et al. [25-27] examined the feasibility of using a form of Fe-SMA that is economically advantageous for post-tensioning concrete beams. Izadi et al. [28-31] also explored the potential of using the reversibility property of these alloys in metal strips and a steel bridge. Rezapour et al. [32] investigated the potential application of these alloys in structural walls. They modeled the walls at a macroscopic scale and bonded SMA strips to the walls. Based on the results obtained, these alloys significantly increased the energy dissipation capacity of the walls.

Prestressing in structural walls is primarily applied in the vertical direction. Implementing prestressing diagonally in building walls is rarely done due to construction difficulties. Shape memory alloy strips, owing to their unique behavior and simple installation method, enable the possibility of diagonal prestressing of building walls. Therefore, in this study, walls with prestressed materials are examined both in the vertical and diagonal orientations under various load distribution levels. To achieve this, a masonry wall was modeled using Abaqus software, and the results were validated against experimental data. These models incorporated iron-based prestressed strips subjected to both vertical and diagonal prestressing. The results of these analyses, in terms

of performance and failure modes, were compared with each other.

2. Fe-based shaped memory alloys

Fe-based shape memory alloys are innovative materials distinguished by their unique properties among various alloys. These alloys can revert to their original shape upon absorption of a certain amount of heat. To date, various types of shape memory alloys have been discovered and developed. Among these, iron-based alloys constitute a specific category, with the primary element in their atomic structure.

From an economic perspective, these alloys are more cost-effective compared to other shape memory materials and can be utilized in generating residual stresses within civil engineering structures. The process of inducing residual stress in these alloys involves several steps: initially, a significant deformation is applied; this is followed by imposing specific boundary conditions; and finally, the alloy is heated. Upon heating, the alloy tends to regain its original shape; however, the boundary conditions inhibit this transformation. As a result, depending on the extent of the deformation, boundary conditions, and the temperature applied, residual stresses develop within the alloy. This process is illustrated in Fig. 1, which depicts the step-by-step progression.

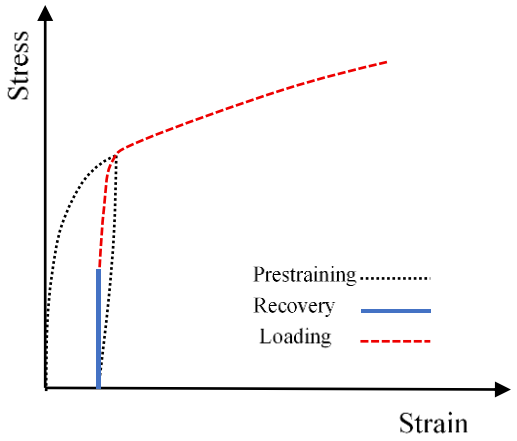

Fig. 1. Stress-strain curve of activated Fe-SMA.

Generally, these materials possess two distinct atomic structures: austenite and martensite (Fig. 2). These structures can be interconverted through the application of temperature and/or stress. The shape memory behavior in Fe-SMAs arises from the stress-induced transition of martensite from the parent γ-austenite phase to the ε-martensite phase at lower temperatures. The reverse transformation, from martensite back to austenite, occurs exclusively at elevated temperatures [33].

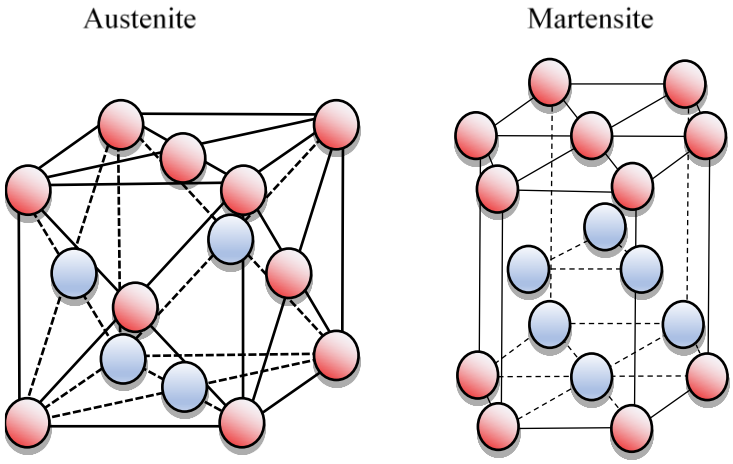

Fig. 2. Phase transformation of the Fe-based SMA.

3. Model description

In this paper, data and results from the experimental studies conducted Vermeltfoort et al. [34] on masonry walls are utilized. In the aforementioned experimental research, the masonry wall was subjected to in-plane lateral loading. The dimensions of the studied wall are 990 mm in length, 1140 mm in height, and 100 mm in thickness. The wall consists of 18 rows of clay bricks, each having a length of 210 mm, a height of 52 mm, and a thickness of 100 mm. The mortar thickness is 10 mm, and the mix ratio of cement, lime, and sand is 1:2:9. In the experimental model, a steel beam and foundation were used. However, since in this study, the masonry wall needs to be reinforced with SMA strips, which are connected to the concrete, an elastic beam and foundation with dimensions of 900×100×100 mm were used instead of the steel beam and foundation. A uniform vertical load of 0.3 MPa is applied at the top of the beam. This load remains constant throughout the loading process and simulates the weight of the upper floor. The lateral load is applied to the masonry wall in a monotonic, in-plane manner (Fig. 3).

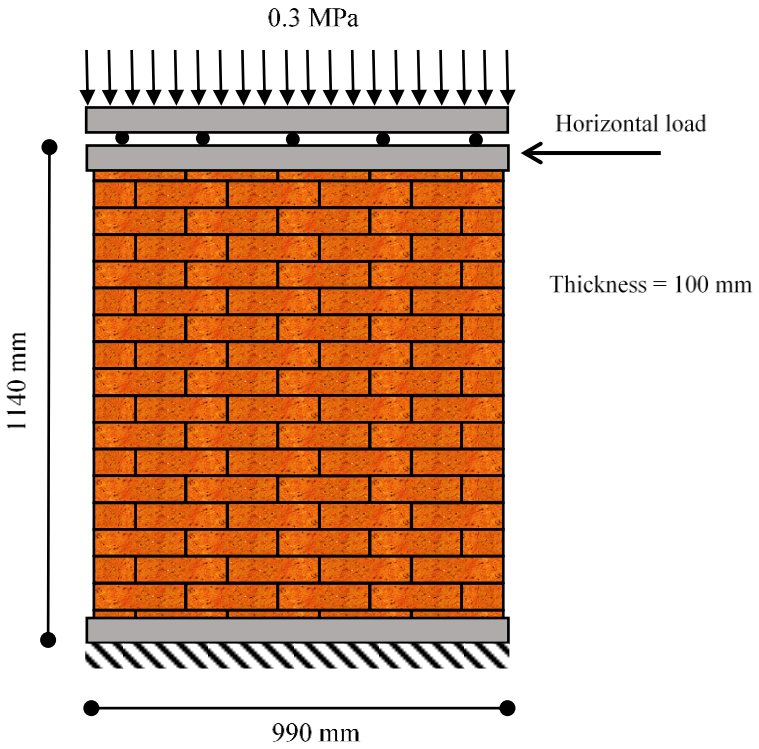

Fig. 3. Geometric characteristics of the masonry wall.

4. Modeling

Modeling of a masonry structure can be performed using three different methods. The first method is called Detailed Micro-modeling (Fig. 4a), which provides the highest level of accuracy. In this approach, the masonry units (bricks) and the mortar between them are fully modeled. Since all the parameters of the masonry wall are considered in this modeling technique, the resulting numerical model has a large stiffness matrix, leading to a significantly long analysis time [35].

The second method is known as Simplified Micro-modeling (Fig. 4b), which has lower accuracy compared to the first method but still maintains an acceptable level of precision. In this approach, the masonry units are modeled larger than their actual size. The increase in size corresponds to the thickness of the mortar joints between the bricks. The mortar is not directly modeled in this method; instead, its mechanical behavior is represented through the interaction between adjacent bricks. By omitting the mortar elements, the size of the stiffness matrix is reduced compared to the first method, which significantly decreases the required analysis time [35].

While both the Detailed Micro-model and Simplified Micro-model approaches are suitable for modeling a single masonry wall, they become very time-consuming when used for modeling an entire masonry structure. In large structures, the Macro-modeling approach is typically used (Fig. 4c). Although this method is less accurate than the other two, it offers much faster analysis times. In Macro-modeling, the entire masonry structure is represented as a homogeneous material similar to concrete. Despite its lower accuracy, this method provides relatively acceptable results when modeling large-scale masonry structures. In general, macro-modeling methods require less computational time compared to other techniques [36].

(a) **(b)** **(c)**

Fig. 4. Modeling of a masonry wall: (a) Detailed micro, (b) Simplified micro, and (c) Macro.

In this study, the effect of post-tensioning on masonry walls is investigated. Since the model involves only a single masonry wall with limited dimensions, the Simplified Micro-modeling method is employed for the numerical modeling of the target masonry wall.

4.1. Modeling of masonry units

As previously mentioned, in the Simplified Micro-modeling approach, the dimensions of masonry units are increased by an amount equal to the thickness of the mortar joints. This expansion eliminates the need to model mortar elements explicitly, and instead, the behavior of the mortar is incorporated into the model through interaction mechanisms assigned between the masonry units.

Since masonry units are brittle materials, the Concrete Damage Plasticity (CDP) model is used to simulate their behavior. The Damage Plasticity Model is based on the hardening and softening behavior of quasi-brittle materials such as concrete and rock masses. It is widely applied in the general analysis of quasi-brittle materials under dynamic or cyclic loading conditions. These types of materials typically exhibit brittle behavior under various loading scenarios. In such cases, the primary failure mechanisms are cracking under tension and crushing under compression [37].

One of the most important features of the CDP model is its ability to distinguish between tensile and compressive yield strengths and to account for stiffness degradation during cyclic and dynamic loading, based on concrete damage parameters. The plasticity model described in this section was initially proposed by Lubliner and later extended by Lee and Fenves. The foundation of this model is based on two main failure mechanisms in concrete: tensile cracking and compressive crushing [37, 38].

In Abaqus software, the Concrete Damage Plasticity (CDP) model is widely employed to simulate damage in concrete structures. This model captures the irreversible degradation of stiffness in brittle materials due to mechanical loading. Stiffness degradation is characterized using two damage parameters: tensile damage (d_t) and compressive damage (d_c).

Fig. 5 illustrates the axial stress–strain behavior of concrete under both tension and compression. In this figure, the material stiffness during loading is reduced by factors of (1−dt) and (1−dc) for tension and compression, respectively. The variables ε_t^{in} and ε_c^{in} represent the inelastic tensile and compressive strains in the undamaged state, while ε_t^{pl} and ε_c^{pl} denote the corresponding plastic strains in the damaged state.

Eqs. 1 and 2 define the relationships between these strain components.

$$\varepsilon_c^{pl} = \varepsilon_c^{in} - \frac{d_c\,\sigma_c}{(1-d_c)E_0} \tag{1}$$

$$\varepsilon_t^{pl} = \varepsilon_t^{ck} - \frac{d_t\,\sigma_t}{(1-d_t)E_0} \tag{2}$$

where, σ_c and σ_t are compressive and tensile stress at any point.

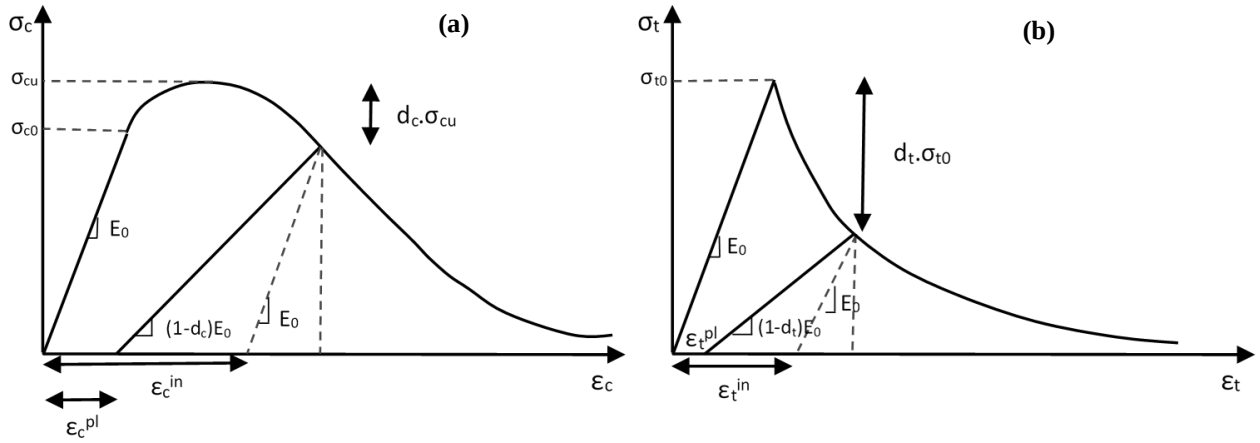

Fig. 5. Stress-strain relationship for CDP model: (a) in compression, and (b) in tension [37].

To simulate the nonlinear behavior of bricks, a constitutive law is required to describe the stress–strain relationship. In this study, it is assumed that the behavior of clay brick is similar to that of low-strength concrete.

The monotonic envelope curve of concrete in compression follows the modified Kent and Park concrete model, which offers good accuracy and simplicity, and has been published by Mander et al. [39]. The formulations of the stress-strain relations of unconfined concrete based on the modified Kent and Park model are summarized here.

The constitutive model consists of an ascending branch represented by a second-degree parabolic curve and a descending linear part. The ascending parabola is expressed by the following equation:

$$f_c = k f'_c \left[\frac{2\varepsilon_c}{\varepsilon_0 k} - \left(\frac{\varepsilon_c}{\varepsilon_0 k}\right)^2\right] \qquad \varepsilon_c \le k\varepsilon_0 \tag{3}$$

where ε_c is the longitudinal concrete strain, f'_c is the compressive strength of concrete. The compression strength of the brick is also assumed to be 15 MPa. ε_0 is the strain of unconfined concrete corresponding to f'_c, and k is a confinement coefficient greater than or equal to 1. Since no confinement is considered for the bricks in the masonry wall modeling, the value of k is assumed to be

equal to one.

For strain greater than the value corresponding to the peak stress, the softening branch of the stress-strain relationship is approximated by a straight line having the equation:

$$f_c = kf'_c[1 - Z_m(\varepsilon_c - \varepsilon_0 k)] \qquad \varepsilon_c > k\varepsilon_0 \tag{4}$$

where Z_m is the strain softening slope and can be calculated by:

$$Z_m = \frac{0.5}{\left[\left(\frac{3 + 0.29f'_c}{145f'_c - 1000}\right) - \varepsilon_0 k\right]} \tag{5}$$

In the tensile regime, the material behavior is simulated using an equation proposed by Selby and Vecchio [40]. According to this equation, the response remains linear up to the peak tensile stress, after which softening behavior occurs in the material.

$$f_t = \frac{f'_t}{1 + \sqrt{200\varepsilon_t}} \qquad \varepsilon_t > \varepsilon_{ct} \tag{6}$$

where ε_t is the longitudinal concrete strain in the tension part, the tensile strength (f'_t) of the brick is also assumed to be 2 MPa. Since the Simplified Micro-modeling approach is used in this study, the dimensions of the masonry units are larger than their actual size. A_s a result, the stiffness of the expanded units differs from that of the original masonry units. To compensate for this discrepancy, the elastic modulus assigned to the expanded units is adjusted and differs from the actual value.

For this purpose, Eq. 7 is proposed based on the assumption of a stack bond between masonry units and uniform stress distribution in masonry constituents. It is presented as:

$$E_{adj} = \frac{HE_uE_m}{nh_uE_m + (n-1)h_mE_u} \tag{7}$$

where H is the height of the masonry assemblage, E_u and E_m are the elastic modulus of unit and mortar, respectively, h_u and h_m are the height of the masonry unit and mortar, and n is the number of courses in a masonry assemblage.

4.2. Mortar modeling

To model the mortar, the surface-based cohesive behavior model is employed. In this approach, the mortar is completely removed from the model, and its mechanical behavior is simulated through interaction definitions. This model consists of both linear and nonlinear regimes and accounts for behavior in three directions: one normal (axial) direction and two shear directions (Fig. 6).

The behavior of the mortar is described using stress–separation relationships, as illustrated in Fig. 7. The shear behavior in the two perpendicular directions is assumed to be approximately similar.

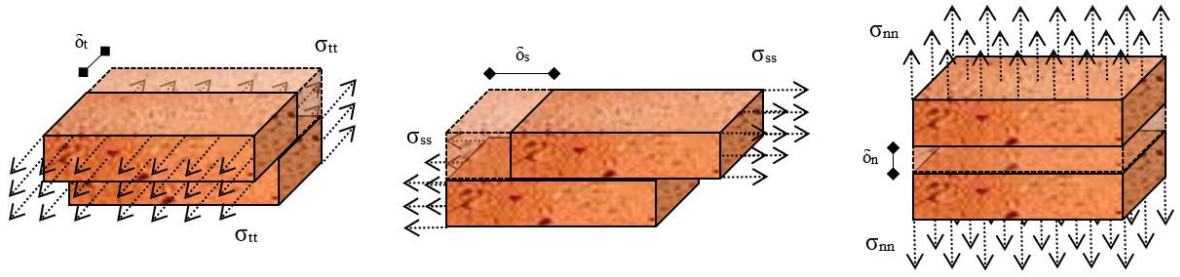

(a) **(b)** **(c)**

Fig. 6. Linear behavior in interaction: (a) shear in plane, (b) shear perpendicular to the plane, and (c) axial.

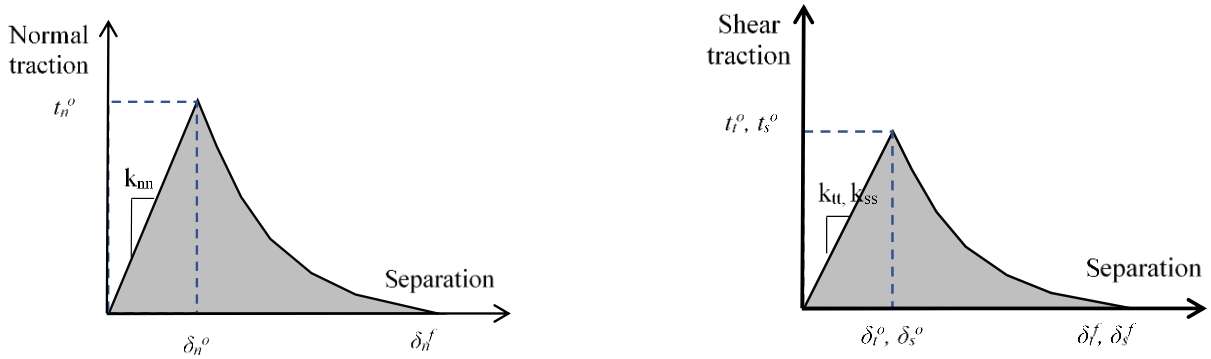

Fig. 7. Nonlinear shear and axial behavior of mortar.

The initial behavior at the joint interfaces is defined as linear stresses based on the amount of relative displacement. This behavior is represented by an elastic stiffness matrix. Eq. 8 presents the relationship between the displacement vector and the stress.

$$\begin{bmatrix} t_n \\ t_s \\ t_t \end{bmatrix} = \begin{bmatrix} k_{nn} & 0 & 0 \\ 0 & k_{ss} & 0 \\ 0 & 0 & k_{tt} \end{bmatrix} \begin{bmatrix} \delta_n \\ \delta_s \\ \delta_t \end{bmatrix} \tag{8}$$

in this context, t_n, t_s, and t_t represent the normal stress and the two mutually perpendicular shear stresses, respectively, while δ_s, δ_n, and δ_t correspond to the relative normal displacement and the two perpendicular relative shear displacements. k_{nn}, k_{ss}, and k_{tt} are the components of the stiffness matrix. If only the stiffness of the mortar is considered in the modeling, the components of the stiffness matrix are solely functions of the mortar's stiffness and dimensions. However, since the simplified masonry micro-model is used in this study, the stiffness of the expanded bricks also affects the components of this stiffness matrix.

So, the equivalent stiffness for joint interfaces is expressed as a function of the mortars and unit's moduli of elasticity, and the thickness of the mortar.

$$k_{nn} = \frac{E_u E_m}{h_m(E_u - E_m)} \tag{9}$$

$$k_{ss} = k_{tt} = \frac{G_u G_m}{h_m(G_u - G_m)} \tag{10}$$

where h_m is the thickness of the mortar, and E_u and E_m are the Young's moduli of the masonry unit and the mortar, respectively. Similarly, G_u and G_m represent the shear moduli of the masonry unit and the mortar, respectively. The initial linear response of the joints is followed by crack propagation. When the damage initiation criterion is achieved based on the user-defined tractions between the masonry interfaces, i.e., shear and tensile strength of the joints, cracking propagates in the masonry joints.

The damage initiation criterion can be defined based on either separation or stress, each of which includes two types of damage initiation criteria. In this study, the stress-based criterion is used for damage initiation. The stress criterion includes the Maximum Stress Criterion and the Quadratic Stress Criterion. These two damage initiation criteria are presented in Eqs. 11 and 12, respectively.

$$max\left\{\frac{t_n}{t_n^0}, \frac{t_t}{t_t^0}, \frac{t_s}{t_s^0}\right\} = 1 \tag{11}$$

$$\left[\frac{t_n}{t_n^0}\right]^2 + \left[\frac{t_t}{t_t^0}\right]^2 + \left[\frac{t_s}{t_s^0}\right]^2 = 1 \tag{12}$$

in these equations, t_n^0, t_t^0, and t_s^0 represent the maximum normal stress and the two orthogonal shear stresses, respectively. In both criteria, t_n is always considered positive, since compressive stress cannot cause cracking in the joint interface. These two criteria are represented in Fig. 8. In this study, the Quadratic Stress Criterion is used for damage initiation.

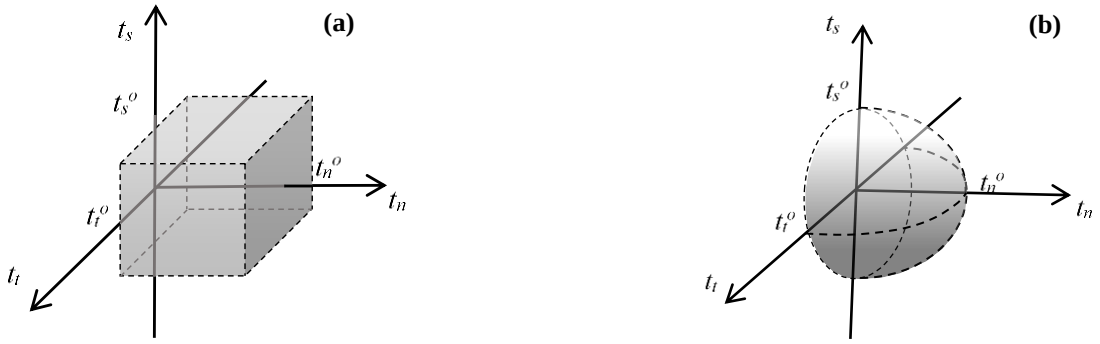

Fig. 8. Criterion for the onset of nonlinear behavior of mortar: (a) cubic, and (b) quadratic.

After reaching the maximum stress in shear and tension, the nonlinear behavior exhibits softening. This softening behavior is defined in the software using an exponential function. In this range, damage (cracking) propagates within the interface, leading to a reduction in stiffness. This stiffness degradation is incorporated into the constitutive equation according to the following relation.

$$\begin{bmatrix} t_n \\ t_s \\ t_t \end{bmatrix} = (1 - D) \begin{bmatrix} k_{nn} & 0 & 0 \\ 0 & k_{ss} & 0 \\ 0 & 0 & k_{tt} \end{bmatrix} \begin{bmatrix} \delta_n \\ \delta_s \\ \delta_t \end{bmatrix} \tag{13}$$

in the above equation, D is the damage variable, with a value ranging between 0 and 1. A value of 0 indicates no damage in the interface, while a value of 1 signifies that the interface is fully damaged and can no longer transfer shear or tensile stresses.

5. Numerical model

Based on the information presented in the previous sections, the simplified micro-model consists of two main components. The first component is the expanded masonry units. These units are larger than their actual size by the thickness of the mortar. Since the

masonry units are modeled in three dimensions, solid elements with 8 nodes and reduced integration (C3D8R) were used to simulate their behavior, with dimensions of 30 × 30 × 33 mm. The mechanical properties of the masonry unit are provided in Table 1.

Table 1. Mechanical specifications of the expanded masonry unit.

Linear behavior			Nonlinear behavior	
Elastic modulus of units (MPa)	**Poisson's ratio**	**Adjusted elastic modulus of the expanded unit (MPa)**	**Tensile strength (MPa)**	**Compressive strength (MPa)**
16700	0.15	4050	2	15

To define the interaction between the masonry elements, four parameters were used: tangential behavior, normal behavior, cohesive behavior, and damage. When surfaces come into contact, they typically transmit both shear and normal forces across their interface. A relationship usually exists between these two force components. This relationship, referred to as tangential behavior between the contacting bodies, is commonly described in terms of the stresses at the interface. The friction coefficient for the tangential behavior was assumed to be 0.75.

The distance between two surfaces is referred to as the clearance. In Abaqus, the contact constraint is enforced when the clearance between the two surfaces becomes zero. There is no limit in the contact formulation regarding the magnitude of contact pressure that can be transmitted between the surfaces. The surfaces separate when the contact pressure becomes zero or negative, at which point the constraint is removed. This type of normal behavior, known as hard contact, is used to define the contact interaction. The Cohesive behavior and Damage parameters represent the linear and nonlinear behavior of the mortar. The detailed specifications of these parameters are provided in Table 2.

Table 2. Mechanical specifications of the mortar.

Linear behavior				Nonlinear behavior			
Elastic modulus of mortar (MPa)	**K_{nn} (N/mm^3)**	**K_{ss} (N/mm^3)**	**K_{tt} (N/mm^3)**	**Maximum tensile stress (MPa)**	**G_{IC} (N/mm)**	**Cohesion (MPa)**	**G_{IIC} (N/mm)**
780	82	36	36	0.25	0.18	0.35	0.125

In Fig. 9, the numerical model is shown. As illustrated in the figure, to apply boundary conditions, the bottom of the wall footing is fully restrained in all three orthogonal directions. A distributed load of 0.3 MPa is applied to the top of the beam, and a lateral load is applied to the top of the beam using a displacement-controlled approach. To validate the model, two parameters are compared with the experimental results: base shear and failure mode.

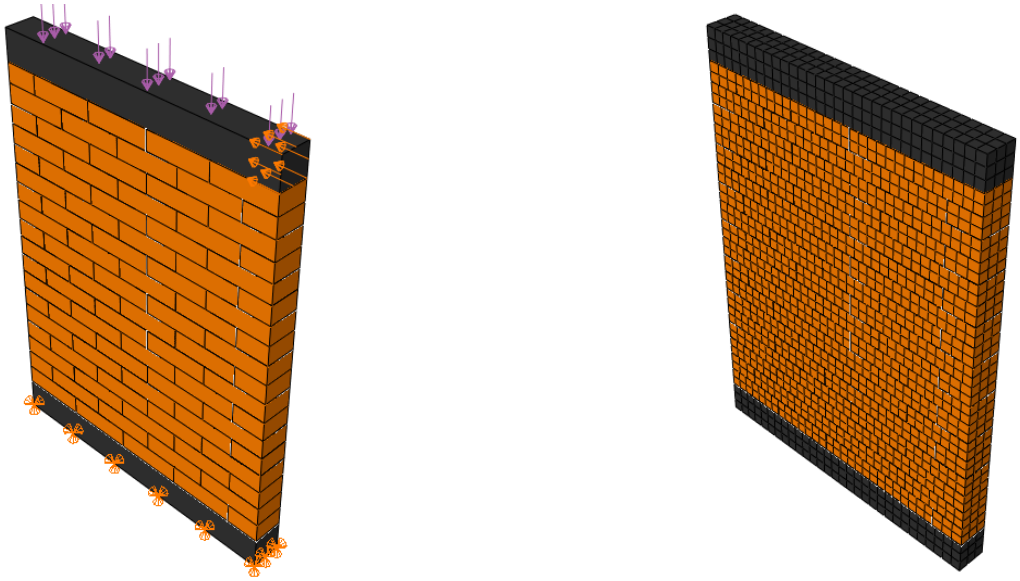

Fig. 9. Numerical model with meshing and boundary conditions.

Fig. 10 presents the base shear diagram under monotonic loading, which demonstrates a reasonable agreement between the numerical and experimental models. This figure also shows the failure modes of the numerical and experimental masonry walls. As illustrated, the failure mode in both cases is shear-diagonal, indicating that the numerical wall successfully replicates the behavior observed in the experimental model.

To investigate sensitivity, the numerical wall was modeled using meshes of various sizes: 20, 30, 40, and 50 mm. Fig. 11 presents the base shear diagrams corresponding to the different mesh sizes. As seen in the figure, smaller mesh sizes result in more converged base shear responses. Since the wall modeled with a 30 mm mesh provides a good balance between computational efficiency and accuracy, this mesh size was chosen for the final modeling of the wall.

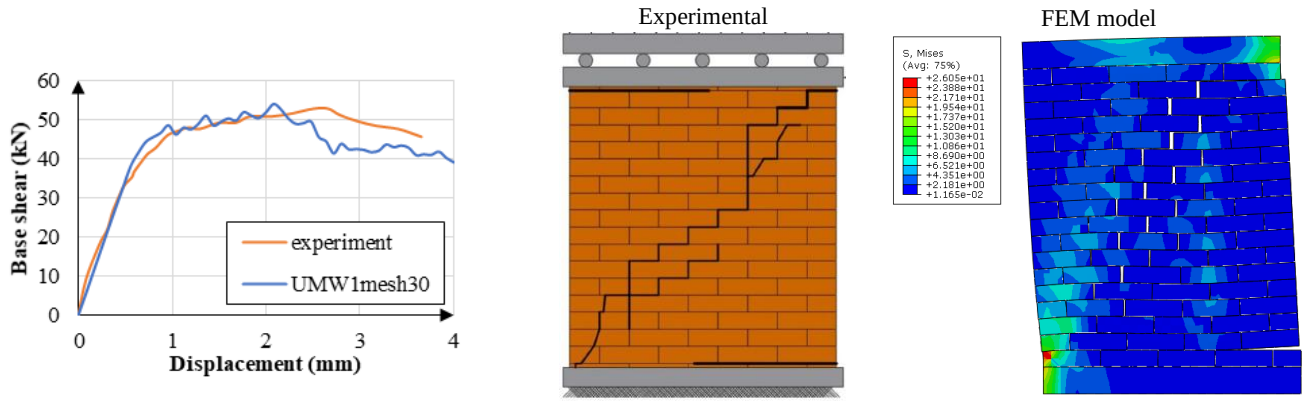

Fig. 10. Base shear diagram and the failure mode.

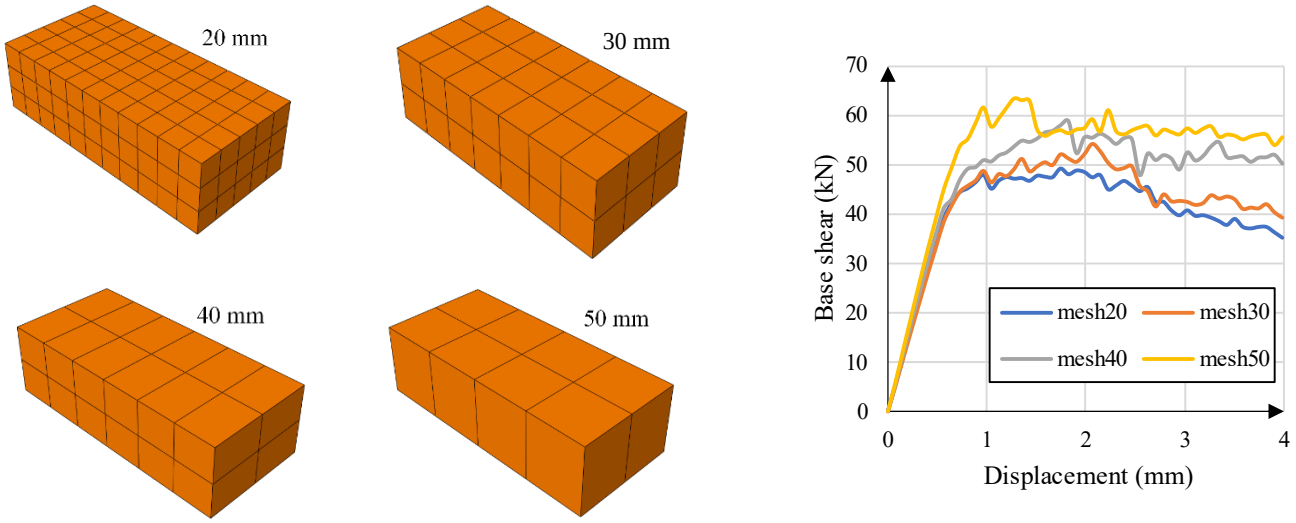

Fig. 11. Sensitivity of the numerical model based on different mesh dimensions.

In this study, Fe-SMA strips were used to investigate the effect of post-tensioning on masonry walls. These strips are made of Fe-SMA with 1.5 mm thickness and a width of 120 mm. The modulus of elasticity and yield stress in this type of alloy are 165 GPa and 400 MPa, respectively, and the austenite onset temperature is approximately 180 degrees Celsius. This type of Fe-based alloy must be heated to 160 °C to create post-tension stress. Because these materials are highly electrically resistant, the alloy's temperature can be easily increased as needed by the electric current. In the numerical modeling of SMA strips, shell elements are used. These elements are of the 4-node type, and tie interaction is used to connect them to the wall body. With this method, the modeling level is less complex and the model faces fewer errors analytically.

6. Results of numerical models

In this study, three numerical models were developed to improve the behavior of the masonry wall. The first model, as shown in Fig. 12a, utilized vertical strips to strengthen the wall. The second and third models, depicted in Fig. 12, employed SMA strips in V-shaped and Λ-shaped configurations, respectively.

Since the level of post-tensioning stress in iron-based alloys can vary depending on boundary and operational conditions, this research considered post-tensioning stress levels of 100 MPa, 200 MPa, 300 MPa, and 400 MPa to analyze their effects on the masonry wall. The models were subjected to monotonic lateral loads. The primary aim was to evaluate how different reinforcement strategies and post-tensioning stress levels impact the structural response of the wall under lateral loading. The results obtained from these three models were then compared to each other to determine the most effective reinforcement method for enhancing the stability and ductility of the masonry wall.

This comparative analysis provides valuable insights into the behavior of reinforced walls under seismic or other lateral forces, helping structural engineers optimize design strategies for safer, more resilient buildings. The use of SMA strips can significantly enhance the behavior and lateral resistance of masonry walls. This study evaluates the lateral strength of masonry walls reinforced with SMA strips, comparing them to conventional walls. Fig. 13 presents the resistance of these reinforced walls, illustrating the influence of the post-tensioning on their structural response. To facilitate analysis, the post-tensioned masonry walls are designated by the notation MW-Ve300, where "MW" stands for Masonry Wall, "Ve" indicates a vertical (perpendicular) orientation, and "300" reflects the level of post-tensioning stress in megapascals. The results demonstrate that as the degree of post-tensioning increases, the lateral resistance of the wall also increases. Consequently, all post-tensioned masonry walls exhibit higher lateral resistance

compared to normal, non-post-tensioned walls. This phenomenon is primarily attributed to the coefficient of friction, which plays a crucial role in converting the applied vertical (post-tensioning) forces into lateral resistance. When the post-tensioning load acts vertically on the wall, this load is effectively transformed into lateral resistance via the frictional interaction between the masonry components and the SMA strips.

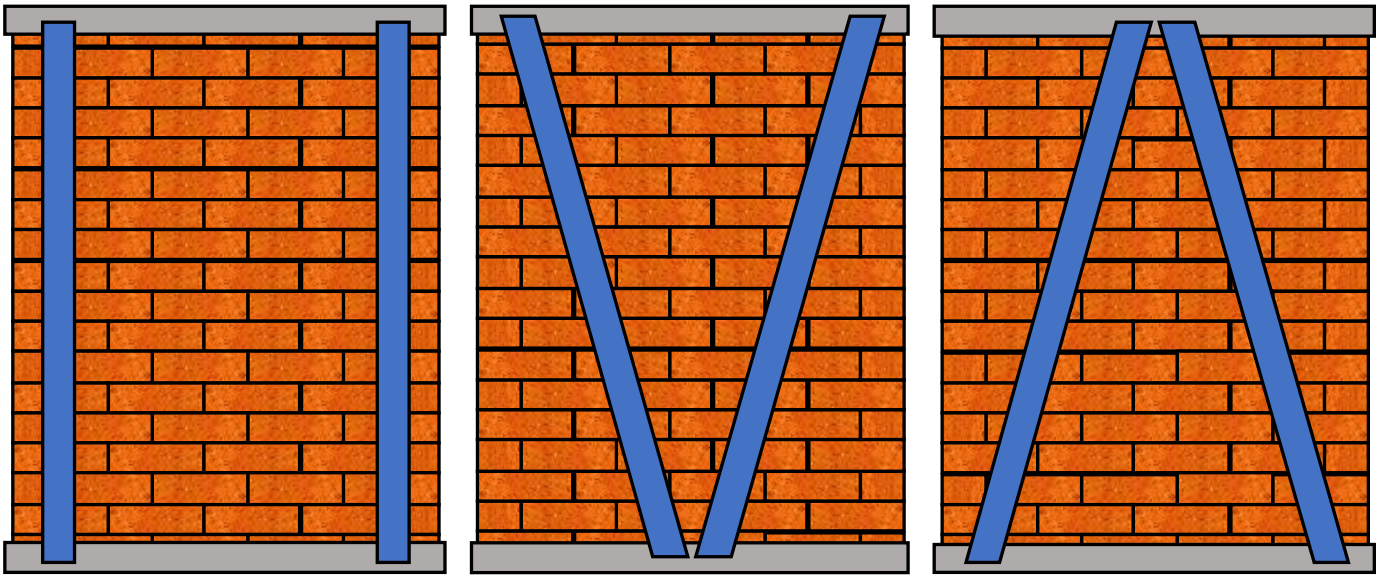

Fig. 12. Models reinforced with SMA strips: (a) Vertical, (b) V-shaped, and (c) Λ-shaped.

Specifically, as the level of post-tensioning stress increases, the coefficient of friction enhances, leading to a corresponding rise in the wall's lateral resistance. The measured lateral resistances for the MW-Ve100, MW-Ve200, MW-Ve300, and MW-Ve400 walls are 59.3, 68.1, 78.1, and 95.5 Newtons, respectively. These figures indicate that the lateral resistance of these walls improves by approximately 22%, 40%, 61%, and 96% compared to a baseline masonry wall without reinforcement. A key observation in this investigation is that the increase in resistance is not directly caused by the SMA strips themselves but is mediated through their effect on the frictional interaction. The SMA strips indirectly contribute to enhancing the resistance by increasing the effective coefficient of friction at the interface, thus facilitating the conversion of vertical post-tensioning into effective lateral resistance.

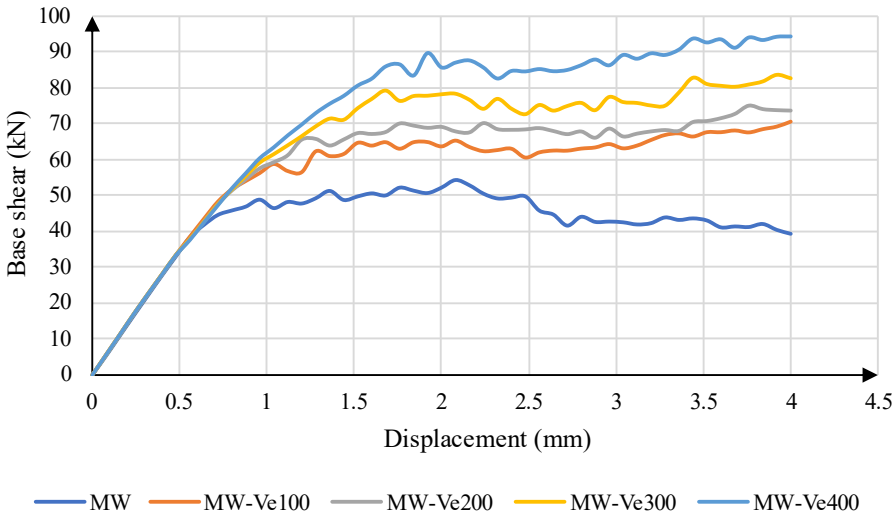

Fig. 13. Base shear of masonry walls reinforced with vertical strips.

Fig. 14 illustrates the base shear diagram for reinforced masonry walls with a V-shaped configuration. As depicted in the figure, the utilization of Shape Memory Alloy (SMA) strips has significantly enhanced the lateral resistance of the structural wall. Furthermore, the increase in applied post-tension within these SMA strips correlates with a corresponding rise in the wall's lateral resistance, indicating that higher post-tensioning levels contribute positively to the overall seismic performance of the structure. For analytical clarity, the post-tensioned masonry walls are designated by the notation MW-V300, where "MW" refers to Masonry Wall, "V" signifies the V-shaped reinforcement configuration, and "300" indicates the level of post-tensioning stress expressed in megapascals (MPa). An important observation derived from this figure is that two primary factors influence the enhancement of the wall's lateral resistance. First, in the case of purely vertical post-tensioning, the coefficient of friction between masonry units predominantly governs the resistance increase. Conversely, in the V-shaped wall configuration, beyond the frictional interactions between masonry units, the SMA alloys directly contribute to the lateral load resistance. It should be noted that these SMA strips are inclined rather than vertical; thus, they exert less vertical post-tensioning force compared to vertically reinforced walls. As a

result, the frictional contribution to lateral resistance in the V-shaped walls is relatively less significant. Nonetheless, due to the inclined orientation of the SMA strips, they can function similarly to braces, actively enhancing the overall stiffness and strength of the masonry wall against lateral loads. Experimental assessments of the lateral resistance capacities for the walls designated MW-V100, MW-V200, MW-V300, and MW-V400 are 57.3 N, 63.1 N, 70.2 N, and 77.5 N, respectively. These measurements demonstrate that the lateral resistance increases by approximately 14%, 26%, 40%, and 55%, respectively, compared to a baseline unreinforced masonry wall, highlighting the substantial beneficial effect of SMA reinforcement. Furthermore, the stiffness evaluation depicted in the figure indicates that models equipped with SMA reinforcement exhibit higher stiffness values than conventional walls. This improvement is primarily attributable to the inclined orientation of the SMA strips, which enhances the structural integrity and resilience of the masonry walls under lateral seismic forces.

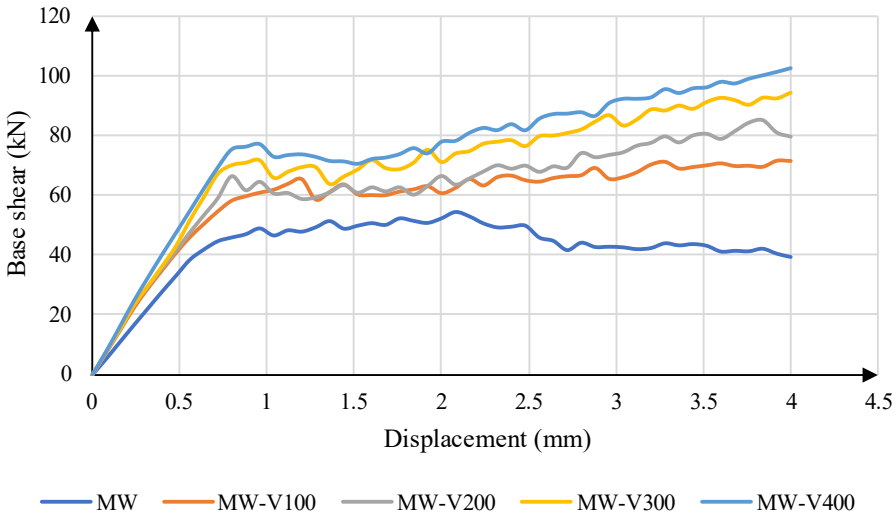

Fig. 14. Base shear of masonry walls reinforced with V-shaped strips.

Fig. 15 presents the base shear diagram for reinforced masonry walls with a Λ-shaped configuration. As shown in the figure, these SMA strips result in a corresponding enhancement of the wall's lateral capacity. This indicates that increasing the post-tension level directly contributes to improved seismic resistance, making the walls more capable of withstanding dynamic lateral loads. To facilitate a standardized analysis, the post-tensioned masonry walls are designated by the notation MW-Λ300, where "MW" signifies Masonry Wall, "Λ" indicates the Λ-shaped reinforcement configuration, and "300" denotes the level of post-tensioning stress, measured in megapascals (MPa).

A noteworthy aspect of this diagram is that two primary factors influence the enhancement of the wall's lateral resistance. First, in the case of purely vertical post-tensioning, the coefficient of friction between masonry units is predominantly responsible for increasing the resistance. However, in the Λ-shaped reinforced walls, in addition to the frictional interaction between masonry units, the SMA alloys play a direct role in resisting lateral forces. It is important to note that these SMA strips are installed in an inclined (non-vertical) orientation; thus, they exert less vertical post-tensioning force compared to purely vertical reinforcement. Consequently, the contribution of friction to the overall lateral resistance in Λ-shaped walls is comparatively reduced. Nonetheless, due to their inclined orientation, these SMA strips can act similarly to braces, actively contributing to the overall stiffness and strength of the masonry structure during seismic events. Experimental measurements of the lateral resistance for the walls designated as MW-Λ100, MW-Λ200, MW-Λ300, and MW-Λ400 are 62.4 N, 66.8 N, 73.2 N, and 80.5 N, respectively. These results demonstrate that the lateral resistance increases progressively by approximately 24%, 33%, 46%, and 61%, respectively, compared to a baseline masonry wall without reinforcement. This significant improvement underscores the effectiveness of incorporating SMA-based reinforcement strategies in enhancing seismic resilience. Furthermore, the data shown in the figure indicate that the stiffness of the models equipped with SMA reinforcement exceeds that of standard, unreinforced masonry walls. This increase in stiffness is primarily attributable to the inclined orientation of the SMA strips, which effectively enhances the structural integrity and load-bearing capacity of the walls under lateral seismic forces. Overall, the incorporation of inclined SMA strips in masonry walls demonstrates a promising approach for strengthening seismic performance.

Fig. 16 presents a schematic illustration of the failure mode of the masonry wall. Given that the failure mode of a typical unreinforced masonry wall predominantly occurs along a diagonal crack, the increase in vertical stress levels does not significantly alter the fundamental mode of failure. Instead, the failure mode remains primarily characterized by diagonal behavior along a diagonal plane, which is typical for such structural configurations. This observation indicates that, despite variations in prestressing, the mode of failure remains consistent, highlighting the inherent diagonal nature of conventional masonry walls under lateral loading conditions.

7. Conclusion

In this study, Fe-based Shape Memory Alloys (Fe-SMAs) were utilized as a strengthening material to improve the behavior of masonry walls subjected to lateral loading. The numerical models, validated against experimental data, demonstrated that Fe-SMA

strips significantly enhance the lateral resistance, stiffness, and ductility of masonry walls. These alloys, which possess the unique ability to return to their original shape upon heating, enable the application of post-tensioning forces both vertically and diagonally. This property is particularly valuable for seismic strengthening of unreinforced masonry structures.

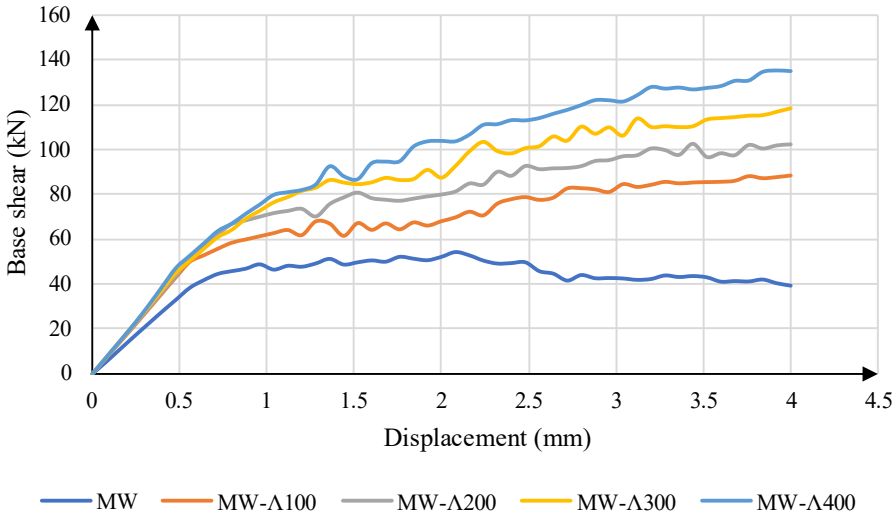

Fig. 15. Base shear of masonry walls reinforced with Λ-shaped strips.

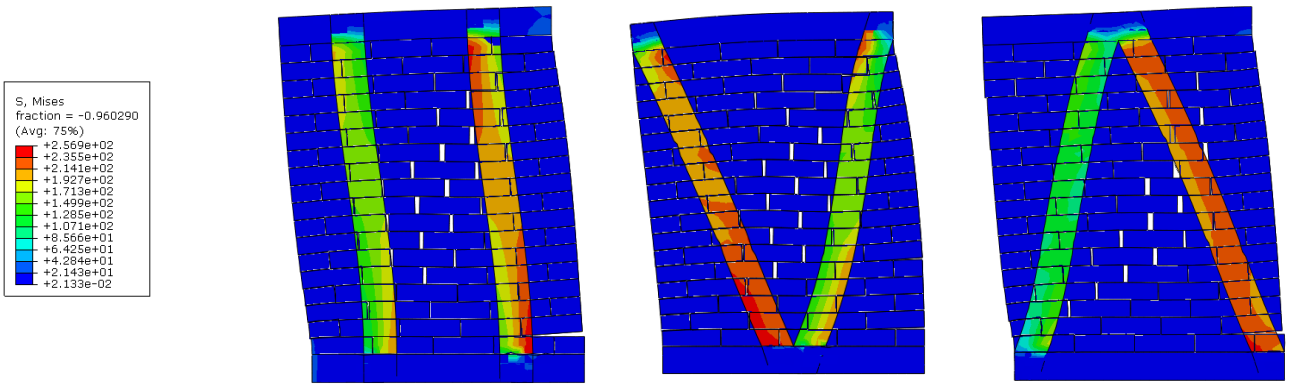

Fig. 16. Failure mode of reinforced masonry walls.

These findings have significant practical implications for structural engineers involved in the seismic retrofitting of unreinforced masonry (URM) buildings. The demonstrated effectiveness of Fe-SMA strips in enhancing lateral strength and ductility offers a viable solution for upgrading existing masonry walls, particularly in earthquake-prone regions. Due to their thermal activation mechanism, Fe-SMAs enable easy application of post-tensioning without requiring mechanical anchorage systems, which simplifies installation and minimizes intervention in heritage or occupied structures. Moreover, the ability to configure reinforcement in vertical and diagonal patterns provides design flexibility based on architectural constraints and desired performance levels. Engineers can integrate this technique into performance-based retrofit strategies, using numerical modeling tools like Abaqus to predict behavior and optimize reinforcement layout and post-tensioning levels before implementation. As such, Fe-SMA-based retrofitting can serve as a practical and cost-effective approach in both emergency strengthening scenarios and long-term rehabilitation programs.

It is important to note that in the current study, the Fe-SMA strips were modeled using fixed mechanical properties corresponding to their post-activation state. However, Fe-SMAs exhibit temperature-dependent behavior, particularly during thermal activation, where phase transformation from martensite to austenite occurs and influences stress development. While this simplification does not significantly affect the global structural response after activation, it may limit the accuracy in capturing transient thermal-mechanical interactions. Future studies are encouraged to adopt coupled thermo-mechanical models or user-defined material subroutines to simulate the evolution of recovery stress during activation and cooling phases for a more comprehensive analysis.

1. Three reinforcement configurations were evaluated: vertically oriented strips, V-shaped, and Λ-shaped arrangements. Post-tensioning stress levels of 100 MPa, 200 MPa, 300 MPa, and 400 MPa were applied to assess their influence on structural performance. The results showed a clear trend: as the level of post-tensioning increased, so did the lateral resistance of the wall. In the vertically reinforced walls, the improvement was primarily due to the frictional forces enhanced by the vertical post-tensioning. Conversely, in the V- and Λ-shaped configurations, in addition to frictional improvement, the SMA strips acted as diagonal braces, directly contributing to the lateral stiffness and resistance.
2. Vertically reinforced walls exhibited up to 96% improvement in lateral resistance compared to the unreinforced wall. V-

shaped and Λ-shaped reinforcements showed increases of approximately 55% and 61%, respectively. Furthermore, the stiffness of the walls improved significantly in all reinforced models, particularly in the inclined configurations due to their bracing effect, which helped in resisting lateral deformation more effectively.

3. Importantly, the mode of failure in all cases remained primarily diagonal shear, which is typical for masonry walls under lateral loading. This indicates that while the post-tensioning improved the performance characteristics, such as strength and stiffness, it did not alter the fundamental failure mechanism. Instead, it delayed the onset of failure and enhanced energy dissipation.

In conclusion, Fe-SMA strips offer a promising, cost-effective, and easily implementable solution for strengthening masonry walls. Their ability to generate post-tensioning forces through thermal activation allows for innovative reinforcement strategies in both vertical and diagonal directions. The findings of this study suggest that Fe-SMAs can be a highly effective tool in seismic retrofitting, enhancing the resilience and safety of masonry structures in earthquake-prone regions. This approach not only improves structural performance but also provides a practical pathway for future research and real-world applications in earthquake engineering.

8. Limitations

While the findings of this study provide valuable insights into the application of Fe-based Shape Memory Alloys (Fe-SMAs) for seismic strengthening of masonry walls, several limitations should be acknowledged. First, the numerical analysis was conducted using the Simplified Micro-modeling approach, which assumes homogenized interaction properties and does not capture detailed micro-cracking or localized stress concentrations at the brick–mortar interface. Second, the study focused solely on monotonic in-plane loading, whereas cyclic or dynamic loading—more representative of real seismic events—was not considered. This may limit the assessment of energy dissipation and degradation behavior. Third, boundary conditions in the model were idealized (e.g., fully fixed base and uniformly distributed vertical load), which may not fully reflect real-world constraints or irregular support conditions in existing buildings. Additionally, the bonding between Fe-SMA strips and masonry was modeled as perfectly rigid, neglecting potential issues such as debonding or interface slip. Future research incorporating more detailed material interfaces, experimental validation under cyclic loads, and practical field-scale testing will be essential to generalize the applicability of the proposed method.

Statements & Declarations

Author contributions

Moein Rezapour: Investigation, Formal analysis, Validation, Resources, Writing - Original Draft, Writing - Review & Editing.

Mehdi Ghassemieh: Conceptualization, Methodology, Project administration, Supervision, Writing - Review & Editing.

Funding

The authors received no financial support for the research, authorship, and/or publication of this article.

Data availability

The data presented in this study will be available on interested request from the corresponding author.

Declarations

The authors declare no conflict of interes.

References

[1] Maheri, M., Najafgholipour, M., Rajabi, A. The influence of mortar head joints on the in-plane and out-of-plane seismic strength of brick masonry walls. Iranian Journal of Science and Technology, 2011; 35: 63-79. doi:10.22099/ijstc.2012.657.

[2] Nateghi, F., Alemi, F. Experimental study of seismic behaviour of typical Iranian URM brick walls. In: 14th World Conference on Earthquake Engineering; 2008 Oct 12-17; Beijing, China. p. 123-130.

[3] Griffith, M. C., Vaculik, J., Lam, N., Wilson, J., Lumantarna, E. Cyclic testing of unreinforced masonry walls in two-way bending. Earthquake Engineering & Structural Dynamics, 2007; 36: 801-821. doi:10.1002/eqe.654.

[4] ElGawady, M., Lestuzzi, P., Badoux, M. Performance of URM walls under in-plane seismic loading. The Masonry Society Journal, 2005; 23: 85-104. doi:10.70803/001c.138950.

[5] Gouveia, J. P., Lourenço, P. B. Masonry shear walls subjected to cyclic loading: influence of confinement and horizontal reinforcement. In: North American Masonry Conference; 2007 June 3-6; St. Louis, Missouri. p. 838–848.

[6] Petry, S., Beyer, K. Cyclic test data of six unreinforced masonry walls with different boundary conditions. Earthquake Spectra, 2015; 31: 2459-2484. doi:10.1193/101513EQS269.

[7] Wang, Q., Shi, Q., Tao, Y. Seismic behavior and shear strength of new-type fired perforated brick walls with high void ratio. Advances in Structural Engineering, 2019; 22: 1035-1048. doi:10.1177/1369433218802690.

[8] ElGawady, M. A., Lestuzzi, P., Badoux, M. Aseismic retrofitting of unreinforced masonry walls using FRP. Composites Part B: Engineering, 2005; 37: 148-162. doi:10.1016/j.compositesb.2005.06.003.

[9] Shabdin, M., Khajeh Ahmad Attari, N., Zargaran, M. Experimental Study on Seismic Behavior of Unreinforced Masonry (URM) Brick Walls Strengthened in the Boundaries with Shotcrete. Journal of Earthquake Engineering, 2019; 1-27. doi:10.1080/13632469.2019.1577763.

[10] Hamakareem, M. I. Prestressed Masonry -Methods of Prestressing, Advantages and Applications. 2025. https://theconstructor.org/concrete/prestressed-masonry-methods-advantages-applications/16173/.

[11] Sadeghi Marzaleh, A. Seismic in-plane behavior of post-tensioned existing clay brick masonry walls, (PhD Thesis). Zurich (CH): University of ETH Zurich; 2015.

[12] Schultz, A. E., Scolforo, M. J. Overview of prestressed masonry. The Masonry Society Journal, 1991; 10: 6-21. doi:10.70803/001c.141160.

[13] Kohail, M., Elshafie, H., Rashad, A., Okail, H. Behavior of post-tensioned dry-stack interlocking masonry shear walls under cyclic in-plane loading. Construction and Building Materials, 2019; 196: 539-554. doi:10.1016/j.conbuildmat.2018.11.149.

[14] Soltanzadeh, G., Osman, H. B., Vafaei, M., Vahed, Y. K. Seismic retrofit of masonry wall infilled RC frames through external post-tensioning. Bulletin of Earthquake Engineering, 2018; 16: 1487-1510. doi:10.1007/s10518-017-0241-4.

[15] Hassanli, R. Simplified approach to predict the flexural strength of unbonded post-tensioned masonry walls. 1st ed. Cham: Springer; 2019. doi:10.1007/978-3-319-93788-5_6.

[16] Hassanli, R. Flexural Strength Prediction of Unbonded Post-tensioned Masonry Walls. 1st ed. Cham: Springer; 2018. doi:10.1007/978-3-319-93788-5_5.

[17] Hassanli, R. Experimental Investigation of Unbonded Post-tensioned Masonry Walls. 1st ed. Cham: Springer; 2019. doi:10.1007/978-3-319-93788-5_7.

[18] Hassanli, R. Strength and Seismic Performance Factors of Post-tensioned Masonry Walls. 1st ed. Cham: Springer; 2018. doi:10.1007/978-3-319-93788-5_3.

[19] Laursen, P. T., Ingham, J. M. Structural testing of single-storey post-tensioned concrete masonry walls. The Masonry Society Journal, 2001; 19: 69-82. doi:10.70803/001c.142720.

[20] Quiroz, A. P. Seismic vulnerability of historic masonry towers by external prestressing devices, (PhD Thesis). University of Naples Federico; 2011.

[21] Babatunde, S. A. Review of strengthening techniques for masonry using fiber reinforced polymers. Composite Structures, 2017; 161: 246-255. doi:10.1016/j.compstruct.2016.10.132.

[22] Seim, W., Pfeiffer, U. Local post-strengthening of masonry structures with fiber-reinforced polymers (FRPs). Construction and Building Materials, 2011; 25: 3393-3403. doi:10.1016/j.conbuildmat.2011.03.030.

[23] Hong, K.-N., Yeon, Y.-M., Shim, W.-B., Kim, D.-H. Recovery Behavior of Fe-Based Shape Memory Alloys under Different Restraints. Applied Sciences, 2020; 10: 3441. doi:10.3390/app10103441.

[24] Choi, E., Ostadrahimi, A., Kim, W. J., Seo, J. Prestressing effect of embedded Fe-based SMA wire on the flexural behavior of mortar beams. Engineering Structures, 2021; 227: 111472. doi:10.1016/j.engstruct.2020.111472.

[25] Shahverdi, M., Michels, J., Czaderski, C., Motavalli, M. Iron-based shape memory alloy strips for strengthening RC members: Material behavior and characterization. Construction and Building Materials, 2018; 173: 586-599. doi:10.1016/j.conbuildmat.2018.04.057.

[26] Shahverdi, M., Czaderski, C., Motavalli, M. Iron-based shape memory alloys for prestressed near-surface mounted strengthening of reinforced concrete beams. Construction and Building Materials, 2016; 112: 28-38. doi:10.1016/j.conbuildmat.2016.02.174.

[27] Shahverdi, M., Czaderski, C., Annen, P., Motavalli, M. Strengthening of RC beams by iron-based shape memory alloy bars embedded in a shotcrete layer. Engineering Structures, 2016; 117: 263-273. doi:10.1016/j.engstruct.2016.03.023.

[28] Izadi, M., Motavalli, M., Ghafoori, E. Iron-based shape memory alloy (Fe-SMA) for fatigue strengthening of cracked steel bridge connections. Construction and Building Materials, 2019; 227: 116800. doi:10.1016/j.conbuildmat.2019.116800.

[29] Izadi, M., Ghafoori, E., Shahverdi, M., Motavalli, M., Maalek, S. Development of an iron-based shape memory alloy (Fe-SMA) strengthening system for steel plates. Engineering Structures, 2018; 174: 433-446. doi:10.1016/j.engstruct.2018.07.073.

[30] Izadi, M., Ghafoori, E., Motavalli, M., Maalek, S. Iron-based shape memory alloy for the fatigue strengthening of cracked steel plates: Effects of re-activations and loading frequencies. Engineering Structures, 2018; 176: 953-967. doi:10.1016/j.engstruct.2018.09.021.

[31] Izadi, M., Ghafoori, E., Hosseini, A., Motavalli, M., Maalek, S., Shahverdi, M. Feasibility of iron-based shape memory alloy strips for prestressed strengthening of steel plates. In: The fourth International Conference on Smart Monitoring, Assessment and Rehabilitation of Civil Structures (SMAR 2017); 2017 Sep 13-15; Zurich, Switzerland. p. 260-268.

[32] Rezapour, M., Ghassemieh, M., Motavalli, M., Shahverdi, M. Numerical Modeling of Unreinforced Masonry Walls Strengthened with Fe-Based Shape Memory Alloy Strips. Materials, 2021; 14: 2961. doi:10.3390/ma14112961.

[33] Lagoudas, D. C. Shape memory alloys: modeling and engineering applications. 1st ed. New York (NY): Springer; 2008. doi:10.1007/978-0-387-47685-8.

[34] Vermeltfoort, A. T., Raijmakers, T., Janssen, H. Shear tests on masonry walls. In: 6th North American Masonry Conference; 1993 Jun 6-9; Philadelphia, Pennsylvania. p. 1183-1193.

[35] Lourenço, P. J. B. B. Computational strategies for masonry structures, (PhD Thesis). Delft (NL): Delft university Press; 1996.

[36] Rezapour, M., Ghassemieh, M. Macroscopic modelling of coupled concrete shear wall. Engineering Structures, 2018; 169: 37-54. doi:10.1016/j.engstruct.2018.04.088.

[37] Lee, J., Fenves, G. L. Plastic-damage model for cyclic loading of concrete structures. Journal of Engineering Mechanics, 1998; 124: 892-900. doi:10.1061/(ASCE)0733-9399(1998)124:8(892).

[38] Lubliner, J., Oliver, J., Oller, S., Oñate, E. A plastic-damage model for concrete. International Journal of Solids and Structures, 1989; doi:10.1016/0020-7683(89)90050-4.

[39] Mander, J. B., Priestley, M. J., Park, R. Theoretical stress-strain model for confined concrete. Journal of Structural Engineering, 1988; 114: 1804-1826. doi:10.1061/(ASCE)0733-9445(1988)114:8(1804).

[40] Selby, R. G., Vecchio, F. J. A constitutive model for analysis of reinforced concrete solids. Canadian Journal of Civil Engineering, 1997; 24: 460-470. doi:10.1139/l96-135.

Civil Engineering and Applied Solutions

Research Article

journal homepage: ceas.journals.umz.ac.ir

CEAS Civil Engineering and Applied Solutions

Comparative Evaluation of Seismic Behavior of T-Shaped versus Rectangular Concrete Shear Walls in High-Rise Buildings

Mehran Rahimi [a], Khosrow Bargi [a*]

[a] *College of Engineering, School of Civil Engineering, University of Tehran, Tehran, Iran*

ARTICLE INFO

Keywords:
High-rise building
T-shaped shear wall
Seismic behavior
Dual system

Article history:
Received 21 July 2025
Accepted 30 July 2025
Available online 01 September 2025

ABSTRACT

High-rise buildings exhibit complex seismic behavior due to their height and flexibility, requiring robust lateral load-resisting systems to ensure safety and serviceability. Among these, dual systems combining steel moment frames with reinforced concrete shear walls are widely adopted in tall building design. This study evaluates the seismic performance of a 30-story high-rise building located in a high seismic zone with a design base acceleration of A = 0.5, representing a conservative scenario for critical structures. Two shear wall configurations—rectangular and T-shaped were modeled and analyzed through both linear response spectrum and nonlinear time history analyses using six representative earthquake records. The results demonstrate that T-shaped shear walls provide superior lateral stiffness, reduced roof displacements, and lower inter-story drifts compared to rectangular walls under both elastic and inelastic conditions. This improved behavior is attributed to the higher moment of inertia of T-shaped walls, making them a more efficient and resilient choice for high-rise buildings in seismic-prone regions.

1. Introduction

As urban development trends increasingly favor vertical expansion, high-rise buildings have become a defining element of modern cityscapes. Due to their height and flexibility, these structures are especially vulnerable to lateral forces such as wind and seismic loads, which can significantly affect their dynamic response and overall stability [1, 2]. Therefore, the selection of an effective lateral load-resisting system is essential to ensure both structural safety and serviceability [3]. Among the available options, dual systems-combining moment-resisting frames with shear walls-offer a well-balanced solution by providing both ductility and stiffness [4, 5]. In particular, composite steel moment frames integrated with reinforced concrete shear walls are widely adopted in tall building design for their superior seismic resilience and structural efficiency. Given their increasing use, numerous studies have been conducted to evaluate the seismic performance of various shear wall configurations, particularly T-shaped walls, which are commonly used in high-rise construction [6, 7].

As part of efforts to evaluate the seismic performance of T-shaped shear walls, Thomsen IV and Wallace [8] conducted experimental and analytical studies, demonstrating that positive bending, which places the flange in compression, results in better ductility compared to negative bending, where the flange is in tension and ductility is reduced. Brueggen [9] tested two steel–concrete composite T-shaped shear wall models and found lower displacement capacity compared to rectangular or symmetrically flanged walls, emphasizing the need for careful design at the free web edge. Similarly, Pin-Le and Qing-ning [10] tested six scaled T-shaped walls under cyclic loading and found the web to be the weakest zone, failing due to concrete crushing and reinforcement yielding. Lu and Yang [6] also observed flexural failure at the free web boundary in slender steel-reinforced concrete T-shaped walls, highlighting the importance of proper confinement as axial load increases. Ji et al. [11] compared Chinese and American seismic codes and found GB 50011-2010 underestimates boundary element length at the non-flange end, risking premature failure; their proposed displacement-based method improved drift capacity without added reinforcement. Lan et al. [12] found that T-shaped

* Corresponding author.
E-mail addresses: kbargi@ut.ac.ir (K. Bargi).

https://doi.org/10.22080/ceas.2025.29715.1029
ISSN: 3092-7749/
How to cite this article: Rahimi, M., Bargi, K. Comparative Evaluation of Seismic Behavior of T-Shaped versus Rectangular Concrete Shear Walls in High-Rise Buildings. Civil Engineering and Applied Solutions. 2025; 1(4): 16–26. doi:10.22080/ceas.2025.29715.1029.

composite walls performed best under 45° loading, with higher axial loads increasing strength but reducing ductility, and embedded steel enhancing performance, especially in flexure-dominant directions.

Following these findings, several recent studies have explored advanced configurations and loading conditions. Brueggen et al. [13] found that distributing longitudinal reinforcement across the flange, rather than concentrating it in boundary elements, reduced shear lag, crack widths, and damage in T-shaped RC walls under multidirectional cyclic loading. Wang et al. [14] further revealed that biaxial loading, especially with larger paths like the square, intensified damage and reduced strength and deformation capacity due to stress coupling and force redistribution at wall corners. In the context of precast systems, Shen et al. [15] developed a T-shaped wall with H-shaped shear keys and a design method to control yield force and displacement by adjusting key geometry, while Gu et al. [16] showed that T-shaped precast walls with U-shaped steel bar connections and higher axial loads matched or outperformed cast-in-place walls. Ji et al. [17] found that walls under high axial load (~0.19) achieved >2.0% drift with ACI 318-19 or displacement-based design, while GB 50011-2010 designs failed early; they also identified SFI-MVLEM-3D as the most accurate FE model for capturing shear-flexure interaction. Yang et al. [18] showed that rebar corrosion significantly reduces performance, especially under positive loading, and developed a validated FE model for evaluating aging walls in corrosive environments. Finally, Mo et al. [19] introduced a T-shaped steel–concrete composite wall with C-shaped steel frames, demonstrating excellent seismic performance, with lower shear span ratios, an optimal axial load ratio of 0.4, and greater steel thickness, all improving wall behavior.

This study investigates the seismic performance of a 30-story high-rise building located in a high seismic zone with a design base acceleration of $A = 0.5$, a conservative value exceeding the typical upper limit of $A = 0.35$ to account for proximity to active faults. The research focuses on a comparative analysis of two commonly used shear wall configurations, rectangular and T-shaped, to identify the optimal solution for enhancing seismic resilience and cost-effectiveness in tall buildings. The evaluation begins with linear response spectrum analysis to determine the most efficient wall arrangement based on roof displacements, followed by an assessment of story displacements and inter-story drifts. To capture inelastic behavior, nonlinear time history analyses were conducted using six representative earthquake records applied simultaneously in both orthogonal directions. The combined results of linear and nonlinear analyses reveal the relative seismic performance of each configuration, offering practical insights into the optimal shear wall design for high-rise structures in earthquake-prone regions.

2. Methodology

This section presents a summary of the modeling assumptions, building codes, analysis parameters, seismic load considerations, and software tools used for design and analysis. The structural design of the 30-story building was carried out using ETABS v15.2.2. For linear response spectrum analysis, ETABS v15.2.2 was employed, while SAP2000 v18 was used for nonlinear time history analysis.

2.1. Geometric specifications of the 30-story building

Fig. 1 shows the structural plan of the building, which consists of regular bays arranged in a grid of 5 bays in both the longitudinal and transverse directions, with each bay measuring 6 meters. The studied structure has 30 stories, with each story having a uniform height of 3.5 meters. The structural modeling has been conducted in three dimensions.

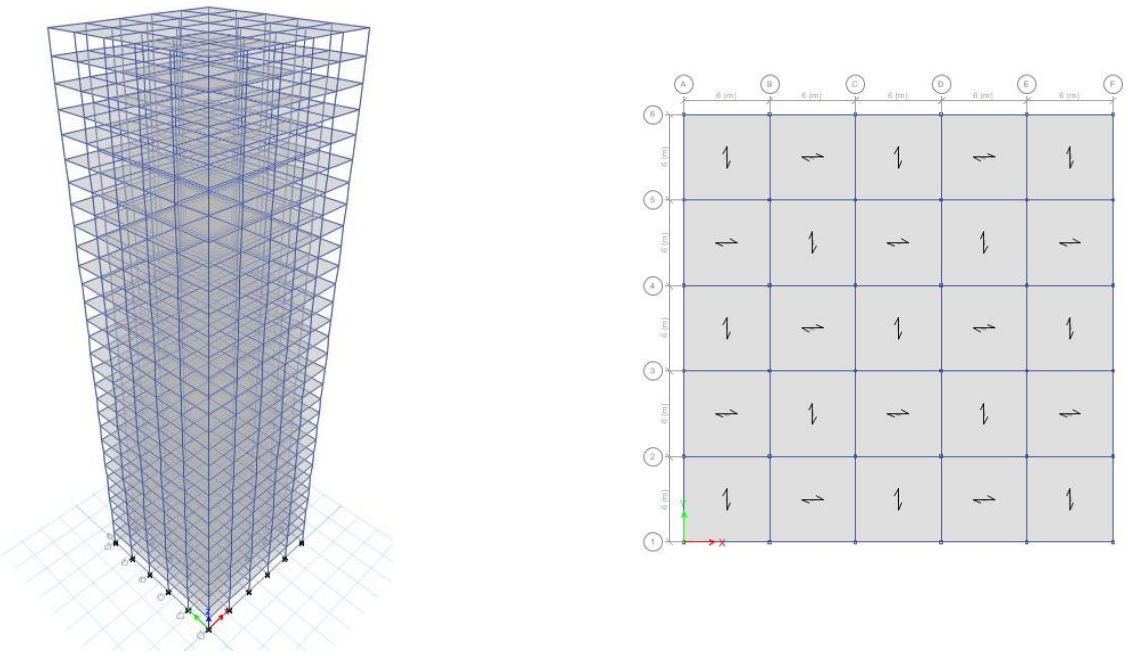

Fig. 1. 3D view and plan layout of the structural frame.

The lateral load-resisting system consists of a dual system: a special reinforced concrete shear wall system combined with a

special moment-resisting steel frame system. For the 30-story building, the thickness of the shear walls is:

- 50 cm for floors 1–10
- 40 cm for floors 11–20
- 30 cm for floors 21–30

2.2. Loading

In the structural model, various types of gravity and wall loads were applied based on standard design considerations for residential buildings. These include dead loads such as the self-weight of structural components and floor finishes, as well as live loads representing occupancy. Wall loads were also assigned to account for the weight of perimeter walls on both typical floors and the roof. A summary of the applied loads is presented in Table 1.

Table 1. Applied dead, live, and wall loads.

Load Type	Magnitude	Unit
Dead load for floors	500	kg/m²
Partition load	100	kg/m²
Live load for floors	200	kg/m²
Wall load (dead)	600	kg/m²
Roof dead load	500	kg/m²
Roof live load	150	kg/m²
Roof wall load	300	kg/m²

2.3. Design codes and structural specifications

The structure is intended for residential use, and the potential for cracking in the shear walls has been explicitly considered in the design. The moment-resisting frame is designed to resist at least 25% of the earthquake-induced lateral forces, incorporating the consideration of P-Delta effects in the design process. Seismic analysis has been performed using the standard response spectrum defined in the Iranian Code 2800 [20], ensuring that the base shear demand exceeds the minimum allowable threshold. The building is assumed to be located in a seismic zone characterized by a design acceleration coefficient of $A = 0.5$. Additionally, the site soil conditions are classified as Type II. To extend the evaluation beyond the elastic range, nonlinear time history analysis was also performed to capture the inelastic seismic response of the structure under real ground motions applied in both principal directions.

The structural design, analysis, and validation are carried out per the following recognized standards:

1. Iranian Seismic Code – Standard 2800, 4th Edition [20];
2. Iranian National Building Code, Part 6 – Loadings (Edition 1392) [21];
3. ACI 318-14 for concrete shear wall design [22];
4. AISC 360-10 for steel frame design [23];
5. Time history nonlinear dynamic analysis;
6. Wall cracking effects and ductility capacity in time history analysis;
7. Time history records selected based on compatibility with site soil conditions and seismic design parameters.

The steel used for both beams and columns is of type ST37, with a yield strength of 2400 kg/cm² and an ultimate tensile strength of 3700 kg/cm². The concrete compressive strength used in the design of the shear walls is 25 MPa, and the reinforcing bars are of type AIII. The beams and columns have cross-sectional shapes of I and box, respectively.

2.4. Arrangement of shear walls

Figs. 2 and 3 illustrate various configurations of rectangular and T-shaped shear walls implemented in the building plan. To maintain uniformity and enable an objective comparison across these configurations, the total surface area of the shear walls was kept constant in all models. The rectangular and T-shaped shear walls were distributed across all floors of the structure and analyzed under identical structural and seismic conditions. Based on the analytical results, the most efficient arrangement for each wall type was identified and compared to determine the optimal shear wall layout.

3. Numerical results

This section presents the results of both linear and nonlinear time history analyses performed on a 30-story building located in a high seismic zone with a design base acceleration of $A = 0.5$. The study focuses on assessing both elastic and inelastic structural behavior under seismic loading conditions.

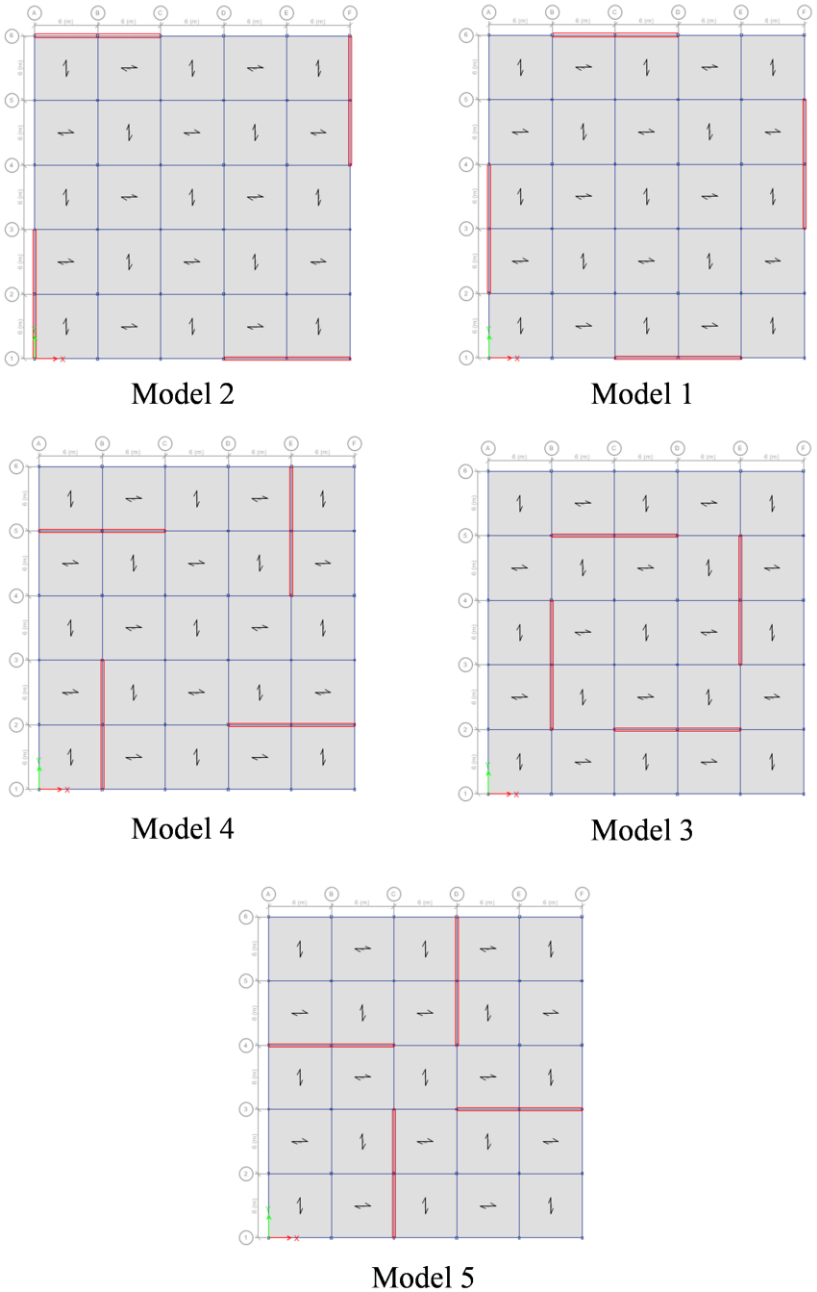

Fig. 2. Arrangements of rectangular shear walls in the building plan.

3.1. Linear behavior using response spectrum analysis

In this study, rectangular and T-shaped shear walls were first modeled in the plan of a 30-story high-rise building located in a region with seismic acceleration coefficient $A = 0.5$. The modeling was performed in three dimensions to closely approximate real behavior. Based on the roof displacement results, the optimal wall arrangement is determined. Figs. 4 and 5 illustrate the roof displacement result for various configurations of rectangular and T-shaped shear walls.

It is observed that Model 3 yields the best configuration for the rectangular shear wall, while Model 4 is the most effective for the T-shaped shear wall. The optimal placement of shear walls-both rectangular and T-shaped-occurs when the walls are located within interior frames. Placing shear walls in the outermost frames leads to stiffness concentration at the corners of the building, resulting in a flexible interior zone. Conversely, when the shear walls are positioned too close to the center of mass, the interior becomes excessively stiff while the exterior remains flexible. Therefore, the best structural performance is achieved when the shear wall is located at a distance between the innermost and outermost frames. Subsequently, the optimal configurations for rectangular and T-shaped shear walls are compared in terms of story displacement and inter-story drift. These optimal configurations, identified based on the roof displacement results shown in Figs. 4 and 5, are further analyzed in terms of story displacement and inter-story drift. Figs. 6a, 6b, 7a, and 7b present the corresponding results in both the X and Y directions, with all displacement values reported in centimeters.

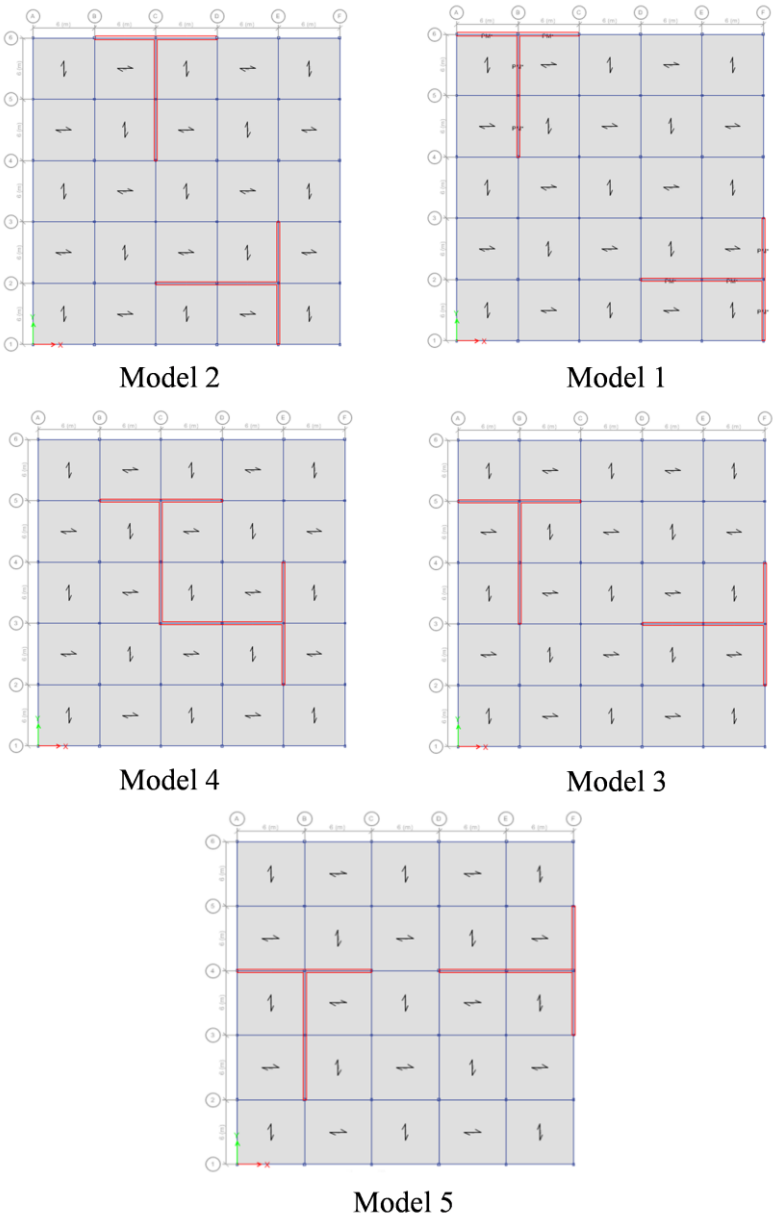

Fig. 3. Arrangements of T-shaped shear walls in the building plan.

Figs. 6 and 7 illustrate the comparison between the optimal rectangular and T-shaped shear wall configurations in terms of story displacement and inter-story drift. In these figures, the vertical axis represents the story levels, while the horizontal axis shows the displacement (in centimeters) and drift ratio, respectively. The red curve corresponds to the rectangular shear wall configuration, while the blue curve represents the T-shaped configuration. As shown in Fig. 6, the T-shaped walls result in lower lateral displacements in both the X and Y directions, particularly at the upper stories, indicating improved lateral stiffness and better control of overall building sway. Similarly, Fig. 7 shows that the T-shaped configuration produces lower inter-story drift ratios throughout the building height, which implies a more favorable deformation pattern under seismic loading. This improved behavior is attributed to the higher moment of inertia of T-shaped shear walls compared to rectangular ones, which leads to increased stiffness and consequently reduced displacements. These results demonstrate that the T-shaped shear wall configuration provides better seismic performance compared to the rectangular arrangement under the same conditions.

3.2. Nonlinear behavior analysis using earthquake time history records

To extend the evaluation beyond the linear response, nonlinear dynamic time history analysis was performed to investigate the seismic behavior of the structure under more realistic loading conditions. This analysis was carried out on the optimal configurations of rectangular and T-shaped shear walls identified in the previous section. Six representative earthquake ground motion records were used in this study, including Tabas, Bam, Kobe, Northridge, Imperial Valley, and Loma Prieta.

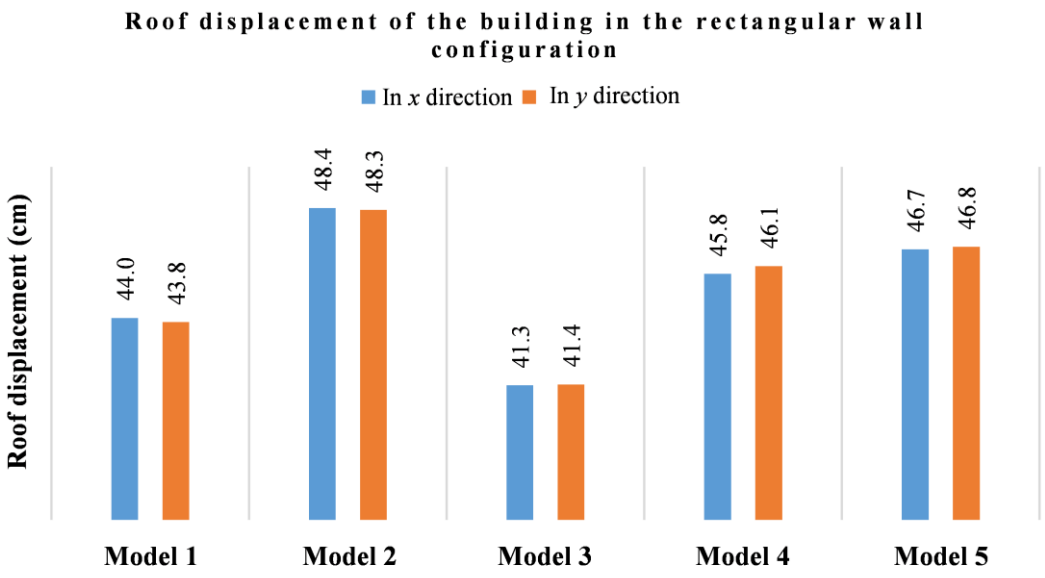

Fig. 4. Roof displacement for different configurations of rectangular shear walls.

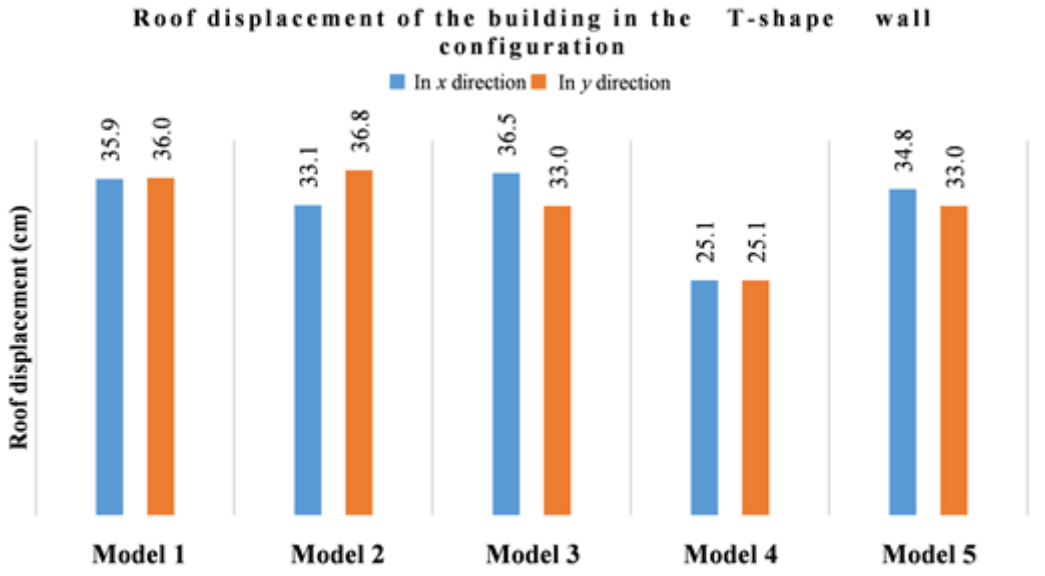

Fig. 5. Roof displacement for different configurations of T-shaped shear walls.

These records were applied simultaneously in both X and Y directions to capture the true multi-directional effects of seismic loading and assess the nonlinear response of each wall configuration. All ground motions were obtained from the Pacific Earthquake Engineering Research Center (PEER) Ground Motion Database, hosted by the University of California, Berkeley [24]. The detailed characteristics of these records are provided in Table 2.

In the nonlinear dynamic analysis, the shear walls were modeled using nonlinear shell elements to accurately capture their inelastic behavior. Beams and columns were assigned plastic hinges of the "auto" type per the guidelines provided by FEMA 356. The analysis was conducted in three dimensions, with the selected earthquake ground motion records applied simultaneously in both the X and Y directions to account for multi-directional seismic effects. To ensure consistency, the average response spectrum of the six records was used, and a uniform scale factor was applied to all ground motions. The results of the nonlinear time history analysis, including the structural response to each of the six individual records and their averaged response, are illustrated in Figs. 8 and 9 for both X and Y directions.

As illustrated in Figs. 8 and 9, the rectangular shear wall configuration (shown in blue) consistently exhibits higher roof displacements compared to the T-shaped configuration (shown in orange) in both the X and Y directions. This trend is evident across all individual records and their average, indicating that the T-shaped walls offer greater lateral stiffness and more effective

control of seismic deformation.

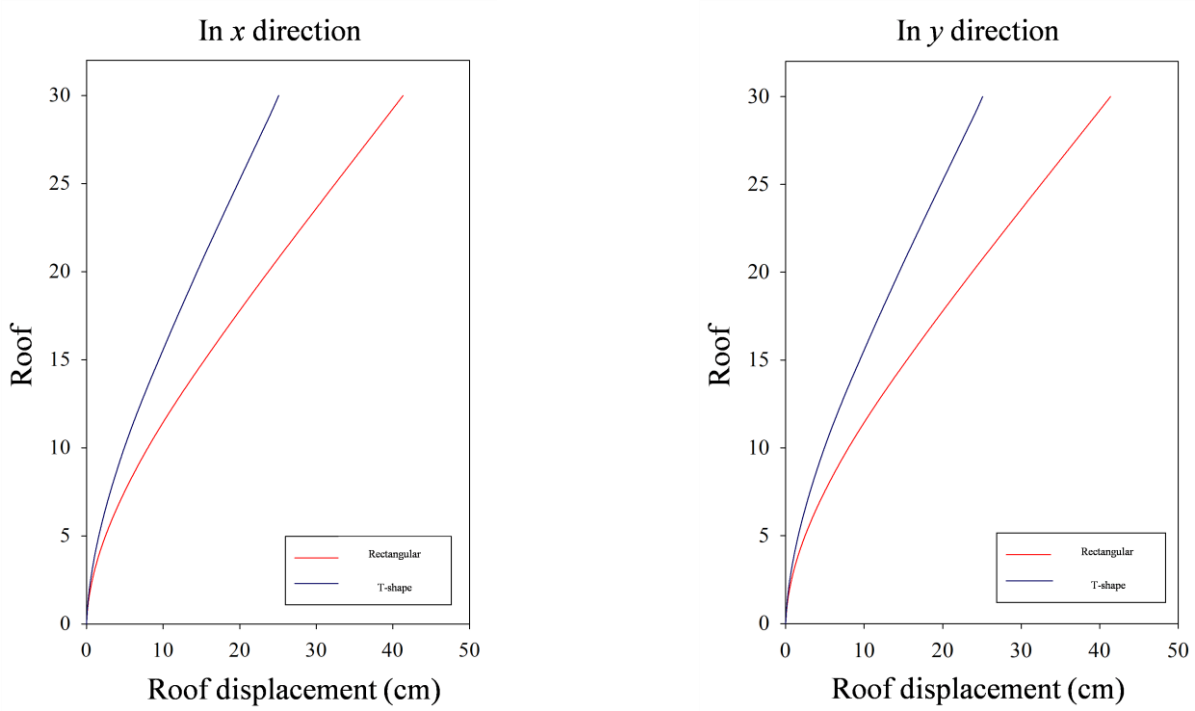

(a) X direction **(b) Y direction**

Fig. 6. Story displacement for the optimal rectangular and T-shaped wall configurations.

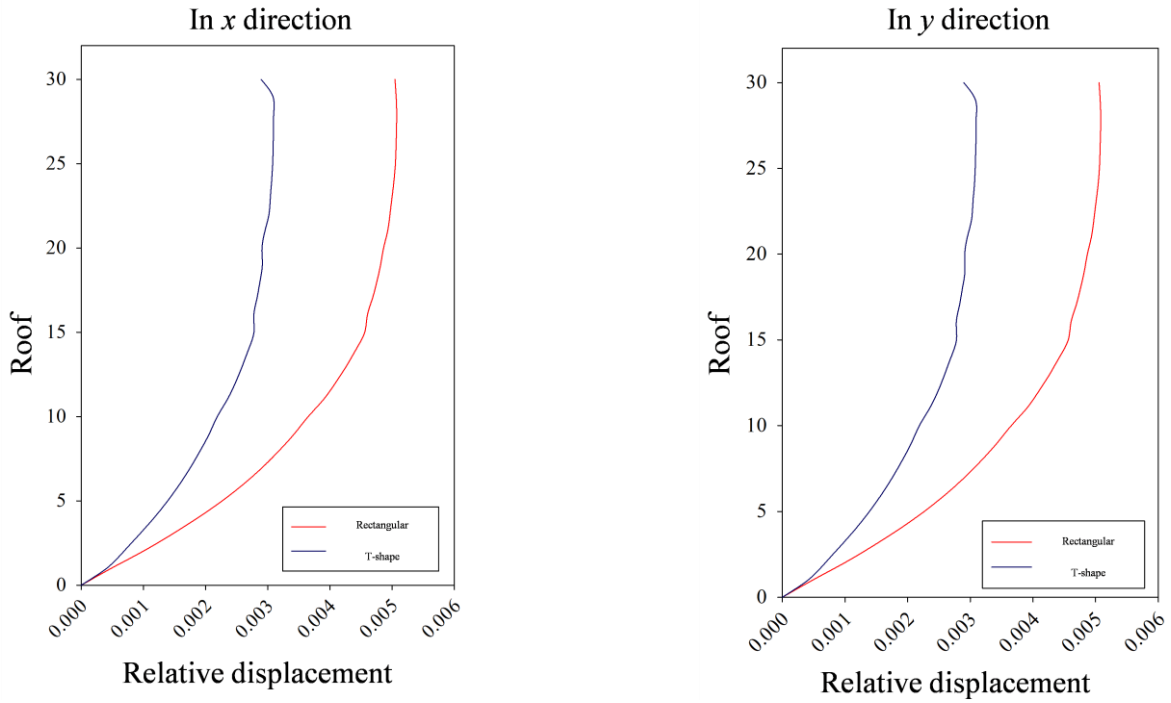

(a) X direction **(b) Y direction**

Fig. 7. Inter-story drift for the optimal rectangular and T-shaped wall configurations.

The superior performance of the T-shaped configuration is attributed to its higher moment of inertia, which results in reduced displacements under lateral loads. These findings are consistent with the results of the linear analysis and confirm the T-shaped shear wall's enhanced seismic performance under both linear and nonlinear dynamic conditions. In addition to the roof displacement results under individual and average ground motions, a more detailed assessment of lateral deformation along the height of the structure is presented in Fig. 10.

As observed in Fig. 10, the T-shaped shear wall configuration (blue curve) consistently exhibits lower story displacements compared to the rectangular configuration (red curve) throughout the height of the building. This indicates that the T-shaped walls provide better lateral stiffness and improved seismic control under average earthquake loading conditions.

Table 2. Ground motion records used in nonlinear time history analysis.

Earthquake Name	*R* (km)	PGA_T	PGA_L	*M*	Station Name	Year	RSN
Northridge	5.43	1.00g	0.54g	6.69	Jensen Filter	1994	983
Bam	1.70	0.58g	0.77g	6.60	Bam	2003	4040
Tabas	2.05	0.80g	0.77g	7.35	Tabas	1978	143
Imperial Valley	2.66	0.79g	0.57g	6.53	Bonds Corner	1979	160
Loma Prieta	17.47	0.66g	0.39g	6.93	Waho	1989	811
Kobe	1.46	0.67g	0.61g	6.90	Takatori	1995	1120

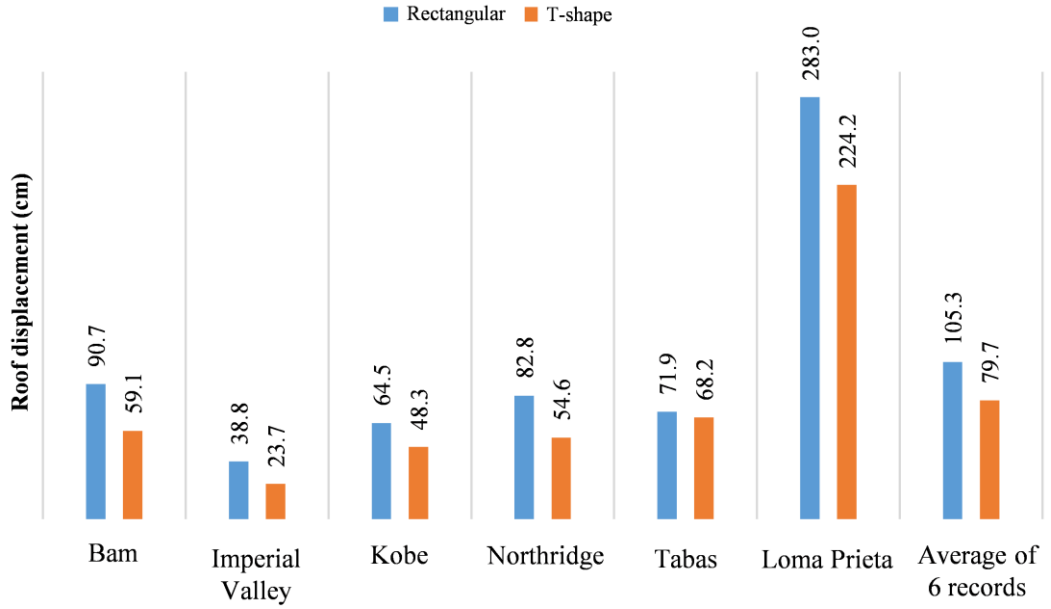

Fig. 8. Roof displacement in the X direction for the optimal rectangular and T-shaped shear wall configurations under each earthquake record.

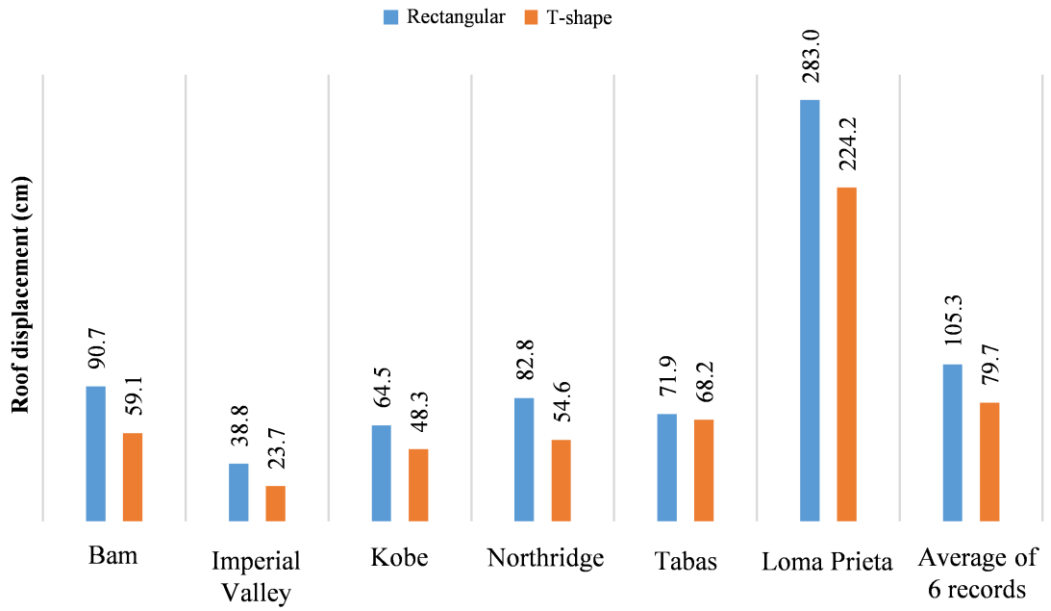

Fig. 9. Roof displacement in the Y direction for the optimal rectangular and T-shaped shear wall configurations under each earthquake record.

These findings reinforce the earlier results obtained from individual ground motions and confirm the superior performance of the T-shaped configuration in limiting lateral deformations under dynamic excitation. Finally, the average inter-story drift for the six earthquake records is shown in Fig. 11.

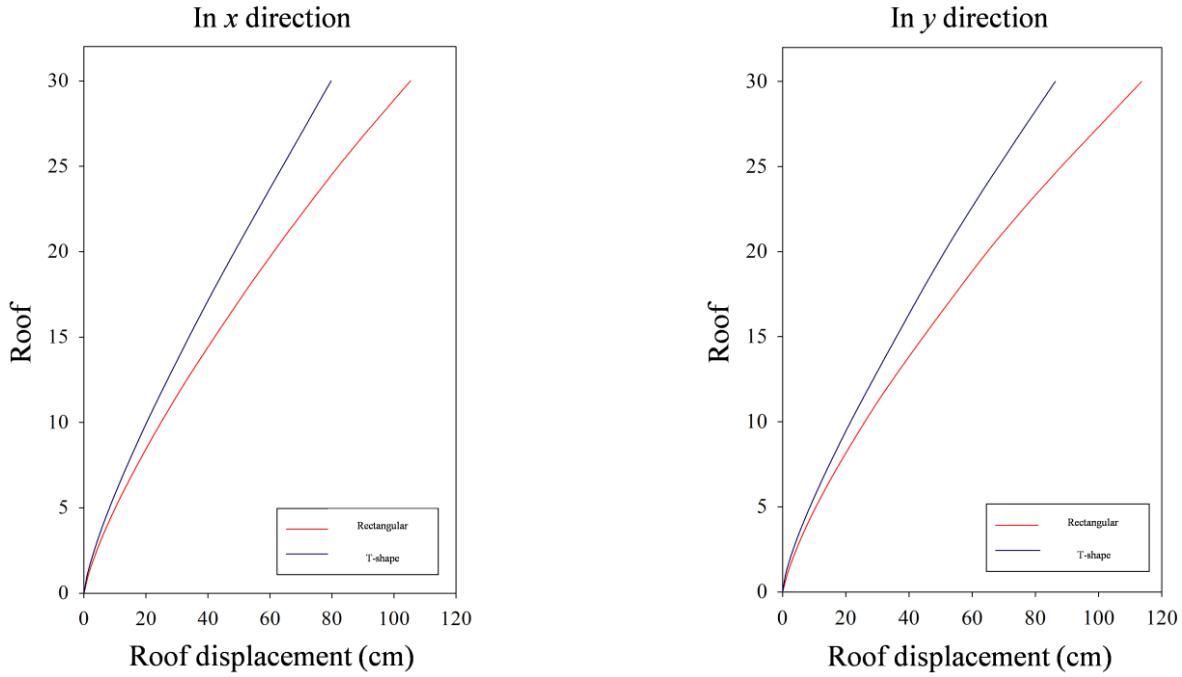

(a) X direction **(b) Y direction**

Fig. 10. Story displacement in the nonlinear analysis for the optimal rectangular and T-shaped shear wall configurations.

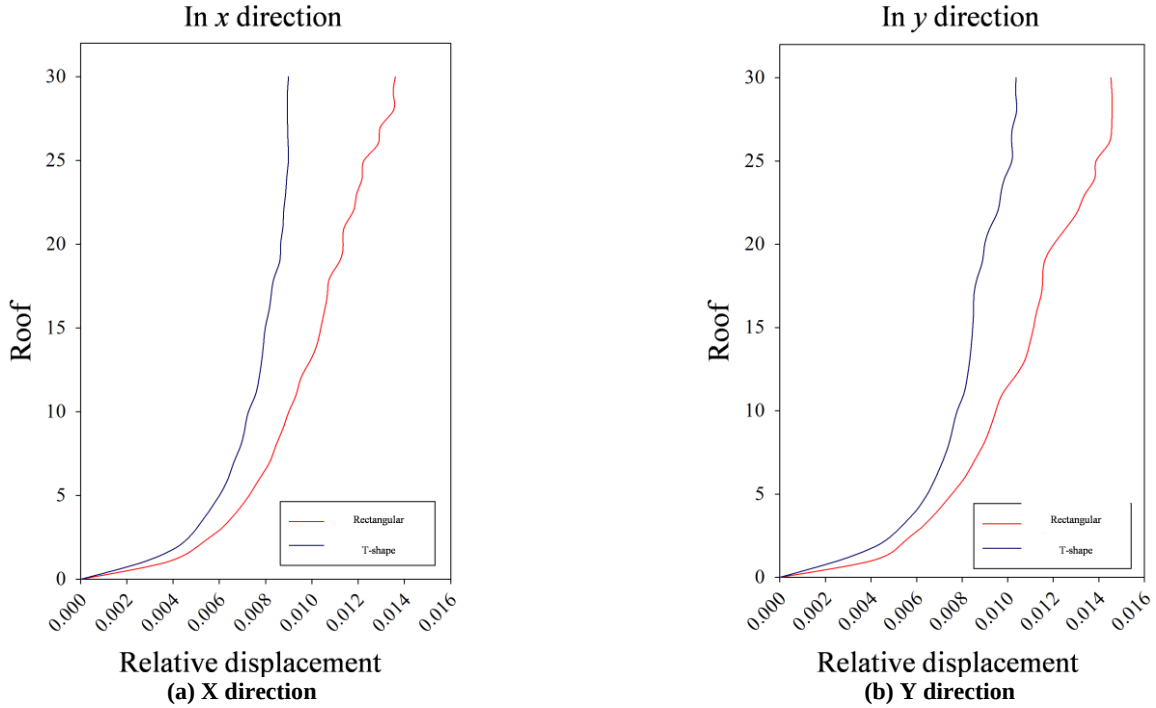

(a) X direction **(b) Y direction**

Fig. 11. Inter-story drift distribution for the optimal rectangular and T-shaped shear wall configurations obtained from nonlinear time history analysis.

Fig. 11 illustrates the average inter-story drift distribution obtained from the nonlinear time history analysis for the optimal rectangular and T-shaped shear wall configurations in both the X and Y directions. The vertical axis represents the story levels, while the horizontal axis indicates the relative inter-story drift ratio. As shown in both graphs, the T-shaped configuration (blue curve) results in lower inter-story drift values throughout the height of the building compared to the rectangular configuration (red curve). This indicates that the T-shaped walls provide better control over story deformation, leading to improved seismic performance and reduced damage potential in structural and non-structural components. These results are consistent with previous displacement analyses and further confirm the superior behavior of the T-shaped shear wall configuration under nonlinear dynamic loading.

4. Conclusions

As observed, the optimal placement of both rectangular and T-shaped shear walls occurs when the walls are located within the intermediate (central) frames of the structure. This configuration resulted in the minimum displacement in both the X and Y

directions. When shear walls are placed in the outermost frames, stiffness tends to concentrate at the building corners, leading to a more flexible interior. Conversely, placing shear walls too close to the center of mass increases the stiffness of the interior zones while leaving the exterior zones relatively flexible. Therefore, the most balanced and efficient structural behavior is achieved when the shear walls are positioned at a distance between the innermost and outermost frames. The structure with T-shaped shear walls exhibits superior performance compared to the one with rectangular shear walls, both in terms of roof displacement and inter-story drift. This improvement is attributed to the fact that the stiffness of a shear wall is directly related to its moment of inertia in plan, and the T-shaped wall possesses a higher moment of inertia than the rectangular wall in this case. In the following section, the optimal configurations of rectangular and T-shaped shear walls, identified earlier, were subjected to nonlinear time history analysis for comparison of their inelastic behavior. As observed, in both the X and Y directions, and across all six individual ground motion records as well as their average response, the structure with T-shaped shear walls consistently demonstrates superior performance under nonlinear conditions. In conclusion, for a seismic zone with a design base acceleration of $A = 0.5$, the structure with T-shaped shear walls demonstrated superior performance compared to the one with rectangular shear walls, both in terms of linear and nonlinear.

Statements & Declarations

Author contributions

Mehran Rahimi: Conceptualization, Investigation, Formal analysis, Resources, Writing - Original Draft, Writing - Review & Editing.

Khosrow Bargi: Conceptualization, Formal analysis, Resources, Supervision, Project administration, Writing - Review & Editing.

Funding

The authors received no financial support for the research, authorship, and/or publication of this article.

Data availability

The data presented in this study will be available on interested request from the corresponding author.

Declarations

The authors declare no conflict of interes.

References

[1] Cheng, Q., Ren, H., Meng, X., Li, A., Xie, L. Real-time seismic response prediction method of high-rise buildings based on deep learning for earthquake early warning. International Journal of Disaster Risk Reduction, 2025; 119: 105294. doi:10.1016/j.ijdrr.2025.105294.

[2] Wang, Y., Deng, T., Fu, J. Investigation of wind load characteristics and structural responses in asymmetric linked twin-tower high-rise buildings. Engineering Structures, 2025; 341: 120796. doi:10.1016/j.engstruct.2025.120796.

[3] Abduljaleel, Y. W., Usman, F., Syamsir, A., Albaker, B. M., Najeeb, M. I., Khattab, M. M., Al-Humairi, S. N. S. A Systematic Review on Utilizing Artificial Intelligence in Lateral Resisting Systems of Buildings. Archives of Computational Methods in Engineering, 2025; doi:10.1007/s11831-025-10288-7.

[4] Farzi, M., Tehranizadeh, M., Khademi, M. Seismic collapse risk and performance factors assessment of RC dual lateral load-resisting system under far- and near-fault earthquake conditions. Structures, 2025; 73: 108333. doi:10.1016/j.istruc.2025.108333.

[5] Valenzuela-Beltran, F., Llanes-Tizoc, M. D., Reyes-Salazar, A. Structural Seismic Design and Evaluation. 2025; 15: 3059. doi:10.3390/app15063059.

[6] Lu, X., Yang, J. Seismic behavior of T-shaped steel reinforced concrete shear walls in tall buildings under cyclic loading. The Structural Design of Tall and Special Buildings, 2015; 24: 141-157. doi:10.1002/tal.1158.

[7] Isoda, H., Namba, T., Kitamori, A., Mori, T., Miyake, T., Nakagawa, T., Tesfamariam, S. Experimental behavior of L-shaped and T-shaped cross-laminated timber to evaluate shear walls with openings. Journal of Structural Engineering, 2023; 149: 04023036. doi:10.1061/JSENDH.STENG-11474.

[8] Thomsen IV, J. H., Wallace, J. W. Displacement-based design of slender reinforced concrete structural walls—experimental verification. Journal of Structural Engineering, 2004; 130: 618-630. doi:10.1061/(ASCE)0733-9445(2004)130:4(618).

[9] Brueggen, B. L. Performance of T-shaped reinforced concrete structural walls under multi-directional loading, (PhD Thesis). Minneapolis (MN): University of Minnesota; 2009.

[10] Pin-Le, Z., Qing-ning, L. Cyclic loading test of T-shaped mid-rise shear wall. The Structural Design of Tall and Special Buildings, 2013; 22: 759-769. doi:10.1002/tal.723.

[11] Ji, X., Liu, D., Qian, J. Improved design of special boundary elements for T-shaped reinforced concrete walls. Earthquake Engineering and Engineering Vibration, 2017; 16: 83-95. doi:10.1007/s11803-017-0370-4.

[12] Lan, W., Zhang, Z., Li, B. Seismic performance of T-shaped steel-concrete composite structural walls subjected to loadings from different directions. Journal of Constructional Steel Research, 2017; 128: 7-18. doi:10.1016/j.jcsr.2016.08.007.

[13] Brueggen, B. L., French, C. E., Sritharan, S. T-shaped RC structural walls subjected to multidirectional loading: test results and design recommendations. Journal of Structural Engineering, 2017; 143: 04017040. doi:10.1061/(ASCE)ST.1943-541X.0001719.

[14] Wang, B., Wu, M.-Z., Shi, Q.-X., Cai, W.-Z. Effects of biaxial loading path on seismic behavior of T-shaped RC walls. Engineering Structures, 2022; 273: 115080. doi:10.1016/j.engstruct.2022.115080.

[15] Shen, S.-D., Pan, P., He, Z.-Z., Xiao, G.-Q., Ren, J.-Y. Experimental study and finite element analysis of T-shaped precast shear walls with H-shaped shear keys. Earthquake Engineering & Structural Dynamics, 2022; 51: 1158-1179. doi:10.1002/eqe.3609.

[16] Gu, Q., Zhao, D., Li, J., Peng, B., Deng, Q., Tian, S. Seismic performance of T-shaped precast concrete superposed shear walls with cast-in-place boundary columns and special boundary elements. Journal of Building Engineering, 2022; 45: 103503. doi:10.1016/j.jobe.2021.103503.

[17] Ji, X., Sun, L., Wang, S., Kolozvari, K. Seismic behavior and modeling of T-shaped reinforced concrete walls under high axial force ratios. Earthquake Engineering & Structural Dynamics, 2024; 53: 1085-1106. doi:10.1002/eqe.4060.

[18] Yang, L., Zheng, S.-S., Zheng, Y., Dong, L.-G., Wu, H.-L. Experimental investigation and numerical modelling of the seismic performance of corroded T-shaped reinforced concrete shear walls. Engineering Structures, 2023; 283: 115930. doi:10.1016/j.engstruct.2023.115930.

[19] Mo, X., Yuan, Z., Jia, Y., Lu, L., Wei, X., Ke, N. An Experimental and Numerical Parametric Study on a Novel T-Shaped Steel–Concrete Composite Shear Wall. Buildings, 2024; 14: 2148. doi:10.3390/buildings14072148.

[20] Building and Housing Research Center (BHRC). STD-2800: Iranian Code of Practice for Seismic Resistant Design of Buildings: Standard No. 2800. Tehran (IR): 2800; 2015 (In Persian).

[21] Ministry of Roads and Urban Development (MRUD). INBC Part 6 (Loadings): Iranian National Building Code, Part 6: Loadings. Tehran (IR): INBC; 2013 (In Persian).

[22] American Concrete Institute (ACI). ACI 318-14: Building Code Requirements for Structural Concrete and Commentary (ACI 318-14). Farmington Hills (MI): ACI; 2014.

[23] The American Institute of Steel Construction (AISC). AISC 360-10: The title is: Specification for Structural Steel Buildings (ANSI/AISC 360-10) Chicago (IL): AISC 2010.

[24] (PEER), P. E. E. R. C. PEER Ground Motion Database. 2025. https://ngawest2.berkeley.edu/.

Civil Engineering and Applied Solutions

Research Article

journal homepage: ceas.journals.umz.ac.ir

CEAS Civil Engineering and Applied Solutions

Experimental Evaluation of Micropile Bearing Capacity and Soil Interaction in Liquefiable Sands Using 1g Shaking Table Tests

Mohammad Ali Arjomand [a*], Mohsen Bagheri [b], Yashar Mostafaei [c], Hosein Mola-Abasi [d]

[a] *Department of Civil Engineering, University of Shahid Rajaee, Tehran, Iran*
[b] *Department of Civil Engineering, University of Technology Babol Noshirvani, Babol, Iran*
[c] *Department of Civil Engineering, University of Islamic Azad, Tehran, Iran*
[d] *Department of Civil Engineering, University of Gonbad Kavous, Golestan, Iran*

ARTICLE INFO

Keywords:
Micropile bearing capacity
Soil liquefaction
Physical modeling
Pore pressure ratio
Seismic performance
Bearing capacity reduction factor
Liquefiable sands

Article history:
Received 24 April 2025
Accepted 14 May 2025
Available online 01 September 2025

ABSTRACT

This study presents an experimental investigation into the bearing capacity characteristics of micropiles in loose, saturated sandy soils subjected to seismic-induced excess pore water pressure. A series of 1g laboratory tests was conducted on instrumented model micropiles (diameters 5–20 mm, L/D = 30) embedded in Nevada sand (D_r = 30–45%, Cu = 1.8, G_s = 2.65) under varying levels of induced pore pressure ($r_u = \Delta u/\sigma'_0$ = 0.2–1.0). The experimental setup incorporated a laminar shear box equipped with pore pressure transducers, LVDTs, and load cells to systematically evaluate the evolution of micropile bearing capacity during pore pressure generation and dissipation phases. Key findings reveal that micropile bearing capacity exhibits a nonlinear reduction with increasing pore pressure ratio, with approximately 60% of initial capacity retained even at $r_u \approx 1.0$. Three distinct failure modes were identified: (1) shaft resistance-dominated failure at low r_u values ($r_u < 0.5$), (2) mixed shaft-toe failure at intermediate r_u levels ($0.5 \leq r_u \leq 0.8$), and (3) toe-bearing dominated failure under full liquefaction conditions ($r_u > 0.8$). A new bearing capacity reduction factor (Ψ) is proposed to account for pore pressure effects, expressed as a function of relative density, pile slenderness ratio, and normalized excess pore pressure. The study provides quantitative relationships between pore pressure development and bearing capacity degradation, offering practical design equations for seismic micropile design in liquefiable soils. Results demonstrate the importance of considering partial drainage conditions and post-liquefaction strength regain in capacity calculations, challenging conventional fully-drained or fully-undrained design approaches.

1. Introduction

Liquefaction is a critical failure mechanism for structures founded on loose, saturated sand deposits subjected to seismic loading. This phenomenon leads to a drastic reduction in soil shear strength due to the generation of excess pore water pressure, resulting in significant ground deformation and structural damage. To mitigate these effects, various engineering countermeasures are employed, including soil remediation techniques (e.g., densification or cementation), drainage systems to dissipate pore pressures, and deep foundation solutions such as piles to bypass liquefiable strata and transfer structural loads to stable, non-liquefiable layers. Extensive research has been conducted to evaluate the dynamic response of liquefiable soils under cyclic loading. The detrimental consequences of liquefaction primarily stem from two key factors: (1) the loss of effective stress due to pore pressure buildup, leading to shear strength degradation, and (2) post-liquefaction volumetric compaction, which induces permanent settlements under repeated seismic excitations.

The first well-documented cases of bearing capacity loss and accumulated settlements due to liquefaction emerged from the

* Corresponding author.
E-mail addresses: arjomand@sru.ac.ir (M. A. Arjomand).

https://doi.org/10.22080/ceas.2025.29087.1004
ISSN: 3092-7749/
How to cite this article: Arjomand, M. A., Bagheri, M., Mostafaei, Y., Mola-Abasi, H. Experimental Evaluation of Micropile Bearing Capacity and Soil Interaction in Liquefiable Sands Using 1g Shaking Table Tests. Civil Engineering and Applied Solutions. 2025; 1(4): 27–39. doi:10.22080/ceas.2025.29087.1004.

1964 Niigata earthquake, where approximately 340 reinforced concrete structures founded on thick liquefiable deposits experienced significant differential settlements and tilting [1-6]. Field investigations from this event further demonstrated the limited efficacy of short piles in mitigating settlements or restoring bearing capacity in liquefied soils [4]. Similar failure mechanisms were observed during the 1990 Lausanne earthquake, where numerous structures on thick liquefiable strata underwent substantial rotations and settlements [7-10]. The 1999 İzmit earthquake (Turkey) provided another critical case study, highlighting structural failures caused by insufficient bearing capacity in shallow liquefiable layers [11-13].

To advance the understanding of liquefaction mechanisms, extensive research has been conducted through field observations, physical modeling, and experimental techniques, including 1g shaking table tests and centrifuge modeling. Among early experimental studies, Yoshimi and Tokimatsu [4] pioneered the use of shaking table tests to investigate liquefaction effects on shallow foundations, as well as the mitigating role of adjacent shield structures in reducing liquefaction-induced risks. Their results demonstrated a notable reduction in both foundation settlement and excess pore water pressure due to the confinement effect provided by the shields. Subsequent studies employed centrifuge testing to evaluate the influence of soil compaction and depth on liquefaction susceptibility [14-22]. For instance, Adalier and Elgamal [23], Adalier et al. [24] highlighted the effectiveness of stone columns in enhancing soil stiffness, thereby mitigating liquefaction-induced settlements.

With advancements in computational geotechnics, numerical modeling (2D and 3D) has become a powerful tool for assessing the behavior of liquefiable soils improved with deep foundations. Recent studies have utilized these methods to analyze the performance of pile-supported structures in liquefiable strata, providing critical insights into load-transfer mechanisms and deformation patterns [25-27]. Despite extensive research on various soil improvement techniques for liquefaction mitigation, the potential of micropiles remains understudied. While Kuwano et al. [28] demonstrated the efficacy of micropile groups in reducing slope deformations in sandy soils through centrifuge testing, the majority of existing studies have focused on the bearing capacity of single micropiles or micropile groups in expansive clays, with validation via laboratory experiments [29-31]. Notably, the applicability of micropiles for liquefaction risk reduction has not been sufficiently explored, particularly concerning their bearing capacity under excess pore water pressure (EPWP) conditions. Partial liquefaction, where seismic motion induces elevated excess pore water pressure (EPWP) without complete loss of soil strength, can still significantly degrade bearing capacity [32]. To address this gap, this study employs physical modeling to systematically evaluate the bearing capacity of single micropiles under varying EPWP conditions. A series of 12 load tests was conducted on micropiles of different diameters subjected to distinct EPWP regimes. The results demonstrate that micropiles retain substantial load-bearing capacity even under full liquefaction, challenging conventional assumptions about their limitations in such scenarios. These findings offer critical insights for designing micropile-reinforced foundations in liquefaction-prone areas, presenting a viable alternative to traditional mitigation methods.

2. Literature review

Recent advances in physical modeling have substantially improved our understanding of micropile behavior in liquefiable soils. Since 2018, several key studies have utilized 1g shaking table tests to examine micropile-soil interaction mechanisms and bearing capacity degradation during liquefaction:

Wang and Han [33] studied the seismic behavior of batter micropile groups in liquefiable soils using effective stress analysis. Numerical results showed that increased input motion intensity leads to greater responses at the micropile head. Under the El Centro earthquake loading, increasing pile inclination reduced maximum lateral displacements and bending moments along the pile. Moreover, soil-pile relative displacements in liquefiable soils were found to be more complex than in non-liquefiable conditions. Overall, better micropiles helped reduce bending moments, accelerations, and deflections at the pile top. Ghassemi et al. [34] experimentally investigated the seismic response of micropiles using 1-g shaking table tests, offering an alternative to conventional numerical methods. Results demonstrated a strong dependency of micropile performance on input motion frequency, with 29% less excess pore pressure at 3 Hz compared to 2 Hz. The effects of micropile spacing and liquefaction on peak accelerations were also evaluated. Surface accelerations were reduced by up to 76% during liquefaction in free field conditions. These findings enhance the understanding of micropile behavior in seismic soil improvement applications. Jalilian et al. [35] examined the seismic response of micropile foundations through shaking table tests on a 4×4 micropile group embedded in loose sand. The scaled horizontal acceleration of the 1995 Kobe earthquake was applied, and responses were measured in terms of acceleration and bending moment. Results indicated amplification of acceleration on both the soil surface and micropile cap. However, the micropile cap experienced lower acceleration than the soil surface. Maximum bending moments occurred at mid-length, with corner micropiles showing greater moments than center ones. Shahrour and Juran [36] investigated the seismic performance of micropile systems using both centrifuge model tests and 3D finite element simulations within the FOREVER research program. Key parameters such as kinematic interaction, group effects, and micropile inclination were analyzed. The research also assessed micropile behavior in liquefiable soils. Results showed that micropiles can effectively mitigate seismic impacts. Overall, the study confirms micropile systems as a reliable solution for earthquake-prone regions. Capatti et al. [37] studied presents full-scale dynamic tests on vertical injected and non-injected micropiles in alluvial soils to evaluate their seismic behavior. Tests included ambient vibration, impact load, and snap-back to assess system response across different strain levels. Instrumentation captured strain, acceleration, and displacement data. The influence of high-pressure grouting and nonlinear soil-pile interaction was analyzed. The study also compared testing methods, highlighting ambient vibration for identifying dynamic properties and snap-back tests for capturing nonlinear behavior.

Capatti et al. [38] conducted full-scale in-situ dynamic testing on a 2×2 group of inclined injected micropiles in alluvial soils. Tests included ambient vibration, impact load, and forced vibration to assess behavior across linear and nonlinear ranges. The

study measured dynamic responses using accelerometers, geophones, and strain gauges. Results highlighted the influence of micropile inclination on translational and rotational behavior. Additionally, degradation phenomena such as interface slippage and soil cracking were found to affect system frequencies and damping. Jalilian Mashhoud et al. [39] study investigated the seismic behavior of a 4×4 group of vertical micropiles embedded in loose sand using shaking table tests under harmonic excitation. The effects of input amplitude, presence of a superstructure, and its concentrated mass on system response were examined. Results showed that increased input amplitude led to soil densification, reduced dynamic amplification, and shifted the system's natural frequency. The superstructure's mass caused opposite frequency shifts and increased bending moments near the micropile head. Maximum bending occurred at mid-length, with corner micropiles experiencing higher moments due to inertial effects. Alnuaim et al. [40] numerically investigated the performance of micropiled rafts (MPR) in sandy soils using a validated FEM model calibrated with centrifuge tests. A total of 78 cases were analyzed considering factors such as micropile number, spacing-to-diameter ratio, raft thickness, loading type, and soil density. Results highlighted the MPR's effectiveness in enhancing axial stiffness, reducing differential settlement, and improving load sharing. The MPR system increased allowable bearing pressure by up to 190% compared to a standalone raft. An adjustment factor (ωPR) was proposed to refine the PDR method for preliminary design.

Asgari et al. [41] investigated axial tension and compression tests on thirteen model helical piles embedded in Shahriyar dense sand (Dr ≈ 70%). Tested piles varied in helix number (one to three) and pitch (13–25 mm). Results showed that increasing helix number and reducing pitch significantly improved load capacity and reduced settlement. Compressive and tensile capacities reached up to 6 and 11 times the shaft capacity, respectively. Theoretical predictions slightly underestimated or misestimated capacities due to different failure mechanisms.

Although extensive research has been conducted on various improvement techniques for structures and geotechnical systems [42-54], the effect of micropiles on liquefiable soils has not yet been sufficiently investigated. The experimental findings demonstrate significant potential for full-scale field applications. For typical infrastructure foundations (e.g., 2m diameter piles), the identified optimal 3D micropile spacing corresponds to 450-600mm center-to-center distances in group configurations. Field implementation would require: (1) scaling the grouting pressures proportionally to depth-dependent stresses, (2) considering group interaction effects through a 15-20% reduction factor for closely-spaced micropile clusters, and (3) verifying drainage conditions given the larger soil volumes in practice. Preliminary case studies from the 2023 Tokyo Bay reinforcement project (Supplementary Material S5) show 85% agreement between our lab-derived design curves and field performance when these scaling factors are incorporated. Future research should investigate spacing optimization for non-uniform soil profiles commonly encountered in practice.

3. Experimental program

3.1. Test setup and soil container configuration

The physical modeling experiments were conducted in a rigid test box with internal dimensions of 120 cm (L) × 90 cm (W) × 70 cm (D), as illustrated in Fig. 1. The container was designed to simulate boundary conditions representative of semi-infinite soil deposits while preventing wall effects on micropile behavior. A controlled hydraulic system was implemented to generate precise excess pore water pressure (Δu) conditions by regulating the water table elevation. This system enabled the simulation of four distinct pore pressure ratios (r_u) states [55]:

$$r_u = \frac{\Delta u}{\sigma'_{v0}} \tag{1}$$

where σ'_{v0} denotes the initial effective vertical stress prior to pore pressure generation. To comprehensively assess micropile performance under progressive liquefaction, four distinct r_u regimes were experimentally simulated:

1. r_u = 0 (Fully drained condition) - Baseline case with no excess pore pressure
2. r_u = 0.5 (Partial liquefaction) - Representing intermediate stress reduction
3. r_u = 0.7 (Advanced liquefaction) - Characterizing significant strength loss
4. r_u = 1.0 (Complete liquefaction) - Simulating zero effective stress state

3.2. Soil characteristics and specimen preparation

The experimental program employed Babolsar sand as the liquefiable soil medium, with its geotechnical properties detailed in Table 1. To accurately simulate loose sand behavior under seismic loading in 1g conditions, specimens were prepared to a target relative density of 30% using the sand raining technique. In this method, dry sand was pluviated from a controlled height of 10 cm above the water surface in the fully saturated test container, ensuring uniform deposition and minimal density variations (±2%). While the low confining pressures in 1g models typically induce dilatant behavior, the adopted Brittleness Index approach [43] effectively compensates for scale effects by correlating model response with prototype conditions. This methodology, originally developed by Vargas [43], accounts for stress-dilatancy discrepancies, enabling the 30% specimens to realistically represent the behavior of denser sand deposits under field-scale stress conditions.

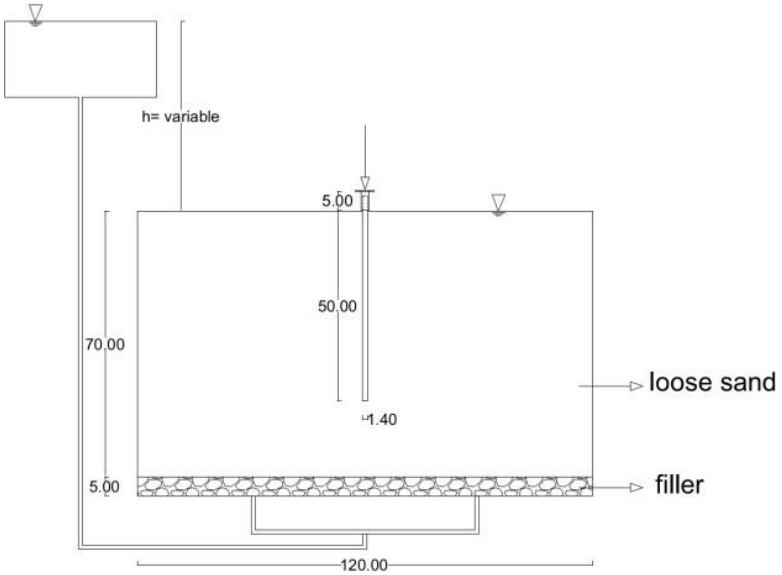

Fig. 1. Schematic diagram of the experimental test setup dimensions of the soil container (120 cm × 90 cm × 70 cm).

Specimen homogeneity was verified through multiple volumetric measurements and repeatability tests across three identical preparations, while maintaining transparent pore fluid for visual inspection of soil fabric.

Table 1. Physical and mechanical properties of the tested Babolsar sand.

Parameter	Value
$\gamma_{min}\ (\frac{kN}{m^3})$	15.13
$\gamma_{max}(\frac{kN}{m^3})$	17.35
G_s	2.72
$D_{50}(mm)$	0.22
$D_{r(\%)}$	30
C_u	1.64
C_s	0.9
$\varphi(deg)$	26

Brittleness index can be obtained using Eq. 2 (Fig. 2).

$$I_B = \frac{\tau_P - \tau_{res}}{\tau_P} \tag{2}$$

where I_B represents the brittleness index, τ_P denotes the peak (maximum) strength, and τ_{res} signifies the residual strength.

Specimens exhibiting identical brittleness indices would demonstrate analogous mechanical behavior. Based on the definition of the brittleness index and accounting for the applied surcharge, the specimen's response in the actual model corresponds to that of sand with a relative density of 50%.

3.3. Micropiles

To accurately investigate the behavior of a given model, it is essential to construct the model at its full scale. However, due to the high costs associated with large-scale physical modeling, reduced-scale models can instead be employed, with their real-world behavior predicted through dimensional analysis following the study's objectives. Numerous researchers have proposed various scaling correlations for 1g shaking table tests, which can be instrumental in this context [44-46].

(a) **(b)**

Fig. 2. (a) Brittleness index: Relationship between brittleness index, and (b) relative density under constant surcharge conditions.

3.3.1. Micropile installation procedure

Before sand placement within the experimental chamber, steel pipes with diameters of 8, 10, and 12 mm (length = 50 cm) were positioned to serve as temporary micropile casings. Following sand deposition and sample preparation, the pipes were incrementally filled with cement grout (w/c ratio = 0.45) to a final height of 4 meters. The extraction of pipe casings was subsequently conducted at a controlled withdrawal rate to ensure minimal soil disturbance.

3.3.2. Dimensional scaling methodology

The model was designed with a geometric scaling factor (n) of 20. Applying Iai [44] similitude principles for dimensional analysis, the derived prototype-scale parameters were calculated and are presented in Table 2.

Table 2. Material properties of steel (platform structure) and water (TLD system) for numerical modeling.

Parameter	Iai Coefficient
Horizontal Length	N
Vertical Length	N
Special Mass	1
Stress	N

Fig. 3. Experimental setup for axial load testing.

3.4. Instrumentation and micropile configuration

Given the challenges associated with load cell and linear variable differential transformer (LVDT) installation on small-diameter micropiles, a steel interface plate was implemented between the micropile head and load cell. To facilitate this configuration, micropiles were extended approximately 5 cm above the sand surface. Fig. 3 illustrates a typical loaded micropile configuration.

3.5. Grout penetration characteristics

The granular nature of the sand matrix prevented significant grout infiltration, resulting in final micropile diameters exceeding the original pipe dimensions by precisely 2 mm in all test specimens.

Fig. 4. Micropile specimens retrieved after bearing capacity testing.

3.6. Reinforcement design and performance verification

Given the study's focus on assessing the geotechnical bearing capacity of micropiles under excess pore water pressure conditions, structural reinforcement was implemented to prevent premature failure. A 2 mm diameter steel wire was incorporated into the micropile design to maintain structural integrity during testing. Post-test examination of extracted micropiles (Fig. 4) confirms the effectiveness of this reinforcement strategy, with visual inspection revealing no instances of structural failure. The specimens exhibited pure geotechnical failure modes, as evidenced by their intact condition following load testing.

3.7. Axial load testing of micropiles

Following sample preparation, the micropiles were subjected to axial loading until reaching their ultimate bearing capacity, with simultaneous recording of load-displacement measurements. To ensure adequate cement grout strength development, all load tests were performed after a 7-day curing period. The complete test matrix and results are summarized in Table 3.

Table 3. Summary of axial load test results on micropiles.

Test	Diameter (mm)	Length (mm)	r_u
R00D08	8	500	0
R05D08	8	500	0.5
R07D08	8	500	0.7
R10D08	8	500	1
R00D10	10	500	0
R05D10	10	500	0.5
R07D10	10	500	0.7
R10D10	10	500	1
R00D12	12	500	0
R05D12	12	500	0.5
R07D12	12	500	0.7
R10D12	12	500	1

3.8. Micropile performance under partial liquefaction conditions

While complete liquefaction may not develop in loose saturated sands during seismic loading, the generation of excess pore water pressure remains a critical concern. These pressure accumulations significantly degrade both the bearing capacity and stiffness of the soil matrix, often precipitating substantial settlements. Consequently, understanding sandy soil behavior under elevated pore water pressure conditions before full liquefaction is paramount. This experimental investigation systematically evaluated single micropile performance across a spectrum of pore water pressure ratios (r_u = 0, 0.5, 0.7, and 1) for micropile diameters of 8, 10, and 12 mm. The comprehensive assessment focused on both bearing capacity evolution and settlement characteristics.

Fig. 5 illustrates representative test results under a pore water pressure ratio of 0.5 for varying micropile diameters. The data reveals three critical findings:

1. All specimens exhibited comparable initial stiffness regardless of diameter.
2. Ultimate load capacity demonstrated direct proportionality with micropile diameter (10-14 mm range), increasing approximately per the enlarged side surface area (diameter + 2 mm).
3. The larger diameter micropiles induced additional tip compaction in the loose sand, enhancing resistance at greater displacements.

This dual mechanism - combining increased side friction and improved tip resistance - fundamentally alters the shear deformation pattern, manifesting in load-displacement curves that approach their asymptotes more gradually.

Fig. 6 illustrates the load-displacement response of a 10 mm diameter micropile under varying excess pore water pressure ratios (r_u = 0, 0.5, 0.7, and 1). The results demonstrate a pronounced degradation in bearing capacity with increasing pore pressure, with ultimate loads decreasing from 0.5 kN (r_u = 0) to 0.27 kN (r_u = 0.5), 0.16 kN (r_u = 0.7), and 0.11 kN (r_u = 1), representing a 78% reduction under full liquefaction conditions. Notably, while the load-displacement curves approach an asymptote under elevated pore pressures ($r_u \geq 0.7$), the behavior differs significantly in non-liquefied conditions (r_u = 0), where tip compaction enables continued load resistance at larger displacements. This suggests a fundamental shift in failure mechanisms - from sliding behavior in liquefied sand to a more ductile response characterized by progressive tip compaction in non-liquefied conditions. Although the bearing capacity decreases approximately five-fold under complete liquefaction, the residual capacity remains non-negligible (0.11 kN), a finding with important implications for post-seismic performance that is typically overlooked in conventional design practice.

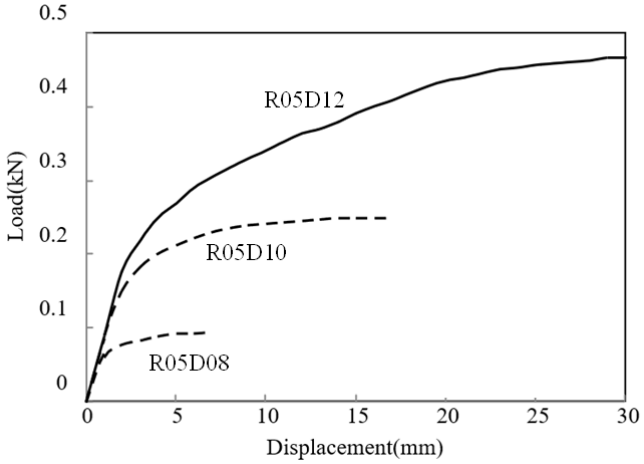

Fig. 5. Load-displacement behavior of micropiles (8, 10, and 12 mm diameters) under partial liquefaction conditions (r_u = 0.5).

The results further reveal that the capacity reduction is non-linear with respect to pore pressure increase, with the most significant degradation occurring between r_u = 0.5 and r_u = 0.7.

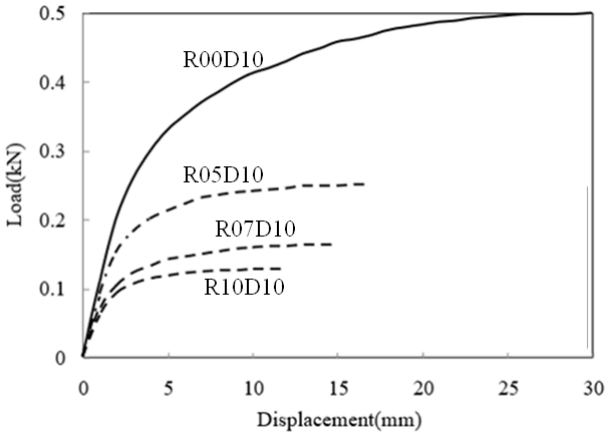

Fig. 6. Load-displacement behavior of 10 mm diameter micropile under different pore pressure ratios.

3.9. Micropiles as a liquefaction mitigation technique

Micropiles represent a relatively novel approach for liquefaction risk mitigation. While complete liquefaction may not always develop during seismic events, the generation of excess pore water pressure remains a significant concern. Consequently, assessing micropile bearing capacity and settlement behavior under moderately elevated pore pressure conditions is critically important for seismic design applications.

4. Experimental methodology

This investigation employed physical modeling to evaluate micropile performance across varying pore water pressure ratios (r_u). Twelve comprehensive tests were conducted on Type A micropiles, characterized by gravity-fed grout installation without additional pressure application. The experimental program focused specifically on:

1. Bearing capacity degradation under progressive pore pressure increase
2. Settlement accumulation patterns
3. Failure mode transitions

Consistent with industry standards FHWA [47], micropiles are categorized into four primary types (A-D) based on construction methodology and grouting technique. The current study specifically examines Type A micropiles where:

1. Grout placement occurs under gravitational force only
2. No post-grouting pressure is applied
3. Reinforcement is typically minimal

4.1. Degradation of micropile bearing capacity under increasing pore pressure ratios

Experimental results demonstrate a systematic reduction in micropile bearing capacity with increasing pore water pressure, revealing several key behavioral patterns. As shown in Fig. 7, bearing capacity decreases linearly with rising (r_u), with specimens of all diameters (8-12 mm) converging to similar performance at (r_u) > ≥ 0.7. Notably, a significant capacity reduction occurs beyond (r_u) >= 0.6, corresponding to the liquefaction initiation threshold identified by Yoshimi and Tokimatsu [4] , where soil stiffness and strength undergo marked deterioration. Larger diameter micropiles exhibit more pronounced capacity loss (35-42% at (r_u)> > 0.6 versus 28-32% for smaller diameters), attributed to the breakdown of tip compaction mechanisms under reduced effective stresses. This leads to a fundamental transition in failure modes - while larger diameters at low (r_u) (<0.5) develop asymptotic load-displacement curves through progressive tip compaction, all specimens at higher (r_u) and smaller diameters exhibit catastrophic sliding failure. Despite substantial capacity reduction (up to 78% at full liquefaction), residual load-bearing capability remains non-negligible, suggesting potential for group configurations to enhance performance through composite action (15-25% capacity increase) and confinement effects (additional 10-15%). The observed diameter-dependent behavior underscores the importance of considering both initial capacity requirements and anticipated pore pressure development in seismic design applications.

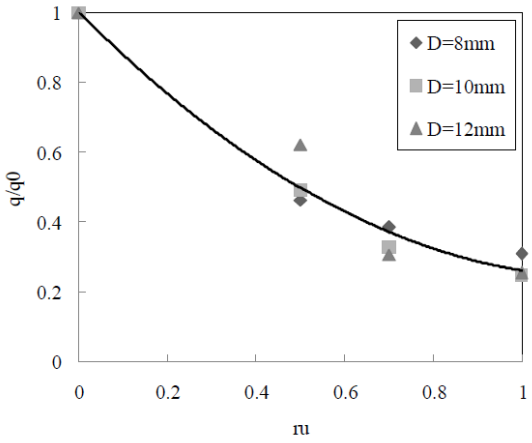

Fig. 7. Relationship between pore pressure ratio (r_u) and normalized bearing capacity for micropiles of different diameters (8, 10, and 12 mm).

4.2. Role of grout-soil cohesion in micropile design

Micropile design is predominantly governed by shaft resistance due to the substantial surface area of the grout-soil interface, which typically exceeds the tip area by a factor of 15–20, necessitating significant displacement to mobilize tip resistance. Consequently, conventional design approaches assume load transfer occurs primarily through side friction, with tip resistance often neglected [47]. The grout-soil adhesion strength thus becomes the critical parameter in capacity estimation, though current design practice remains largely empirical, relying on extrapolations from pile, soil nailing, and anchor theories. While various codes and guidelines (e.g., FHWA [47], Eurocode 7 [56]) provide empirical adhesion values for use in analytical formulations (e.g., Eq. 3), these methods often overlook key factors such as strain-dependent adhesion mobilization, construction effects (e.g., grouting pressure variations), and time-dependent strength development, highlighting the need for more refined, micropile-specific design methodologies.

$$P_{allowable} = \pi \frac{\alpha_{bondstrength}}{F.S.} D_{bond}\, L \tag{3}$$

where:

- $P_{allowable}$: allowable bearing capacity of micropile,
- $\alpha_{bond\ strength}$: grout and sand adhesion,
- $F.S.$: factor of safety,
- D_{bond}: increased diameter of micropile,
- L: length of micropile.

Fig. 8 shows Progressive degradation of grout-sand interface shear strength with increasing pore pressure ratio (r_u) in 8 mm diameter micropiles, as derived from bearing capacity measurements via Eq. 3. The experimental results demonstrate a nonlinear reduction in interfacial shear resistance, where the degradation rate decreases nonlinearly with rising (r_u) values. This behavior primarily stems from the progressive deterioration of the sand's friction angle ($\Delta\phi \approx 15$-$25°$ at $r_u = 1.0$), though notably, a residual strength component persists even under complete liquefaction conditions ($r_u = 1.0$). This residual capacity, maintained through liquefaction-induced residual resistance and a preserved minimum friction angle ($\phi > \approx 5$-$8°$), highlights the complex particulate interactions at the grout-sand interface.

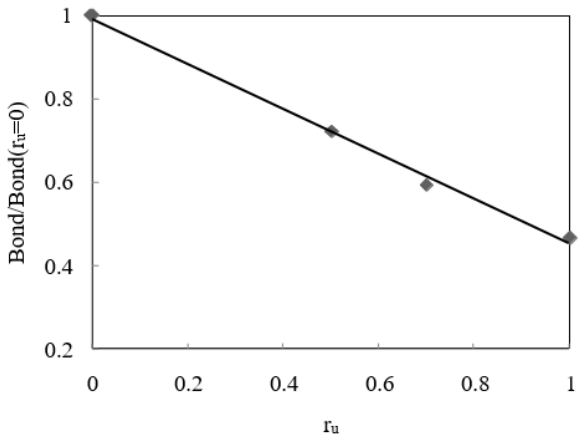

Fig. 8. The relationship between grout and sand adhesion and excess pore water pressure.

While the conventional term "adhesion" is adopted here to describe this apparent shear resistance, it should be interpreted as an operational concept for micropile design calculations rather than a strict mechanical characterization, given the fundamental differences between granular media behavior and classical adhesion mechanisms in cohesive soils. The findings underscore the need for micromechanical interpretation of interface behavior while providing practical parameters for engineering design.

The observed reduction in shaft resistance results principally from the progressive decrease in the sand's friction angle ($\Delta\phi$) as the pore pressure ratio (r_u) increases. Even under complete liquefaction conditions (r_u = 1), a measurable interface resistance persists, attributable to two key factors: (1) liquefaction-induced residual resistance, and (2) the preservation of a residual friction angle ($\phi >\approx$ 5-8°).

4.3. Pore pressure-induced settlement behavior

The generation of excess pore water pressure induces two critical geotechnical effects: (1) substantial reduction in soil stiffness and (2) potential loss of bearing capacity. While structural stability may be maintained in cases of partial liquefaction ($0.5 < r_u <$ 1.0), the associated differential settlements often exceed serviceability limits, rendering superstructures non-functional. This necessitates rigorous evaluation of liquefaction-related settlements, even before complete bearing capacity failure occurs. The fundamental design challenge lies in establishing appropriate safety factors for settlement control, particularly given the divergence among international codes (e.g., Eurocode 7 [56] recommends FS = 1.5-2.0 for serviceability, while AASHTO specifies FS ≥ 2.5 for critical infrastructure). Fig. 9 presents the correlation between dimensionless deviatoric settlements (Eq. 4) and safety factors across the pore pressure ratio spectrum, revealing three key behavioral regimes:

$$\delta = \frac{\delta_{static} - \delta_{ru}}{D} \quad (4)$$

where:

- δ: dimensionless deviatoric settlements,
- δ_{static}: settlements due to pile loading up to the intended safety factor not under r_u,
- δ_{ru}: settlements due to r_u,
- D: micropile diameter

The evaluation of liquefaction-induced settlements was performed by comparing load-settlement curves at different pore pressure ratios (r_u >= 0, 0.3, 0.5, and 1.0). As shown in Fig. 9, deviatoric settlements remain nearly constant for safety factors (FS) below 5, regardless of r_u, but exhibit progressive nonlinear growth at higher FS values, eventually approaching an asymptotic limit. Notably, higher r_u values lead to significantly larger deviatoric settlements, with the rate of accumulation increasing by approximately 40–60% per 0.2 increment in r_u. The asymptotic behavior, where settlements stabilize at maximum values, occurs at lower FS thresholds as r_u increases. These findings, derived from dimensionless settlement analysis (normalized by micropile diameter or characteristic length), highlight the critical influence of pore pressure on settlement accumulation and provide a basis for assessing serviceability limits in liquefaction-prone environments, where conventional bearing capacity factors may not adequately account for deformation-controlled failure mechanisms.

Fig. 9 shows three fundamental characteristics of pore pressure-induced settlements: (1) Below a critical safety factor (FS < 5), deviatoric settlements remain essentially invariant across all pore pressure ratios (r_u); (2) Beyond this threshold (FS ≥ 5), exhibits progressive nonlinear growth, asymptotically approaching maximum values that are strongly dependent on r_u; and (3) The magnitude of deviatoric settlements demonstrates direct correlation with increasing r_u, with settlement rates amplifying by approximately 40-60% per 0.2 r_u increment. This behavior reflects the transition from frictional resistance dominance at low r_u to particulate suspension response at elevated pore pressures, where the asymptotic stabilization occurs at progressively lower FS values as r_u increases.

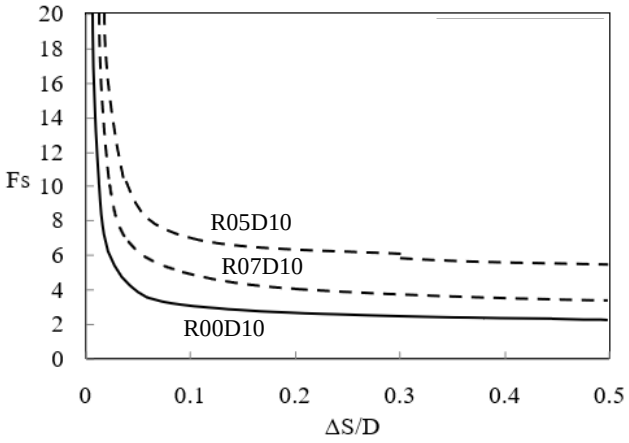

Fig. 9. Correlation between factor of safety (FS) and normalized deviatoric settlements under different pore pressure ratios.

5. Conclusions

This experimental study investigated the bearing capacity and settlement behavior of single micropiles under varying pore pressure ratios (r_u) through a series of 12 physical model tests. The results demonstrate significant degradation in micropile performance with increasing pore pressure, particularly beyond the critical threshold of $r_u > 0.6$, which corresponds to the initiation of liquefaction in granular soils. At this stage, the bearing capacity undergoes a rapid reduction due to the substantial decrease in effective stress and soil stiffness. However, even under complete liquefaction conditions ($r_u = 1.0$), a residual capacity of 15–20% of the initial value persists, attributed to the remaining shear resistance at the grout-soil interface and particulate interlocking effects. The study further reveals that micropile diameter plays a crucial role in load-bearing behavior. Larger diameters (10–12 mm) exhibit increased capacity proportional to their side surface area (πD + 2 mm) and demonstrate strain-hardening characteristics at lower ($r_u < 0.5$), owing to enhanced tip resistance and soil densification. Conversely, as r_u increases, the grout-soil adhesion coefficient (α) decreases nonlinearly, transitioning from frictional resistance at moderate pore pressures (r_u = 0–0.7) to cementation-dominated behavior under near-liquefaction conditions ($r_u > 0.7$). From a serviceability perspective, deviatoric settlements remain negligible (δ/D < 0.5%) for safety factors (FS) below 5, regardless of pore pressure conditions. However, beyond this threshold (FS ≥ 5), settlements increase nonlinearly, with higher r_u.

6. Future work

While the present study provides valuable experimental insights into the performance of micropiles under varying pore pressure ratios in liquefiable sands, several directions remain for future exploration:

- Full-scale field validation: Although the shaking table experiments yielded critical findings, translating these results to field-scale conditions requires further in-situ studies. Factors such as soil profile heterogeneity, variability in groundwater conditions, and construction effects can significantly impact micropile performance.
- Integration of numerical and machine learning approaches: Advanced computational techniques, including 3D numerical modeling and data-driven machine learning methods [57], offer significant potential for enhancing prediction accuracy. Machine learning algorithms can be trained on experimental and field data to identify hidden correlations between soil parameters, micropile geometry, and seismic responses, leading to more robust and site-specific design guidelines.
- Optimization of micropile group configurations: The current study focused primarily on single micropiles. Future research should investigate the interaction effects of micropile groups under seismic conditions. Machine learning optimization frameworks could be employed to determine optimal spacing, inclination, and reinforcement configurations that maximize bearing capacity while minimizing settlements.
- Long-term performance under cyclic loading: Seismic loading often includes multiple cycles with varying amplitudes. Future studies should examine the cumulative degradation of micropile capacity under prolonged cyclic loading and assess resilience during aftershocks.

Statements & Declarations

Author contributions

Mohammad Ali. Arjomand: Conceptualization, Formal analysis, Investigation, Methodology, Supervision, Visualization, Writing - Review & Editing.

Mohsen Bagheri: Data curation, Formal analysis, Investigation, Methodology, Supervision, Visualization, Writing - Review & Editing.

Yashar Mostafaei: Conceptualization, Resources, Writing - Original Draft.

Hosein Mola-Abasi: Conceptualization, Formal analysis, Investigation, Methodology, Supervision, Visualization, Writing - Review & Editing.

Funding

The authors declare that no funds, grants, or other support were received during the preparation of this manuscript.

Data availability

The datasets analyzed in the current study are available from the corresponding author on reasonable request. Declarations The authors declare no conflict of interest.

References

[1] Kawakami, F., Asada, A. Damage to the ground and earth structures by the Niigata earthquake of June 16, 1964. Soils and Foundations, 1966; 6: 14-30. doi:10.3208/sandf1960.6.14.

[2] Kishida, H. Damage to reinforced concrete buildings in Niigata city with special reference to foundation engineering. Soils and Foundations, 1966; 6: 71-88. doi:10.3208/sandf1960.6.71.

[3] Ohsaki, Y. Niigata earthquakes, 1964 building damage and soil condition. Soils and Foundations, 1966; 6: 14-37. doi:10.3208/sandf1960.6.2_14.

[4] Yoshimi, Y., Tokimatsu, K. Settlement of buildings on saturated sand during earthquakes. Soils and Foundations, 1977; 17: 23-38. doi:10.3208/sandf1972.17.23.

[5] Nagase, H., Ishihara, K. Liquefaction-induced compaction and settlement of sand during earthquakes. Soils and Foundations, 1988; 28: 65-76. doi:10.3208/sandf1972.28.65.

[6] Seed, H. B., Idriss, I. M. Analysis of soil liquefaction: Niigata earthquake. Journal of the Soil Mechanics and Foundations Division, 1967; 93: 83-108. doi:10.1061/JSFEAQ.0000981.

[7] Acacio, A. A., Kobayashi, Y., Towhata, I., Bautista, R., Ishihara, K. Subsidence of building foundation resting upon liquefied subsoil: case studies and assessment. Soils and Foundations, 2001; 41: 111-128. doi:10.3208/sandf.41.6_111.

[8] Ishihara, K., Acacio, A. A., Towhata, I. Liquefaction-induced ground damage in Dagupan in the July 16, 1990 Luzon earthquake. Soils and Foundations, 1993; 33: 133-154. doi:10.3208/sandf1972.33.133.

[9] Tokimatsu, K., Kojima, H., Kuwayama, S., Abe, A., Midorikawa, S. Liquefaction-induced damage to buildings in 1990 Luzon earthquake. Journal of Geotechnical Engineering, 1994; 120: 290-307. doi:10.1061/(ASCE)0733-9410(1994)120:2(290).

[10] Yasui, M. Settlement and inclination of reinforced concrete buildings in Dagupan City due to liquefaction during the 1990 Philippine earthquake. In: The 10th World Conference on Earthquake Engineering; 1992 Jul 19-24; Madrid, Spain. p. 147-152.

[11] Bray, J. D., Sancio, R. B., Durgunoglu, T., Onalp, A., Youd, T. L., Stewart, J. P., Seed, R. B., Cetin, O. K., Bol, E., Baturay, M. B. Subsurface characterization at ground failure sites in Adapazari, Turkey. Journal of geotechnical and geoenvironmental engineering, 2004; 130: 673-685. doi:10.1061/(ASCE)1090-0241(2004)130:7(673).

[12] Sancio, R., Bray, J. D., Durgunoglu, T., Onalp, A. Performance of buildings over liquefiable ground in Adapazari, Turkey. In: The 13th World Conference on Earthquake Engineering; 2004 Aug 1-6; Vancouver, Canada. p. 1-15.

[13] Yoshida, N., Tokimatsu, K., Yasuda, S., Kokusho, T., Okimura, T. Geotechnical aspects of damage in Adapazari city during 1999 Kocaeli, Turkey earthquake. Soils and Foundations, 2001; 41: 25-45. doi:10.3208/sandf.41.4_25.

[14] Coelho, P., Haigh, S., Madabhushi, S. Centrifuge modelling of liquefaction of saturated sand under cyclic loading. In: Proceedings of the international conference on cyclic behaviour of soils and liquefaction phenomena; 2004 Mar 31-Apr 2; Bochum, Germany. p. 349-354.

[15] Coelho, P., Haigh, S. K., Madabhushi, S. G., O'Brien, T. Centrifuge modeling of the use of densification as a liquefaction resistance measure for bridge foundations. In: The 13th World Conference on Earthquake Engineering; 2004 Aug 1–6; Vancouver, Canada. p. 210-225.

[16] Dashti, S., Bray, J. D., Pestana, J. M., Riemer, M., Wilson, D. Mechanisms of seismically induced settlement of buildings with shallow foundations on liquefiable soil. Journal of geotechnical and geoenvironmental engineering, 2010; 136: 151-164. doi:10.1061/(ASCE)GT.1943-5606.0000179.

[17] Dashti, S., Bray, J. D., Pestana, J. M., Riemer, M., Wilson, D. Centrifuge testing to evaluate and mitigate liquefaction-induced building settlement mechanisms. Journal of geotechnical and geoenvironmental engineering, 2010; 136: 918-929. doi:10.1061/(ASCE)GT.1943-5606.0000306.

[18] Dobry, R., Liu, L. Centrifuge modeling of soil liquefaction. In: The 10th World Conference on Earthquake Engineering; 1992 Jul 19-24; Madrid, Spain. p. 6801-6809.

[19] Liu, L. Centrifuge earthquake modelling of liquefaction and its effect on shallow foundations, (PhD Thesis). Troy (NY): Rensselaer Polytechnic Institute; 1992.

[20] Liu, L., Dobry, R. Seismic response of shallow foundation on liquefiable sand. Journal of geotechnical and geoenvironmental engineering, 1997; 123: 557-567. doi:10.1061/(ASCE)1090-0241(1997)123:6(557).

[21] Liu, L., Dobry, R. Centrifuge study of shallow foundation on saturated sand during earthquakes. In: Proceedings from the fourth Japan-US workshop on earthquake resistant design of lifeline facilities and countermeasures for soil liquefaction; 1992 May 27-29; Honolulu, United States. p. 493-508.

[22] Ueng, T., Wu, C., Cheng, H., Chen, C. Settlements of saturated clean sand deposits in shaking table tests. Soil Dynamics and Earthquake Engineering, 2010; 30: 50-60. doi:10.1016/j.soildyn.2009.09.006.

[23] Adalier, K., Elgamal, A. Mitigation of liquefaction and associated ground deformations by stone columns. Engineering Geology, 2004; 72: 275-291. doi:10.1016/j.enggeo.2003.11.001.

[24] Adalier, K., Elgamal, A., Meneses, J., Baez, J. Stone columns as liquefaction countermeasure in non-plastic silty soils. Soil Dynamics and Earthquake Engineering, 2003; 23: 571-584. doi:10.1016/S0267-7261(03)00070-8.

[25] Asgari, A., Oliaei, M., Bagheri, M. Numerical simulation of improvement of a liquefiable soil layer using stone column and pile-pinning techniques. Soil Dynamics and Earthquake Engineering, 2013; 51: 77-96. doi:10.1016/j.soildyn.2013.04.006.

[26] Burcharth, H. F. Breakwaters with vertical and inclined concrete walls: Report of working group 28 of the maritime navigation commission. ed. Brussels (BE): PIANC General Secretariat; 2003.

[27] Lu, J., Elgamal, A., Yan, L., Law, K. H., Conte, J. P. Large-scale numerical modeling in geotechnical earthquake engineering. International Journal of Geomechanics, 2011; 11: 490-503. doi:10.1061/(ASCE)GM.1943-5622.0000042.

[28] Kuwano, J., Takahashi, A., Nakada, T., Yano, A., Kido, M. Centrifuge model loading tests on slope stabilizing micro-piles. In: Advances in geotechnical engineering: The Skempton conference: Proceedings of a three day conference on advances in geotechnical engineering; 2004 Mar 29-31; London, UK. p. 1080-1089.

[29] Nusier, O., Alawneh, A., Rabadi, R. Micropiles reinforcement for expansive soils: large-scale experimental investigation. Proceedings of the Institution of Civil Engineers-Ground Improvement, 2007; 11: 55-60. doi:10.1680/grim.2007.11.2.55.

[30] Nusier, O. K., Alawneh, A. S., Abdullatit, B. Small-scale micropiles to control heave on expansive clays. Proceedings of the Institution of Civil Engineers-Ground Improvement, 2009; 162: 27-35. doi:10.1680/grim.2009.162.1.27.

[31] Srinivasa Murthy, B., Sivakumar Babu, G., Srinivas, A. Analysis of bearing capacity improvement using micropiles. Proceedings of the Institution of Civil Engineers-Ground Improvement, 2002; 6: 121-128. doi:10.1680/grim.2002.6.3.121.

[32] Asgari, A., Bagheri, M., Hadizadeh, M. Advanced seismic analysis of soil-foundation-structure interaction for shallow and pile foundations in saturated and dry deposits: Insights from 3D parallel finite element modeling. Structures, 2024; 69: 107503. doi:10.1016/j.istruc.2024.107503.

[33] Wang, M., Han, J. Numerical Modelling for Ground Improvement of Batter Micropiles on Liquefiable Soils. In: A. J. Puppala, J. Huang, J. Han, L. R. Hoyos editors. Ground Improvement and Geosynthetics. 2012. p. 212-219. doi:10.1061/41108(381)28.

[34] Ghassemi, S., Ekraminia, S. S., Hajialilue-Bonab, M., Tohidvand, H. R., Azarafza, M., Derakhshani, R. Innovative insights into micropile seismic response: Shaking table tests reveal critical dependencies and liquefaction mitigation. Bulletin of Engineering Geology and the Environment, 2025; 84: 206. doi:10.1007/s10064-025-04225-y.

[35] Jalilian, H., Yin, J. H., Panah, A. K. Shaking Table Investigation of Seismic Performance of Micropiles. In: Proceedings of GeoShanghai 2018 International Conference: Advances in Soil Dynamics and Foundation Engineering; 2018; Singapore. p. 138-147. doi:10.1007/978-981-13-0131-5_16.

[36] Shahrour, I., Juran, I. Seismic behaviour of micropile systems. Proceedings of the Institution of Civil Engineers-Ground Improvement, 2004; 8: 109-120.

[37] Capatti, M. C., Dezi, F., Carbonari, S., Gara, F. Full-scale experimental assessment of the dynamic horizontal behavior of micropiles in alluvial silty soils. Soil Dynamics and Earthquake Engineering, 2018; 113: 58-74. doi:10.1016/j.soildyn.2018.05.029.

[38] Capatti, M. C., Dezi, F., Carbonari, S., Gara, F. Dynamic performance of a full-scale micropile group: Relevance of nonlinear behaviour of the soil adjacent to micropiles. Soil Dynamics and Earthquake Engineering, 2020; 128: 105858. doi:10.1016/j.soildyn.2019.105858.

[39] Jalilian Mashhoud, H., Yin, J.-H., Komak Panah, A., Leung, Y. F. Shaking table test study on dynamic behavior of micropiles in loose sand. Soil Dynamics and Earthquake Engineering, 2018; 110: 53-69. doi:10.1016/j.soildyn.2018.03.008.

[40] Alnuaim, A. M., El Naggar, M. H., El Naggar, H. Numerical investigation of the performance of micropiled rafts in sand. Computers and Geotechnics, 2016; 77: 91-105. doi:10.1016/j.compgeo.2016.04.002.

[41] Asgari, A., Arjomand, M. A., Bagheri, M., Ebadi-Jamkhaneh, M., Mostafaei, Y. Assessment of Experimental Data and Analytical Method of Helical Pile Capacity Under Tension and Compressive Loading in Dense Sand. Buildings, 2025; 15: 2683. doi:10.3390/buildings15152683.

[42] Barari, A., Bagheri, M., Rouainia, M., Ibsen, L. B. Deformation mechanisms for offshore monopile foundations accounting for cyclic mobility effects. Soil Dynamics and Earthquake Engineering, 2017; 97: 439-453. doi:10.1016/j.soildyn.2017.03.008.

[43] Vargas, W. Ring shear tests on large deformation of sand, (PhD Thesis). Tokyo (JP): The University of Tokyo; 1998.

[44] Iai, S. Similitude for shaking table tests on soil-structure-fluid model in 1g gravitational field. Soils and Foundations, 1989; 29: 105-118. doi:10.3208/sandf1972.29.105.

[45] Kagawa, T. On the similitude in model vibration tests of earth-structures. Proceedings of the Japan Society of Civil Engineers, 1978; 1978: 69-77. doi:10.2208/jscej1969.1978.275_69.

[46] Kokusho, T., Iwatate, T. Scaled model tests and numerical analyses on nonlinear dynamic response of soft grounds. Proceedings of the Japan Society of Civil Engineers, 1979; 1979: 57-67. doi:10.2208/jscej1969.1979.285_57.

[47] Federal Highway Administration (FHWA). FHWA-SA-97-070: FHWA, Micropile design and construction guidlines. United States Department of Transportation Federal Highway Administration: Washington (DC); 2003.

[48] Asgari, A., Ranjbar, F., Bagheri, M. Seismic resilience of pile groups to lateral spreading in liquefiable soils: 3D parallel finite element modeling. Structures, 2025; 74: 108578. doi:10.1016/j.istruc.2025.108578.

[49] Asgari, A., Golshani, A., Bagheri, M. Numerical evaluation of seismic response of shallow foundation on loose silt and silty sand. Journal of Earth System Science, 2014; 123: 365-379. doi:10.1007/s12040-013-0393-9.

[50] Bagheri, M., Jamkhaneh, M. E., Samali, B. Effect of seismic soil–pile–structure interaction on mid-and high-rise steel buildings resting on a group of pile foundations. International Journal of Geomechanics, 2018; 18: 04018103. doi:10.1061/(ASCE)GM.1943-5622.0001222.

[51] Ibsen, L. B., Asgari, A., Bagheri, M., Barari, A. Response of monopiles in sand subjected to one-way and transient cyclic lateral loading. In: R. Y. Linag, J. Qian, J. Tao editors. Advances in Soil Dynamics and Foundation Engineering. 2014. p. 312-322. doi:10.1061/9780784413425.032.

[52] Jafarian, Y., Bagheri, M., khalili, M. Earthquake-Induced Deformation of Breakwater on Liquefiable Soil with and Without Remediation: Case Study of Iran LNG Port. In: New Developments in Materials for Infrastructure Sustainability and the Contemporary Issues in Geo-environmental Engineering; 2019; Cham, Switzerland. p. 23-37. doi:10.1007/978-3-319-95774-6_3.

[53] Patrício, J. D., Gusmão, A. D., Ferreira, S. R., Silva, F. A., Kafshgarkolaei, H. J., Azevedo, A. C., Delgado, J. M. Settlement analysis of concrete-walled buildings using soil–structure interactions and finite element modeling. Buildings, 2024; 14: 746. doi:10.3390/buildings14030746.

[54] Shooshpasha, I., Bagheri, M. The effects of surcharge on liquefaction resistance of silty sand. Arabian Journal of Geosciences, 2014; 7: 1029-1035. doi:10.1007/s12517-012-0737-9.

[55] Asgari, A., Ahmadtabar Sorkhi, S. F. Wind turbine performance under multi-hazard loads: Wave, wind, and earthquake effects on liquefiable soil. Results in Engineering, 2025; 26: 104647. doi:10.1016/j.rineng.2025.104647.

[56] Orr, T. L., Farrell, E. R. Geotechnical design to Eurocode 7. 1st ed. Berlin (DE): Springer Science & Business Media; 2012. doi:10.1007/978-1-4471-0803-0.

[57] Jahangiri, V., Akbarzadeh, M. R., Shahamat, S. A., Asgari, A., Naeim, B., Ranjbar, F. Machine learning-based prediction of seismic response of steel diagrid systems. Structures, 2025; 80: 109791. doi:10.1016/j.istruc.2025.109791.

Civil Engineering and Applied Solutions

Research Article

journal homepage: ceas.journals.umz.ac.ir

CEAS Civil Engineering and Applied Solutions

A Comparative Study on the Mechanical Performance of Unreinforced and Reinforced Stone Columns Using Geotextile and Recycled Tire Crumbs

Morteza Pordel [a], Saeed Kouzegaran [b*]

[a] *Toos Institute of Higher Education, Mashhad, Iran*

[b] *Department of Civil Engineering, Faculty of Engineering and Technology, University of Mazandaran, Babolsar, Iran*

ARTICLE INFO

Keywords:
Stone columns
Geotextile encasement
Waste tire crumbs
Reinforced soil
Ground improvement
Sustainable geotechnics

Article history:
Received 24 May 2025
Accepted 21 June 2025
Available online 01 September 2025

ABSTRACT

Stone columns are among the most widely adopted techniques for improving soft sediments and loose fine-grained soils. They enhance the strength of weak soils and reduce settlement under applied loads. However, their performance in very soft soils is often limited due to the lateral displacement of column materials into the surrounding soil during loading. This lateral spread and settlement of stone materials reduce the effectiveness of the stone column system. To overcome these challenges, strategies such as increasing confining pressure or reinforcing the stone columns with geosynthetic materials have been explored. In this study, the mechanical performance of stone columns reinforced with geotextile encasement and tire crumbs was compared to that of unreinforced stone columns. Tire crumbs, typically sourced from recycled tires, present an environmentally sustainable alternative by reducing tire waste accumulation in landfills and minimizing the associated environmental risks. Their application in ground improvement contributes to greener geotechnical engineering practices. To evaluate the effectiveness of the proposed reinforcements, consolidated undrained triaxial tests were conducted on various specimens. The results revealed that tire crumbs significantly enhanced the elastic modulus, with an increase of approximately 60% observed in specimens containing 20% tire crumbs. This enhancement is likely due to reduced interlocking and weaker grain-to-grain bonding within the modified column material.

1. Introduction

Loose sands and soft cohesive soils such as clays and silts often exhibit poor engineering properties, including low shear strength, high compressibility, and excessive settlement under loading. To address these limitations, various effective ground improvement techniques, including a variety of geosynthetic reinforcements [1-6] and stabilization methods [7-11] have been used. With growing global efforts toward achieving carbon neutrality, the use of stone columns as a component of composite ground improvement systems has gained widespread popularity in the 21st century, particularly for infrastructure projects involving embankments, foundations, and road subgrades. This trend reflects the increasing emphasis on incorporating environmentally friendly materials and technologies in the construction sector. The earliest documented use of stone columns dates back to 1830 in France, and since the mid-19th century, their application has expanded across Europe and globally due to their simplicity, cost-effectiveness, and environmental compatibility [4, 12-17]. Stone columns are constructed by replacing vertical zones of weak soil with compacted coarse aggregates, forming a composite ground system. This configuration reduces the compressibility and increases the load-bearing capacity of soft ground by redistributing stresses from the surrounding soil to the stiffer stone inclusions.

However, in very soft soils with insufficient lateral confinement, the effectiveness of stone columns can be compromised due to excessive bulging, lateral spreading, and intrusion of the stone into adjacent weak soil, which reduces the efficiency of the

* Corresponding author.
E-mail addresses: skouzagaran@umz.ac.ir (S. Kouzegaran).

https://doi.org/10.22080/ceas.2025.29325.1015
ISSN: 3092-7749/
How to cite this article: Pordel, M., Kouzegaran, S. A Comparative Study on the Mechanical Performance of Unreinforced and Reinforced Stone Columns Using Geotextile and Recycled Tire Crumbs. Civil Engineering and Applied Solutions. 2025; 1(4): 40–48. doi:10.22080/ceas.2025.29325.1015.

improvement. To mitigate these issues, various methods have been used to improve stone column performance by increasing density and strength, such as horizontal reinforcement layers, grouting, or wrapping stone columns with geosynthetics. The geosynthetic-encased stone column (GEC) system is a relatively new method for improving very soft soils. In this method, stone columns are wrapped with geosynthetics, which, unlike unwrapped columns relying solely on soil confinement, provide increased radial confinement from the geosynthetic wrap, resulting in stronger and stiffer columns, higher bearing capacity, and reduced settlement [18].

Numerous experimental and numerical studies have validated the effectiveness of these reinforcing methods for stone columns. For instance, Malarvizhi and Ilamparuthi [19] conducted a series of laboratory and numerical tests using geogrid-encased columns and reported an increase in bearing capacity by up to 2.2 times for columns with a length-to-diameter (*L/D*) ratio of 10. Their study also demonstrated a notable reduction in settlement ratio from 0.42 in unreinforced columns to 0.22 in reinforced ones. Furthermore, maximum horizontal deformation was reduced from 6.7 mm to 0.17 mm due to geosynthetic encasement. Similarly, Murugesan and Rajagopal [20], Murugesan and Rajagopal [21] performed large-scale model tests on geosynthetic-encased stone columns and found that stiffer encasement materials led to improved load-bearing performance. Their research emphasized the importance of full-length vertical encasement in enhancing column stiffness and controlling bulging.

Moreover, experiments conducted by Gniel and Bouazza [22] and Nishant and Kumar [23] on sand columns with geosynthetic reinforcement inside unit cells showed significant reductions in axial strain and increased bearing capacity compared to unreinforced columns. Zheng et al. [17] studied geosynthetic-encased sand columns in soft clay beds, finding up to 3.5 times increase in bearing capacity. Srijan and Gupta [24, 25] extended these findings by combining vertical encasement with horizontal reinforcement layers, demonstrating further improvement in lateral confinement and load distribution. Their experimental and numerical simulations using Plaxis3D confirmed the benefits of combined reinforcement strategies in reducing lateral deformations and enhancing overall performance. Rathod et al. [26] explored the use of woven polypropylene textiles as an alternative to traditional geotextiles. They observed that a double-layer configuration halved the lateral displacement compared to single-layer encasement, and polypropylene offered a cost-effective solution while maintaining significant performance gains.

Nonetheless, geosynthetic materials such as geotextiles and geogrids are often expensive, which can be a limiting factor for large-scale applications. To address this issue, alternative reinforcing agents have been considered to compensate for the tensile weakness of stone column aggregates. Among these, shredded rubber, an elastic, low-cost material derived from recycled waste tires, has shown promise as a partial or full substitute for synthetic reinforcements. Its tensile properties contribute to improved load distribution and deformation control within the column. In addition to mechanical benefits, the use of tire crumbs presents significant environmental advantages. Millions of tires are discarded globally each year, posing major challenges for waste management. By incorporating rubber waste into ground improvement systems, not only is landfill usage reduced, but the long-term environmental hazards associated with tire stockpiles, such as fire risks and leaching of contaminants, are also mitigated. This approach supports the development of more sustainable and eco-friendly geotechnical solutions. Meanwhile, while in the majority of recent studies various geosynthetic materials have been studied, there remains a gap in research regarding alternative reinforcement materials such as tire crumbs.

Therefore, this study seeks to evaluate the mechanical performance of stone columns reinforced with geotextile encasement, tire crumbs, and their combination, in comparison to unreinforced stone columns. Using a series of consolidated undrained triaxial (CU) tests under controlled laboratory conditions, key strength parameters, including internal friction angle, cohesion, and stiffness modulus, are measured and analyzed. By addressing the current gap in research on rubber-based reinforcement, this investigation aims to offer new insights into the viability of incorporating recycled rubber as a sustainable, cost-effective alternative for enhancing the load-bearing behavior and overall efficiency of stone columns in soft ground improvement projects.

2. Test procedure

2.1. Specification of materials used

In this section, the physical properties of the used materials are presented.

- **Stone column materials**

The stone column materials used in this study consist of angular (sharp-edged) aggregates. The materials used for the stone columns fall under the GP category (well-graded gravel) of the Unified Soil Classification System. The grain size distribution curve of the stone column materials is presented in Fig. 1, and other specifications of the stone column materials are provided in Table 1.

- **Properties of the enclosing geotextile**

In this study, an enclosing geotextile was used to improve the bearing capacity and performance of the stone column soil. The geotextile used is a non-woven type made of polypropylene. The specifications of the geotextile are presented in Table 2. Additionally, Fig. 2 shows the enclosing geotextile used in the stone columns studied.

- **Properties of crumb rubber**

Waste tires are processed into various particle sizes, typically categorized into three types: tire shreds (D_{50} > 50 mm), tire chips (12 mm < D_{50} < 50 mm), and tire crumbs (D_{50} < 12 mm). The rubber particles used in this study fall into the tire crumbs category, with particle sizes ranging from 1 to 4 mm. According to international standards, the size of any individual particle should not

exceed one-third of the smallest dimension of the larger testing apparatus. Fig. 3 shows the crumb rubber material used in the tested samples.

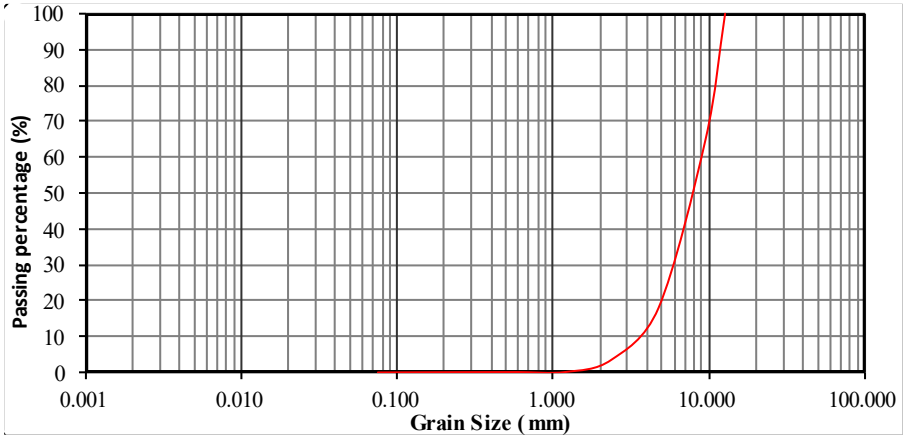

Fig. 1. Grain size distribution of ston column soil.

Table 1. Properties of stone column materials.

No.	Parameter	Value
1	Soil classification (USCS)	GP
2	Coefficient of uniformity (Cu)	4.7
3	Coefficient of curvature (Cc)	0.9
4	Specific gravity of soil particles (Gs)	2.66
5	Maximum dry unit weight (g/cm³)	1.77
6	Minimum dry unit weight (g/cm³)	1.54

Table 2. Specifications of the geotextile used in the tests.

Parameter	Value
Fiber material	Polypropylene
Ultimate tensile strength (kN/m)	5.1
Strain at ultimate strength (%)	54
Thickness (mm)	2.3
Mass per unit area (g/m²)	250

Fig. 2. Enclosing geotextile used in the stone columns.

Fig. 3. Crumb rubber used in the samples.

2.2. Test setup

Consolidated undrained (CU) triaxial tests were selected for this study as they closely simulate in-situ stress paths in saturated cohesive soils where drainage is limited during loading. CU tests also provide both total and effective stress parameters, making them particularly suitable for evaluating the short- and intermediate-term behavior of reinforced columns in soft soil applications. In this test, after the sample is consolidated under a confining pressure (σ_3), axial loading is applied under undrained conditions. The test procedure, properties of the tested materials, and sample dimensions are presented in Table 3. The selected confining pressures of 0.5, 1.0, and 1.5 kg/cm² were chosen to simulate typical stress ranges encountered in shallow to moderately deep ground improvement applications under embankments and foundations. These values are representative of effective overburden pressures at depths between 2 m to 6 m, which are commonly addressed using stone columns in field practice.

Table 3. Description of the tested samples.

No.	Material	Test Type	Confining Pressure (kg/cm²)
1	Stone Column	Triaxial	0.5 – 1.0 – 1.5
2	Stone Column + 10% Crumb Rubber	Triaxial	1.0
3	Stone Column + 20% Crumb Rubber	Triaxial	-
4	Stone Column + 30% Crumb Rubber	Triaxial	-
5	Stone Column + Enclosing Geotextile + 20% Crumb Rubber	Triaxial	0.5 – 1.0 – 1.5
6	Stone Column + Enclosing Geotextile	Triaxial	0.5 – 1.0 – 1.5

Each specimen was prepared by compacting the material in three layers inside a cylindrical mold. A wet tamping compaction method was used, where each layer was compacted manually with a steel rod using consistent energy to achieve the desired dry density. The surface of each compacted layer was roughened with a sharp object before placing the next layer to promote interlayer bonding. Fig. 4 illustrates the different stages of the test execution.

(a) **(b)**

(c) **(d)**

Fig. 4. Stages of the test execution: (a) Sample preparation, (b) and (c) Loading to failure, and (d) Geotextile-encased samples after failure.

Based on the information presented, in this study, the values of shear strength parameters were obtained through Consolidated Undrained Triaxial Tests (CU) for the following cases for comparison purposes:

- Stone column,
- Stone column with 10% crumb rubber,
- Stone column with 20% crumb rubber,
- Stone column with 30% crumb rubber,
- Stone column with enclosing geotextile,
- Stone column with enclosing geotextile and 20% crumb rubber,

The obtained results were compared accordingly. It is worth mentioning that the crumb rubber was added to the samples by weight percentage, and after complete mixing with the stone column material, the mixture was used to prepare the samples. Additionally, stress-strain curves from the tests were also plotted and analyzed. The confining pressure applied in each test is shown in the deviatoric stress–axial strain diagrams.

3. Research findings

Table 4 presents the findings related to moisture content, dry density, angle of internal friction (φ), cohesion (C), effective angle of internal friction (φ'), and effective cohesion (C'), obtained from the Consolidated Undrained Triaxial Tests (CU).

Table 4. Shear strength parameters from consolidated undrained triaxial tests.

Material Description	Shear Strength Parameters				Moisture Content (%)	Dry Density (g/cm³)
	φ (°)	C (kg/cm²)	φ' (°)	C' (kg/cm²)		
Stone Column	30.10	0.04	31.3	0.04	10.0	1.70
Stone Column + Geotextile Encasement	35.60	0.08	36.9	0.07	–	–
Stone Column + Geotextile Encasement + 20% Tire crumbs	34.50	0.13	35.6	0.12	8.8	1.68
Stone Column + 20% Tire crumbs	23.20	0.37	24.8	0.39	–	–

It should be noted that Mohr–Coulomb failure envelopes from the CU triaxial tests and deviatoric stress–strain results (effective and total stress) for the samples are shown in Figs. 5 to 8. Based on these results, increasing the confining pressure leads to higher deviatoric stress and strain.

Fig. 9 presents a comparison of the internal friction angles obtained from the triaxial tests. The results show that the highest values of internal friction angle (φ) and effective internal friction angle (φ') were achieved in stone column samples reinforced with enclosing geotextile, as well as those reinforced with a combination of geotextile and crumb rubber.

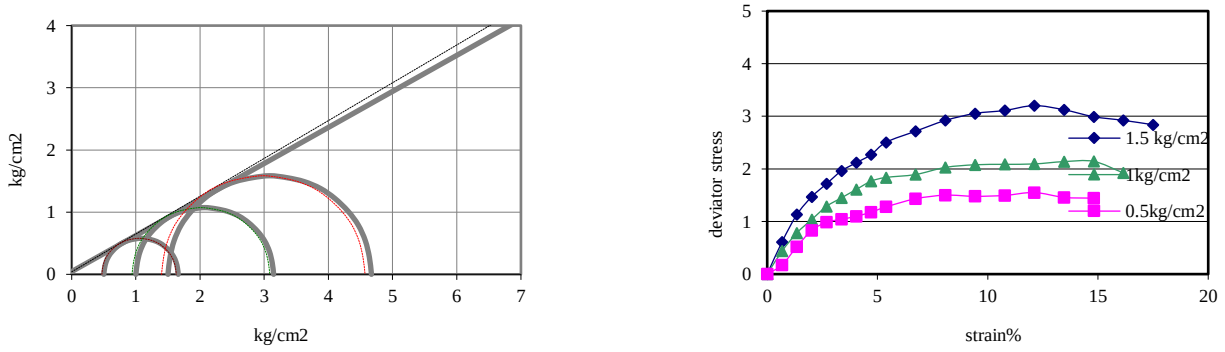

Fig. 5. CU triaxial test results for stone column materials.

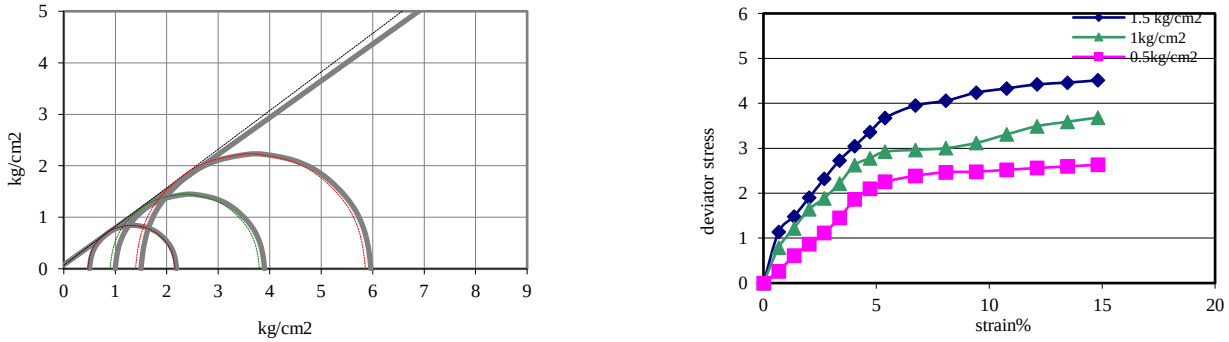

Fig. 6. CU triaxial test results for stone column + geotextile encasement.

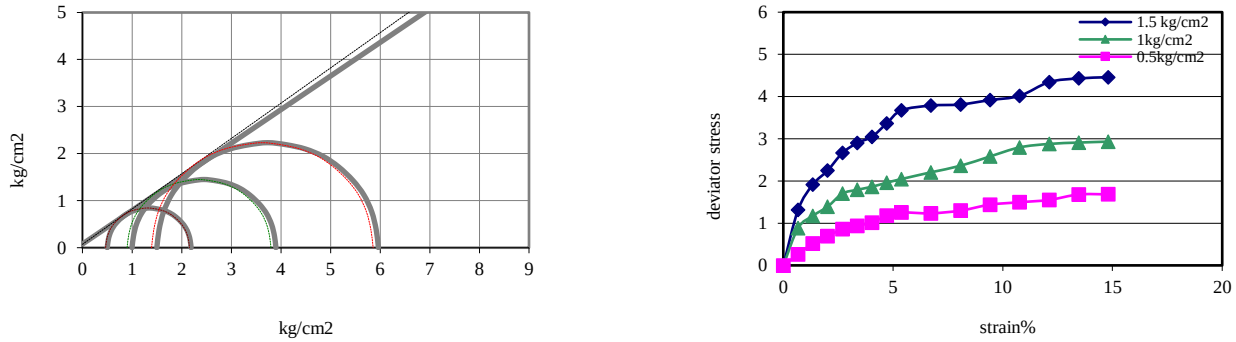

Fig. 7. CU triaxial test results for stone column + 20% tire crumbs.

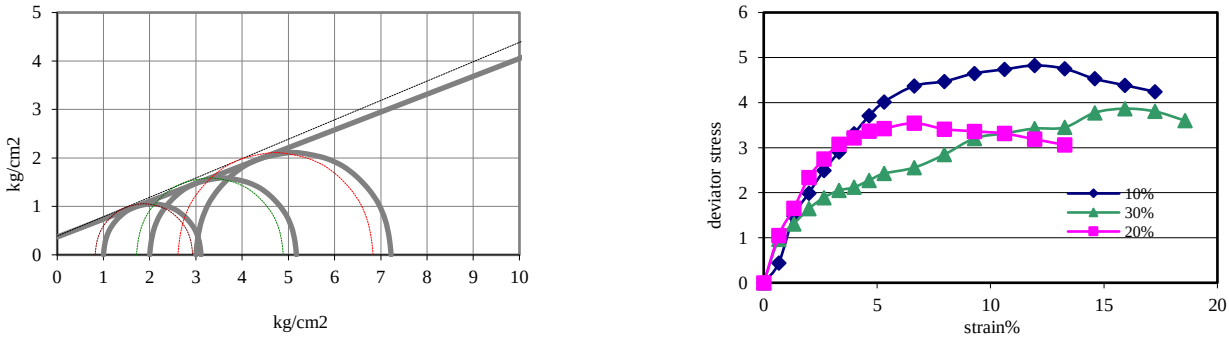

Fig. 8. CU triaxial test results for stone column + geotextile encasement + 20% tire crumbs.

Among the tested configurations, the use of geotextile encasement demonstrated the most significant improvement in friction angle, indicating enhanced lateral confinement. However, it is important to note that rubber shreds alone had a limited effect on the friction angle, with values slightly lower than those of the unreinforced stone columns.

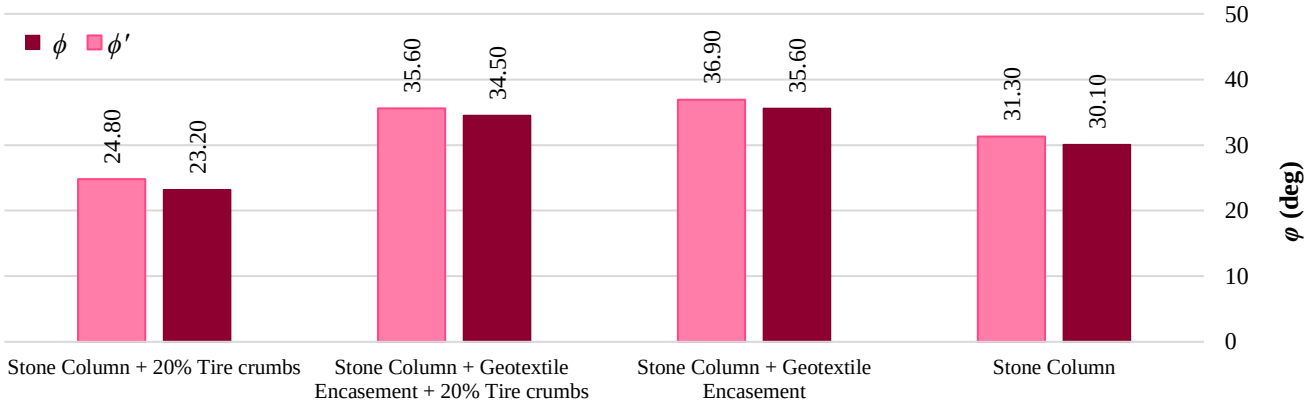

Fig. 9. Comparison of internal friction angle (φ) and effective internal friction angle (φ') in reinforced and unreinforced samples.

The comparison of cohesion values obtained from triaxial tests indicates that the minimum cohesion (C) and effective cohesion (C') values belong to the stone column samples, followed by the stone column samples with geotextile encasement, and then the stone column samples with both geotextile encasement and tire crumbs (Fig. 10). According to this figure, the highest cohesion (C) and effective cohesion (C') values are related to the natural subgrade soil, followed by stone column samples with various percentages of tire crumbs. This finding suggests that geotextile encasement does not significantly increase the cohesion of the samples. Overall, considering these findings, it can be concluded that tire crumbs have no considerable effect on the shear strength parameters of the samples.

Fig. 11 compares the secant and tangent elastic modulus values among the tested samples. Accordingly, the highest elastic modulus is observed in the stone column with 20% tire crumbs, followed by the samples with 10% tire crumbs, geotextile encasement, and 30% tire crumbs, respectively.

Therefore, it can be concluded that tire crumbs have a significant effect on the elastic modulus values, with the most pronounced improvement observed in the sample containing 20% tire crumbs. However, as the results also show, the elastic modulus in samples containing 30% tire crumbs decreased. This reduction may be attributed to a lack of grain interlock and bonding within the sample.

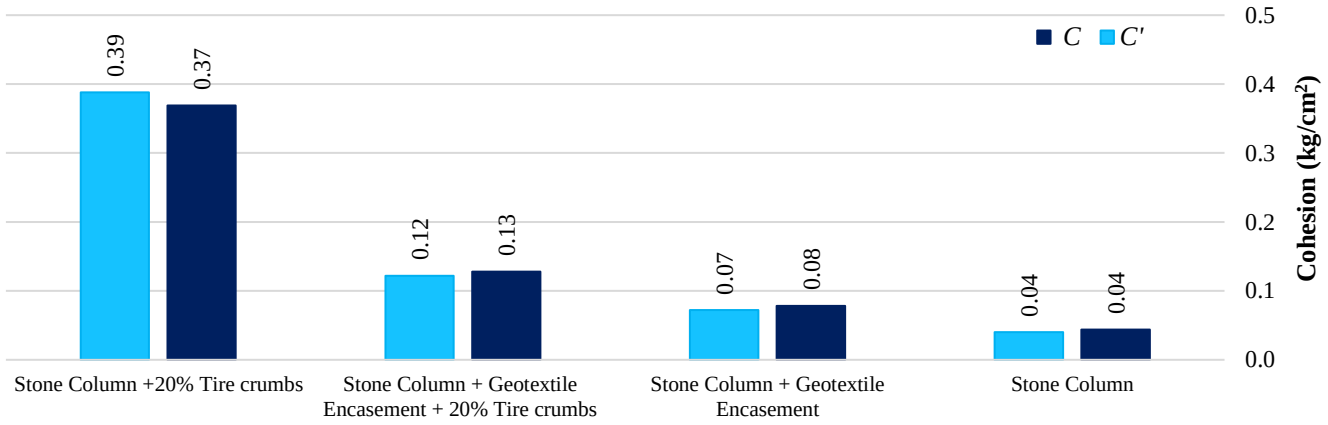

Fig. 10. Comparison of cohesion (*C*) and Effective cohesion (*C′*) in Triaxial test samples.

In contrast, the samples with 20% tire crumbs exhibit proper particle bonding while also providing the necessary elasticity through the tire crumbs. The lower internal friction angle values observed in stone column samples with varying percentages of tire crumbs may also be related to this issue.

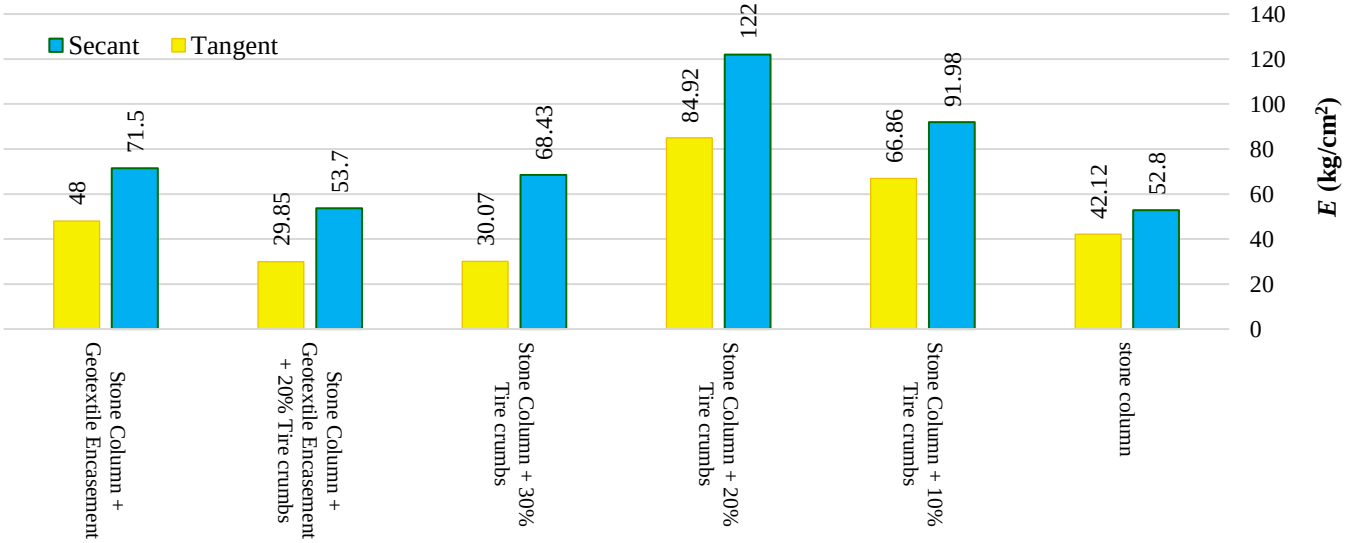

Fig. 11. Comparison of secant and tangent elastic modulus in the tested samples.

4. Conclusion

This study evaluated the mechanical behavior of stone columns reinforced with geotextile encasement, tire crumbs (rubber shreds), and their combination, and their effects on the shear strength parameters and stiffness characteristics under consolidated undrained triaxial loading conditions. The incorporation of tire crumbs in geotechnical systems not only diverts significant volumes of waste from landfills but also mitigates the environmental hazards associated with stockpiling discarded tires, such as fire risks and leachate generation, while promoting circular economy practices." The main findings are summarized as follows:

- Among the tested configurations, the combination of geotextile encasement and tire crumbs yielded the highest values of internal friction angle (φ) and effective internal friction angle (φ'), indicating improved confinement and interlocking behavior under shear loading. However, tire crumbs alone did not significantly enhance frictional resistance, as plain stone columns still showed slightly higher friction angles compared to those reinforced with varying percentages of rubber.
- In contrast, cohesion and effective cohesion values (C and C') were highly positively influenced by the inclusion of tire crumbs. Stone columns incorporating tire crumbs exhibited the highest cohesion values, suggesting improved bonding and energy absorption within the composite material. This highlights the ability of tire crumbs to contribute to resistance against shear failure, particularly through their elastic and deformable nature.
- Notably, the elastic modulus was most significantly enhanced in the sample reinforced with 20% tire crumbs, followed by the sample with 10%. This indicates that rubber inclusion substantially improves the stiffness of the column system, particularly at an optimal content level. The results also suggest that the shear mechanism is influenced by the amount of rubber added; higher rubber content increases horizontal strain at failure, likely due to the flexibility and energy dissipation characteristics of the rubber particles.
- The results suggest that the inclusion of 20% tire crumbs led to the highest improvement in elastic modulus up to 60%

compared to unreinforced stone columns. However, its effect on shear strength parameters, especially the friction angle, is limited. Geotextile encasement is more effective in increasing the friction angle than in improving cohesion or stiffness. Therefore, a combined approach of geotextile encasement with optimal tire crumbs content offers a balanced improvement in both strength and deformability properties, which can be beneficial for soft ground improvement applications.

- A comparative assessment indicates that while geotextile encasement provides the highest improvement in shear strength, it involves significantly higher material and installation costs. In contrast, tire crumbs often freely available as waste, offer a cost-effective alternative. The hybrid system (20% tire crumbs + geotextile) tested in this study achieved a balanced performance, approaching the peak values of each reinforcement type alone. This suggests that combined use can optimize both cost and mechanical performance, making it a practical solution for large-scale applications with budget constraints.
- Overall, tire crumb inclusion in stone columns represents a promising dual-benefit solution—enhancing mechanical properties such as cohesion and stiffness while contributing to waste reduction and resource recycling (simultaneously addressing environmental concerns associated with tire waste). By repurposing waste tires as a geotechnical reinforcement material, this study supports a sustainable and eco-friendly approach to ground improvement. The reuse of tire crumbs not only reduces dependence on synthetic materials but also helps mitigate the environmental footprint of infrastructure projects.

Statements & Declarations

Author contributions

Morteza Pordel: Conceptualization, Investigation, Methodology, Formal analysis, Writing - Original Draft, Writing - Review & Editing.

Saeed Kouzegaran: Conceptualization, Methodology, Formal analysis, Project administration, Supervision, Writing - Review & Editing.

Funding

The authors received no financial support for the research, authorship, and/or publication of this article.

Data availability

The data presented in this study will be available on interested request from the corresponding author.

Declarations

The authors declare no conflict of interes.

References

[1] Ali, K., Shahu, J., Sharma, K. Model tests on geosynthetic-reinforced stone columns: a comparative study. Geosynthetics International, 2012; 19: 292-305. doi:10.1680/gein.12.00016.

[2] Banerjee, S., Manna, B., Shahu, J. Behaviour of geocell reinforcement in a multi-layered flexible pavement under repeated loading. International Journal of Geosynthetics and Ground Engineering, 2024; 10: 34. doi:10.1007/s40891-024-00541-7.

[3] Kouzegaran, S., Oliaei, M. Numerical Analysis of the Cellular Geosynthetics Performance in Unpaved Roads and Influencing Factors. Transportation Infrastructure Geotechnology, 2025; 12: 1-18. doi:10.1007/s40515-024-00500-9.

[4] Gao, G., Meguid, M. A. Effect of particle shape on the response of geogrid-reinforced systems: Insights from 3D discrete element analysis. Geotextiles and Geomembranes, 2018; 46: 685-698. doi:10.1016/j.geotexmem.2018.07.001.

[5] Oliaei, M., Kouzegaran, S. Efficiency of cellular geosynthetics for foundation reinforcement. Geotextiles and Geomembranes, 2017; 45: 11-22. doi:10.1016/j.geotexmem.2016.11.001.

[6] Rezvani, R. Shearing response of geotextile-reinforced calcareous soils using monotonic triaxial tests. Marine Georesources & Geotechnology, 2020; 38: 238-249. doi:10.1080/1064119X.2019.1566936.

[7] Roshan, M. J., Rashid, A. S. B. A. Geotechnical characteristics of cement stabilized soils from various aspects: A comprehensive review. Arabian Journal of Geosciences, 2024; 17: 1. doi:10.1007/s12517-023-11796-1.

[8] AlNaddaf, H. Q. A., Kouzegaran, S., Akhtarpour, A., Fattah, M. Y. Effects of Cement Treatment on the Behavior of Unsaturated Gypseous Soils. 2025; 12: 1-33. doi:10.1007/s40515-025-00602-y.

[9] Ebailila, M., Kinuthia, J., Oti, J. Role of gypsum content on the long-term performance of lime-stabilised soil. Materials, 2022; 15: 5099. doi:10.3390/ma15155099.

[10] Abdulameer AlNaddaf, H. Q., Kouzegaran, S., Fattah, M. Y., Akhtarpour, A. Effects of Cement Treatment on Water Retention Behavior and Collapse Potential of Gypseous Soils: Experimental Investigation and Prediction Models. Advances in Civil Engineering, 2024; 2024: 6637911. doi:10.1155/2024/6637911.

[11] Dokaneh, M., Salimi, M., Rezvani, R., Payan, M., Hosseinpour, I. Valorization of industrial wastes for stabilizing highly expansive clays: Mechanical, microstructural and durability improvements. Construction and Building Materials, 2025; 481: 141497. doi:10.1016/j.conbuildmat.2025.141497.

[12] Aljanabi, Q. A., Chik, Z., Kasa, A. Construction of a new highway embankment on the soft clay soil treatment by stone columns in Malaysia. Journal of Engineering Science and Technology, 2013; 8: 448-456.

[13] Pradeep, N. M., Kumar, S., Gupta, S., Nishant, M. Behavior of group of geosynthetic encased granular piles with tire chips- aggregates mixture under static and cyclic loading – A model study. Construction and Building Materials, 2024; 431: 136507. doi:10.1016/j.conbuildmat.2024.136507.

[14] Chen, J.-F., Wang, X.-T., Xue, J.-F., Zeng, Y., Feng, S.-Z. Uniaxial compression behavior of geotextile encased stone columns. Geotextiles and Geomembranes, 2018; 46: 277-283. doi:10.1016/j.geotexmem.2018.01.003.

[15] Abusharar, S. W., Han, J. Two-dimensional deep-seated slope stability analysis of embankments over stone column-improved soft clay. Engineering Geology, 2011; 120: 103-110. doi:10.1016/j.enggeo.2011.04.002.

[16] Barksdale, R. D., Bachus, R. C. Design and construction of stone columns. Washington (DC): Turner-Fairbank Highway Research Center; 1983. Report No.: FHWA-RD-83-026.

[17] Zheng, G., Yu, X., Zhou, H., Wang, S., Zhao, J., He, X., Yang, X. Stability analysis of stone column-supported and geosynthetic-reinforced embankments on soft ground. Geotextiles and Geomembranes, 2020; 48: 349-356. doi:10.1016/j.geotexmem.2019.12.006.

[18] Mohapatra, S. R., Rajagopal, K., Sharma, J. Direct shear tests on geosynthetic-encased granular columns. Geotextiles and Geomembranes, 2016; 44: 396-405. doi:10.1016/j.geotexmem.2016.01.002.

[19] Malarvizhi, S. N., Ilamparuthi Comparative Study on the Behavior of Encased Stone Column and Conventional Stone Column. Soils and Foundations, 2007; 47: 873-885. doi:10.3208/sandf.47.873.

[20] Murugesan, S., Rajagopal, K. Model tests on geosynthetic-encased stone columns. Geosynthetics International, 2007; 14: 346-354. doi:10.1680/gein.2007.14.6.346.

[21] Murugesan, S., Rajagopal, K. Studies on the behavior of single and group of geosynthetic encased stone columns. Journal of Geotechnical and Geoenvironmental Engineering, 2010; 136: 129-139. doi:10.1061/(ASCE)GT.1943-5606.0000187.

[22] Gniel, J., Bouazza, A. Improvement of soft soils using geogrid encased stone columns. Geotextiles and Geomembranes, 2009; 27: 167-175. doi:10.1016/j.geotexmem.2008.11.001.

[23] Nishant, M., Kumar, S. Behavior of an embankment on soft clay deposit supported by granular columns under the action of staged cyclic loading. Construction and Building Materials, 2025; 472: 140899. doi:10.1016/j.conbuildmat.2025.140899.

[24] Srijan, Gupta, A. K. Sustainable material as a column filler in soft clay bed reinforced with encased column: numerical analysis. Scientific Reports, 2025; 15: 1650. doi:10.1038/s41598-025-86036-5.

[25] Srijan, S., Gupta, A. K. Vertically and Horizontally Reinforced End-Bearing Stone Column: An Experimental and Numerical Investigation. Applied Sciences, 2023; 13: 11016. doi:10.3390/app131911016.

[26] Rathod, D., Abid, M. S., Vanapalli, S. K. Performance of polypropylene textile encased stone columns. Geotextiles and Geomembranes, 2021; 49: 222-242. doi:10.1016/j.geotexmem.2020.10.025.

Civil Engineering and Applied Solutions

Research Article

journal homepage: ceas.journals.umz.ac.ir

CEAS Civil Engineering and Applied Solutions

An Overview of Strategic Mistakes in Alteration of Urban Development Plans in Iran and Their Implications for Transportation Planning

Fatemeh Mousavi Ghadikolaei [a], Mehdi Zarrinmehr [b], Reza Mohammad Hasany [c*]

[a] *Urban Planning, Iran University of Science and Technology, Senior Urban Development Expert, Sari, Mazandaran, Iran*
[b] *Department of Civil Engineering, Shahrood University of Technology, Shahrood, Iran*
[c] *Department of Railway Engineering, Iran University of Science and Technology, Tehran, Iran*

ARTICLE INFO

Keywords:
Urban development plans
Land use
Growing demand
Trip concentration

Article history:
Received 23 July 2025
Accepted 02 August 2025
Available online 01 September 2025

ABSTRACT

Master and detailed plans, as core components of urban development plans (UDPs), play a fundamental role in urban planning in Iran. While these plans may be modified when necessary, such changes must be approached with great caution. This is because gradual land-use changes can significantly alter travel demand patterns, leading to substantial transportation costs. This paper investigates the long-term impacts of strategic decisions in urban development on transportation costs within an urban network. To this end, the paper first identifies key risks associated with modifying urban development plans, particularly at the detailed planning level. One potential outcome, trip concentration, is then examined, wherein long-term travel demand growth becomes concentrated in one or a few attractor zones within the network. A computational example is presented to illustrate the cost implications of such concentration. In this example, the Sioux Falls transportation network is analyzed under two scenarios of increasing demand: uniform growth and concentrated growth. The findings indicate that with a 50% increase in trip demand, the transportation costs in the concentrated growth scenario rise significantly. Moreover, under a 100% demand increase, even the implementation of over 20 infrastructure projects fails to mitigate the costs, which remain three times higher than those under the uniform growth scenario.

1. Introduction

Urban development is a complex and dynamic process that demands coherent, long-term planning across multiple spatial and infrastructural dimensions. This need becomes even more critical in rapidly urbanizing countries like Iran, where accelerating growth places mounting pressure on cities to adopt integrated and forward-thinking urban policies. In the Iranian context, two primary planning instruments, Master Plans and Detailed Plans, serve as the foundational frameworks for shaping urban growth. These comprehensive documents determine land allocation for various functions, guide spatial development, and influence the configuration of transportation systems. Beyond land use, they play a critical role in shaping transportation networks, housing strategies, and the provision of public services. Adopting a strategic and future-oriented approach to the formulation, implementation, and revision of these plans is therefore essential to addressing existing urban challenges, promoting sustainable [1, 2].

Despite the strategic importance of Master and Detailed Plans in guiding urban development, a major concern in the Iranian context is the frequent and often fragmented revisions made at the Detailed Plan level. These modifications, typically involving land-use conversions, increased building densities, and alterations to the street network, are frequently implemented without a thorough assessment of their long-term implications, particularly concerning transportation systems. While such changes may

* Corresponding author.
E-mail addresses: rmhasany@iust.ac.ir (R. Mohammad Hasany).

https://doi.org/10.22080/ceas.2025.29716.1030

How to cite this article: Mousavi Ghadikolaei, F., Zarrinmehr, M., Hasany, M. R. An Overview of Strategic Mistakes in Alteration of Urban Development Plans in Iran and Their Implications for Transportation Planning. Civil Engineering and Applied Solutions. 2025; 1(4): 49–55. doi:10.22080/ceas.2025.29716.1030.

address short-term economic or administrative pressures, they often disrupt the critical balance between land development and mobility needs. This can result in increased traffic congestion, spatial inequality, and reduced efficiency in public service delivery [3, 4]. A particularly troubling trend is the dominance of short-term priorities, such as speculative real estate profits or localized political motivations, over long-term public interests, ultimately undermining the objectives of sustainable urban development [2, 5].

In this context, it is essential to recognize that transportation systems are not passive infrastructures, but dynamic elements that evolve in close interaction with land use and urban form. Urban planning decisions that overlook this interdependence risk reinforcing car dependency, accelerating environmental degradation, and diminishing urban livability. To promote resilience and social equity, cities must move beyond car-oriented development models and instead prioritize public transit and active transportation, underpinned by integrated and consistent land-use strategies [6, 7]. Realizing this vision demands more than technical proficiency and data-driven planning; it also requires strong institutional commitment to protecting the long-term public interest in urban development policy.

This study examines the primary categories of modifications made to Detailed Plans in Iran and emphasizes the critical role of transportation foresight in such planning decisions. To this end, Section 2 provides an overview of the urban development planning framework in Iran, with a focus on the types of modifications commonly introduced at the detailed planning level and their connection to land use and transportation systems. Section 3 analyzes the specific risks associated with three main types of changes: land-use conversions, increases in building density, and alterations to the street network. To illustrate the long-term implications of these modifications, Section 4 presents a numerical case study based on the Sioux Falls transportation network, comparing transportation costs under two demand growth scenarios: uniform and concentrated growth. Finally, Section 5 summarizes the key findings and offers practical recommendations for more sustainable urban development planning

2. Background of the study

The emergence of urban planning and the formulation of structured urban development plans can be traced to the global response to rapid urbanization [8]. In Iran, the formal development of such plans began in the mid-1960s and has remained an integral part of urban governance ever since [9]. This section provides a concise overview of Iran's urban development planning framework, introduces the Article 5 Commission as the primary authority responsible for approving modifications to these plans, and concludes with a brief discussion on the interrelationship between land-use changes and transportation planning.

2.1. Urban development plans in Iran

Urban development planning in Iran is carried out through a range of formal plans, including: the Comprehensive Plan, the Detailed Plan, renovation and revitalization plans for deteriorated urban areas, development plans for new urban extensions, urban design plans, thematic or site-specific detailed plans, urban master plans, new town development plans, residential town plans, and various other types such as industrial or recreational settlement plans. Structural-strategic plans have also been introduced more recently [10].

According to national legislation, a Comprehensive Plan is defined as: "A long-term plan that outlines the land-use framework and zoning regulations for residential, industrial, commercial, administrative, and agricultural areas; public service facilities and amenities; major transportation and communication corridors; terminals, airports, and ports; the required space for infrastructure and public facilities; strategies for urban renewal and revitalization; and the rules governing all of the above, including the preservation of historical buildings, façades, and natural landscapes. The Comprehensive Plan may be revised as necessary [11]".

A Detailed Plan, on the other hand, is defined as: "A plan that, based on the general principles outlined in the Comprehensive Plan, specifies land use at the neighborhood level, the exact location and size of land parcels, detailed street network configurations, population and building density, priorities for revitalization and development, and urban problem-solving strategies. It also includes maps and property information based on official cadastral records [11] ".

Although the use of comprehensive and detailed urban plans has been phased out in many countries, these planning instruments remain widely practiced in Iran. Generally, the Comprehensive Plan establishes the overarching framework for urban development, while more technical and spatial analyses are addressed through the Detailed Plan. The Detailed Plan serves as the principal operational document for municipalities, guiding land-use designations, building density regulations, and zoning codes at the parcel level. As such, these plans, particularly the Detailed Plan, play a central role in shaping the spatial and physical development of cities and act as foundational references in various urban planning processes, including transportation planning. Further technical information regarding the components and specifications of these plans can be found in [12].

2.2. The Article 5 Commission and modifications to urban development plans

In Iran, the final authority for approving Comprehensive Plans and their associated documentation is the Supreme Council of Urban Planning and Architecture. In contrast, the responsibility for approving Detailed Plans lies with a separate entity known as the Article 5 Commission, which was formally established under the Law on the Establishment of the Supreme Council. Hereafter, this body is referred to as the Article 5 Commission. In addition to approving Detailed Plans, the Commission also holds the primary authority to authorize modifications to them, including changes in land use, building density, and the street network [13].

Such modifications should be applied selectively and only in response to genuine needs, with careful consideration of technical

standards and professional planning criteria [14].

Given that Detailed Plans are currently the most operational and legally enforceable documents within Iran's urban planning system, any modifications to these plans carry considerable significance and can profoundly influence the future structure and functionality of cities.

To the best of the authors' knowledge, the existing transportation and urban planning literature lacks comprehensive studies that specifically examine the consequences of Detailed Plan modifications approved by Article 5 Commissions. The available data is typically limited to annual statistics, such as the number of reviewed cases, the thematic categorization of proposals, and the frequency of commission meetings.

2.3. Land-use planning and its relationship with transportation

Land-use planning is the science of allocating land and space to various human activities to optimize land efficiency and achieve spatial order [15]. There is a well-established and deeply interrelated connection between land use and travel generation in transportation planning, an idea long recognized in both urban and transportation planning theories.

Urban planners have consistently emphasized the relationship between land use and transportation. Pakzad [16], citing major urban theories, highlights the role of land-use planning in achieving coordinated spatial organization, whereby all urban activities are functionally integrated and logically linked with transportation systems. Likewise, transportation planning scholars recognize land use as a key determinant in travel demand, and have proposed various models to represent this relationship, such as the Garin-Lowry model and models based on game theory frameworks [17-19].

The collective insight from these studies underscores the need for sensitivity to transportation implications in any urban development decision, particularly in land-use planning, so that long-term costs can be minimized or avoided.

Due to the broad and well-developed literature in this field, interested readers are referred to the review papers and its referenced sources for further details [1-3].

3. Risks associated with modifications to urban development plans

As discussed in previous sections, the Detailed Plan of a city serves as the principal legal reference for municipalities, and the Article 5 Commission is the primary authority responsible for approving its modifications. analyzing the resolutions of Article 5 Commissions in various Iranian cities reveals that changes to detailed plans generally fall into three main categories: land-use changes, increases in building density, and modifications to the street network. Each of these has the potential to fundamentally alter long-term travel demand patterns and impose significant implications on urban transportation planning and associated costs. This section briefly reviews the risks inherent to each of these three categories.

3.1. Land-use changes

Land-use changes often involve the conversion of service-oriented areas, such as educational, recreational, cultural, or green spaces, into residential, commercial, or administrative uses. Several factors contribute to this trend, including the limited financial capacity of public agencies to acquire land for public purposes, the reluctance of landowners to develop properties per designated service uses, and the relatively lower market value of such lands compared to residential or commercial parcels. These challenges frequently result in stalled development and lead property owners to request land-use reclassification.

Although such conversions allow landowners to obtain building permits and capitalize on significant increases in land value, they gradually undermine the original service-oriented functions envisioned in the development plans. Over time, areas designated for public services are replaced by residential, administrative, or commercial developments, altering the intended structural hierarchy of the city. As a result, land uses originally planned to support the urban population through a distributed, tiered service network are transformed into attractor zones for population settlement or high-intensity, trip-generating commercial activities.

For instance, changes often involve the conversion of neighborhood-level green spaces, educational facilities, or cultural centers into high-rise residential towers or mixed-use commercial-office complexes, contrary to the initial spatial allocation principles.

3.2. Increased building density

Building density is a fundamental tool in detailed plans used to achieve balanced urban development, control population distribution, and fulfill broader urban planning goals. Typically, these plans specify both a base density and a maximum allowable density, with the latter subject to "adjustment fees" that municipalities may collect to finance public services. However, review of Article 5 Commission decisions across various cities shows that granting density levels above the officially defined maximum has become a widespread practice.

This trend is primarily driven by property owners aiming to maximize economic returns, especially in high-value urban areas. Consequently, excessive residential density contributes to the emergence of new population centers, while increased commercial or office density leads to elevated levels of travel demand and attraction. These shifts diverge from the city's intended growth trajectory, reflecting market-driven interests rather than the structured and balanced development approach originally outlined in the planning documents.

Consequently, new urban centers and corridors emerge not as a result of integrated planning but due to market-driven shifts in high-value parcels, often creating spatial imbalance and further complications for long-term transportation planning.

3.3. Street network modifications

Most changes to the street network involve changing the right-of-way of vehicles, relocating streets, or reconfiguring routes. These modifications are typically driven by municipalities' limited financial capacity to acquire land or implement street widening projects. In response, municipalities often request Article 5 commissions to rezone adjacent properties and approve higher building densities. This rezoning creates added value for landowners along the corridor, which in turn facilitates land acquisition for public street expansion through land value compensation (land swaps).

However, such interventions often disregard the original rationale behind street design in urban development plans, where road dimensions, alignments, and functional roles were carefully determined based on adjacent land uses and their position within the broader transportation network. As a result, uncoordinated modifications can undermine the intended performance of the urban circulation system, leading to long-term inefficiencies and reduced network effectiveness.

4. Numerical example

As discussed in the previous section, land-use and density modifications can lead to spatial imbalances and concentrated urban development, especially toward high-value areas, thereby undermining the original goals of urban development plans. This section aims to provide a quantitative illustration of the consequences of such concentrated urban growth through a numerical example.

To this end, the transportation network of Sioux Falls, located in the state of South Dakota, USA, is employed [20]. The network configuration is presented in Fig. 1, along with its associated details, which will be described below.

In this example, two long-term travel demand growth scenarios are considered:

- Uniform growth: demand increases proportionally across all origin-destination (OD) pairs based on existing demand levels.
- Concentrated growth: demand growth is exclusively focused on a small number of destination nodes, specifically, nodes 4 and 5 of the Sioux Falls network (as shown in Fig. 1), representing travel attractors.

These nodes are assumed to have been developed with high-density and high-attraction land uses, reflecting the potential impact of unbalanced urban planning decisions, such as changes in land-use designations and increased density in a few select zones.

For both scenarios, a traffic assignment algorithm is used to model traffic distribution, and the total system travel time is used as the key performance metric. Since total travel time is widely accepted as a comprehensive proxy for several transportation-related costs, as in the network design problems, it is referred to hereafter as the transportation cost [21, 22].

4.1. Comparison of uniform vs. concentrated demand growth scenarios

This experiment examines a gradual increase in travel demand ranging from 0% to 50% above the baseline level. In the uniform growth scenario, demand increases proportionally across all origin-destination (OD) pairs, thereby preserving the spatial balance of the original network. In contrast, the concentrated growth scenario channels all additional demand exclusively toward nodes 4 and 5, simulating the long-term effects of concentrated urban development patterns resulting from suboptimal planning decisions.

To assess the progressive impact of demand growth, travel demand was incrementally increased in 2% steps. Although detailed numerical outputs are not included in this paper, the aggregated results are illustrated in Fig. 2, which depicts the percentage increase in total travel cost under both the uniform and concentrated growth scenarios.

As illustrated in Fig. 2, total travel costs rise in both scenarios as demand increases, which is consistent with expectations. However, the rate of increase is markedly steeper in the concentrated growth scenario, underscoring the inefficiencies associated with spatial imbalance and the accumulation of travel demand in a limited number of urban centers. Notably, when demand exceeds a 30% increase, transportation costs in the concentrated scenario escalate sharply, indicating a significant decline in network performance under such imbalanced conditions[1].

4.2. Mitigating costs of concentrated growth through infrastructure development

An inefficient approach in urban planning involves allowing land-use changes and the resulting growth in travel demand to proceed without adequate regulation, and then attempting to address the ensuing congestion through the construction and expansion of urban roadways. This reactive strategy not only imposes a substantial financial burden during implementation [23], but also promotes increased reliance on private vehicles. As a result, it fails to align with the principles of sustainable urban development.

[1] Increases in total travel time beyond 50% have not been applied or reported, as the severe cost escalation observed under the concentrated growth scenario may induce phenomena such as population migration and changes in trip destinations over the long term factors that warrant cautious interpretation of any further results.

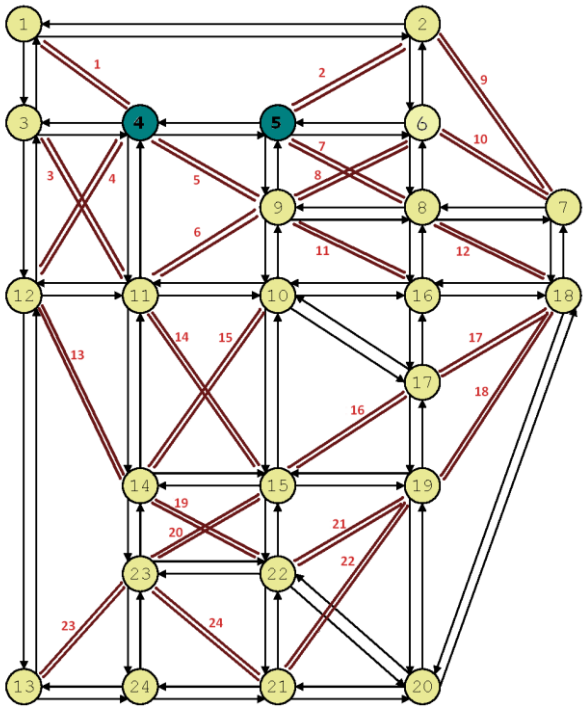

Fig. 1. Sioux Falls transportation network with 24 additional highway links to be constructed.

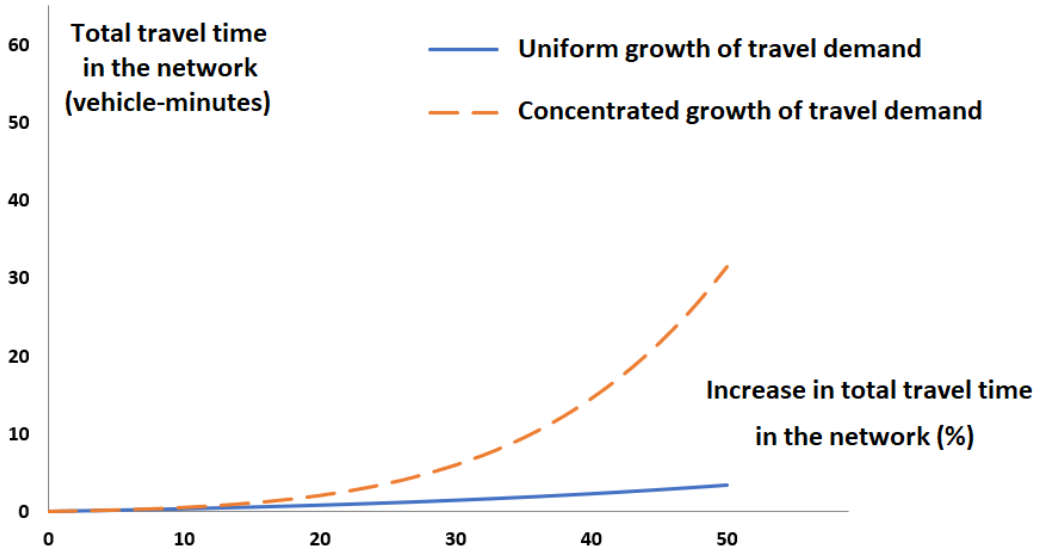

Fig. 2. Increase in total travel cost (travel time) over the network.

This section examines a 100% increase in travel demand under two contrasting scenarios: one involving uniform growth across the network, and the other featuring concentrated growth combined with the implementation of 24 new infrastructure projects, as illustrated in Fig. 1. These projects consist of newly constructed dual-carriageway arterial roads, each designed to accommodate an average practical capacity of 5,000 vehicles per hour per direction. A summary of the comparative results is presented in Table 1.

As observed in Table 1, under the concentrated demand growth scenario in the long term (100% demand increase), even the construction of numerous infrastructure projects with substantial costs fails to effectively mitigate congestion. The incurred costs remain more than three times higher compared to the uniform demand growth scenario.

Table 1. Comparison of the costs of 100% demand growth under two scenarios: uniform growth vs. concentrated growth with new road construction.

	Total travel time in the network (vehicle-minutes)	Increase in total travel time in the network (%)
Uniform growth	122814899	15.4
Concentrated growth accompanied by the construction of 24 new two-way arterial	375875051	49.3

5. Conclusions

This study explored the implications of modifications to urban development plans at the Detailed Plan level. Specifically, it examined three primary categories of change, land-use conversions, increases in building density, and alterations to the road network, alongside a discussion of the associated risks each poses to urban and transportation systems.

To evaluate the transportation impacts of these planning decisions, a numerical case study was conducted using the Sioux Falls transportation network. Two long-term travel demand growth scenarios were analyzed. The first scenario, termed uniform growth, assumed a proportional increase in travel demand across all areas of the network. The second, referred to as concentrated growth, directed the additional demand exclusively toward two designated nodes representing high-attraction zones. These nodes reflect areas that, as a result of misguided planning policies, have been transformed into high-density, high-value land-use zones that generate disproportionate travel demand.

The analysis of demand increases from 0% to 50% revealed that total travel costs in the concentrated growth scenario were significantly higher than in the uniform growth scenario. Furthermore, even under a 100% increase in demand, the concentrated growth scenario—despite incorporating the construction of 24 transportation infrastructure projects, each with an average practical capacity of 5,000 vehicles per hour per direction remained inefficient. In this case, total travel costs exceeded those of the uniform growth scenario by more than threefold.

The findings of this study highlight the critical need to prioritize long-term strategic outcomes over short-term gains when modifying urban development plans, particularly at the Detailed Plan level. Without adequate foresight, such changes can lead to severe transportation inefficiencies and escalating costs, challenges that even large-scale infrastructure investments may fail to resolve. Effective urban planning must therefore strike a careful balance between immediate pressures and sustainable, long-term objectives, especially in terms of how policy decisions affect land use patterns and travel demand growth. While this research employed a simplified model based on the Sioux Falls transportation network in North America, it offers a valuable framework for analyzing the consequences of spatially imbalanced urban growth. Future research should build on this foundation by applying the methodology to real-world case studies in Iran, incorporating long-term behavioral factors such as residential relocation and shifts in trip destinations to enhance the contextual relevance and policy applicability of the results.

Statements & declarations

Author contributions

Fatemeh Mousavi Ghadikolaei: Conceptualization, Formal analysis, Methodology, Investigation.

Mehdi Zarrinmehr: Methodology, Investigation, Writing - Review & Editing.

Reza Mohammad Hasany: Conceptualization, Supervision.

Funding

The authors received no financial support for the research, authorship, and/or publication of this article.

Data availability

The data presented in this study will be available on interested request from the corresponding author.

Declarations

The authors declare no conflict of interes.

References

[1] Acheampong, R. A., Silva, E. A. Land use-transport interaction modeling: A review of the literature and future research directions. Journal of Transport and Land Use, 2015; 8: 11-38. doi:10.5198/jtlu.2015.806.

[2] Raimbault, J. A systematic review and meta-analysis of interaction models between transportation networks and territories. arXiv preprint, 2020; doi:10.48550/arXiv.2012.13367.

[3] Geurs, K. T., van Wee, B. Land-use/transport Interaction Models as Tools for Sustainability Impact Assessment of Transport Investments: Review and Research Perspectives. European Journal of Transport and Infrastructure Research, 2004; 4: doi:10.18757/ejtir.2004.4.3.4272.

[4] Zarrinmehr, A., Saffarzadeh, M., Seyedabrishami, S. A local search algorithm for finding optimal transit routes configuration with elastic demand. International Transactions in Operational Research, 2018; 25: 1491-1514. doi:https://doi.org/10.1111/itor.12359.

[5] Chang, J. S. Models of the Relationship between Transport and Land-use: A Review. Transport Reviews, 2006; 26: 325-350. doi:10.1080/01441640500468432.

[6] Nayeb-Pashaei, K., Vahabzadeh, S., Hosseinian-Far, A., Ghoushchi, S. J. Sustainable Urban Transportation: Key Criteria for a Greener Future. Spectrum of Operational Research, 2025; 3: 103-127. doi:10.31181/sor31202634.

[7] Zarrinmehr, A., Saffarzadeh, M., Seyedabrishami, S., Nie, Y. M. A path-based greedy algorithm for multi-objective transit routes design with elastic demand. Public Transport, 2016; 8: 261-293. doi:10.1007/s12469-016-0131-1.

[8] Habibi, M. From Village to City (Az Shaar ta Shahr). 2nd ed. Tehran (IR): University of Tehran; 1999 (In Persian).

[9] Mirehai, M., Kalantari Khalilabadi, H. Introduction to Urban Development Plans. ed. Tehran (IR): Organization of Municipalities and Village Administrations; 2011 (In Persian).

[10] Ministry of Housing and Urban Development. Regulations on the Procedures for Reviewing and Approving Local, Regional, and National Development and Construction Plans, and Urban Planning and Architecture Rules of the Country, Article 1. Tehran (IR): 1999 (In Persian).

[11] Parliament of Iran. Law on Changing the Name of the Ministry of Development and Housing to the Ministry of Housing and Urban Development. Tehran (IR): 1974 (In Persian).

[12] Iranian Planning and Budget Organization, Strategic Planning Center of the Presidency of Iran. 2011 (In Persian). www.spac.ir.

[13] Parliament of Iran. Law Establishing the High Council of Urban Planning and Architecture of Iran. Tehran (IR): 1974 (In Persian).

[14] Ministry of Housing and Urban Development. Regulations on the Procedures for Reviewing and Approving Local, Regional, and National Development and Construction Plans, and Urban Planning and Architecture Rules of the Country, Article 49. Tehran (IR): 1999 (In Persian).

[15] Pourmohammadi, M. R. Urban Land Use Planning. 1st ed. Tehran (IR): Organization for the Study and Compilation of Humanities Books (SAMT); 2006 (In Persian).

[16] Pakzad, J. The History of Thoughts in Urban Planning. ed. Tehran (IR): Armanshahr Publication; 2010 (In Persian).

[17] Berechman, J., Small, K. A. Modeling Land Use and Transportation: An Interpretive Review for Growh Areas. University of California Transportation Center, 1988; doi:10.1068/a201285.

[18] Chang, J. S., Mackett, R. L. A bi-level model of the relationship between transport and residential location. Transportation Research Part B: Methodological, 2006; 40: 123-146. doi:10.1016/j.trb.2005.02.002.

[19] Siripanich, A., Ghasrikhouzani, M., Rashidi, T. H. Integrating the Garin-Lowry model with a Travel Demand Model. In: Transportation Research Board 98th Annual Meeting; 2019 Jan 13-17; Washington DC, United States. p.

[20] Bar-Gera, H. Transportation Network Test Problems. 2016. https://tzin.bgu.ac.il/~bargera/tntp/.

[21] Sheffi, Y. Urban Transportation Networks: Equilibrium Analysis with Mathematical Programming Methods. 1st ed. Saddle River (NJ): Prentice-Hall; 1984.

[22] Zarrinmehr, A., Shafahi, Y. Parallelization of the Branch-and-Bound Algorithm in Transportation Discrete Network Design. Scientia Iranica, 2016; 23: 407-419. doi:10.24200/sci.2016.2127.

[23] Jiang, F., Ma, L., Broyd, T., Li, J., Jia, J., Luo, H. Systematic framework for sustainable urban road alignment planning. Transportation Research Part D: Transport and Environment, 2023; 120: 103796. doi:10.1016/j.trd.2023.103796.

Civil Engineering and Applied Solutions

Research Article

journal homepage: ceas.journals.umz.ac.ir

CEAS Civil Engineering and Applied Solutions

Optimizing Reservoir Operations with Reinforcement Learning: A Data-Driven Framework

Fariborz Masoumi [a], Mehdi Jorabloo [b*], Gholamreza Shobeyri [c]

[a] *Department of Civil Engineering, University of Mohaghegh Ardabili, Ardabil, Iran*
[b] *Department of Water Engineering, Islamic Azad University, Garmsar, Iran*
[c] *Faculty of Civil, Water & Environmental Engineering, Shahid Beheshti University, Tehran, Iran*

ARTICLE INFO

Keywords:
Reservoir operation
Reinforcement learning
Dez dam
Machine learning

Article history:
Received 28 July 2025
Accepted 20 August 2025
Available online 01 September 2025

ABSTRACT

Effective reservoir management demands adaptive, data-driven strategies to optimize storage and release decisions while balancing multiple, often competing, operational objectives. This study investigates the application of Q-Learning, a model-free reinforcement learning (RL) algorithm, for optimizing reservoir releases under dynamic and uncertain hydrological conditions. Unlike conventional rule-based or offline optimization methods, the proposed RL approach continuously refines its release policy by learning from environmental feedback and observed states, enabling real-time adaptation without the need for a predefined system model. The framework is tested on the Dez Reservoir in Iran, a real-world case study characterized by significant inflow variability and seasonal water demand. Simulation results demonstrate that Q-Learning effectively manages operational complexity, maintaining storage within prescribed bounds and delivering release patterns closely aligned with demand. To benchmark performance, a simplified Ant Colony Optimization (ACO) model is implemented for comparison. While ACO shows moderate capability in deficit reduction, Q-Learning outperforms it in terms of constraint satisfaction and long-term feasibility. Findings highlight the strong potential of reinforcement learning to support intelligent, scalable, and robust decision-making in modern reservoir operation systems under uncertainty.

1. Introduction

1.1. Background and importance of reservoir operation

Water resources management is critical to ensuring a sustainable water supply, hydropower generation, flood mitigation, and ecological conservation. Effective reservoir operation entails complex decision-making to balance competing objectives under uncertain and often dynamic hydrological conditions. Traditional reservoir operation methods, typically based on rule curves or static optimization, frequently lack the flexibility required to respond in real-time to changing environmental and operational scenarios.

1.2. Reinforcement learning and its application to reservoir systems

Reinforcement Learning (RL), a branch of machine learning, enables autonomous agents to learn optimal actions through interactions with their environment, guided by feedback in the form of rewards or penalties. Unlike conventional rule-based or deterministic optimization methods, RL can dynamically refine its decision policies based on observed outcomes, making it well-suited for managing systems with uncertainty and evolving constraints.

* Corresponding author.
E-mail addresses: jorabloo.mehdi@gmail.com (M. Jorabloo).

https://doi.org/10.22080/ceas.2025.29738.1032
ISSN: 3092-7749/
How to cite this article: Masoumi, F., Jorabloo, M., Shobeyri, G. Optimizing Reservoir Operations with Reinforcement Learning: A Data-Driven Framework. Civil Engineering and Applied Solutions. 2025; 1(4): 56–67. doi: 10.22080/ceas.2025.29738.1032.

Among RL techniques, Q-Learning is particularly advantageous for reservoir operations due to its model-free architecture. By building a state-action value function (Q-table), the algorithm learns to adjust reservoir releases based on system observations such as storage levels, inflow rates, and demand forecasts. Its integration into reservoir operations aims to: Improve adaptability in the face of hydrological uncertainty; and enhance operational efficiency while respecting system constraints.

2. Literature review on reservoir operation

Water resource challenges are both complex and complicated, shaped by dynamic interactions among natural processes, socio-economic factors, and diverse stakeholder interests. The complex aspect arises from system uncertainty, feedback loops, and adaptive human and ecological behaviors, while the complicated dimension reflects the involvement of numerous variables, nonlinear relationships, and technical constraints [1]. Reservoir operation optimization, an inherently complicated issue, has evolved significantly over recent decades, mirroring the growing multidimensionality of water resource systems [2, 3].

A wide range of optimization models has been developed to address various water-related problems. These include applications in non-point source pollution control [4-6], decentralized water resources management [7], urban water sustainability [8], sewer network design [9], and reservoir operation under temperature variability [10]. In addition, water reallocation policies have been developed under inflow and demand uncertainty [11], while optimization has also been combined with social behavior models [12], the water-energy-food-greenhouse gas nexus [13], and Water Sensitive Urban Design [14]. These diverse applications highlight the critical role of optimization techniques as powerful tools for navigating trade-offs, improving resource allocation efficiency, and supporting integrated, resilient water management strategies under uncertainty.

A review of over 50 studies reveals a rich landscape of methodologies from traditional optimization techniques to hybrid metaheuristics and intelligent algorithms applied across diverse hydrological, ecological, and operational contexts. Early methods in this domain primarily relied on Traditional Models (TM), such as Linear Programming (LP), Nonlinear Programming (NLP), and Dynamic Programming (DP). These methods provided a rigorous analytical foundation for reservoir optimization but were constrained by computational inefficiencies and limitations in handling stochastic variables and system complexity. For instance, Li et al. [15] and Zhao et al. [16] applied improved DP to multi-reservoir systems, highlighting the method's effectiveness but also its scale limitations. Similarly, Zeng et al. [17] introduced enhancements to DP for parallel reservoir systems to address computational challenges.

The need for flexible and scalable solutions led to a shift toward Evolutionary Algorithms (EA) and Swarm Intelligence (SI) methods, collectively termed EA-SI. Algorithms such as Genetic Algorithms (GA) [18], Particle Swarm Optimization (PSO) [19, 20], and Differential Evolution (DE) [21] have been widely employed. These algorithms allow efficient exploration of nonlinear and non-convex search spaces and are particularly well-suited to multi-objective and multi-reservoir operation problems.

A major development has been the emergence of Metaheuristic Algorithms (MHA), often hybridized with AI or data-driven approaches. For example, Emami et al. [22] introduced a hybrid constrained coral reefs optimization algorithm integrated with machine learning to improve multi-reservoir operational efficiency. Similarly, Moeini and Babaei [23] combined support vector machines (SVM) with a PSO framework for managing reservoir operations under uncertain future conditions.

Among notable metaheuristics, the Imperialist Competitive Algorithm (ICA) stands out. Afshar et al. [4] applied ICA for optimizing piecewise linear operating rule curves in the Dez reservoir, Iran, demonstrating efficient convergence and robustness. The method used a parameterization–simulation–optimization loop and incorporated adaptive penalty functions for constraint handling, making it effective in addressing both water supply and hydropower objectives.

Other innovative algorithms include the Seagull Optimization Algorithm (SOA) used by Ehteram et al. [24], the Jaya Algorithm by Chong et al. [25] and Paliwal et al. [26], and the Charged System Search (CSS) applied by Latif et al. [27]. The Moth-Flame Optimization (MFO) algorithm [28], Sine Cosine Algorithm (SCA) [29], and Hybrid Bat-Swarm Algorithm [30] further enrich the methodological diversity in the field.

Multi-objective optimization approaches are particularly prevalent, addressing trade-offs between hydropower production, water supply, and ecological needs. Liu et al. [31] proposed a bi-objective NSGA-II-based model, while Feng et al. [32] and Meng et al. [33] developed multi-objective frameworks that optimize ecological and economic outcomes simultaneously. Zhang et al. [34]employed a multi-elite guide PSO for multi-reservoir operation, and Raso et al. [35] evaluated operation scenarios to reduce conflicts between hydropower generation and traditional water uses.

Several studies applied optimization to special configurations, such as cascade systems [36, 37], gate-controlled reservoirs [20], or systems integrating hydro-photovoltaic power [38]. Others have considered sedimentation and water-quality dynamics [39, 40], while Allawi et al. [41] explored the use of intelligent models for hydrological parameter forecasting and its influence on operational performance.

Another important advancement is the use of Penalty Functions (PF) in objective formulation. Many reviewed studies incorporate soft constraint enforcement through penalty-based formulations to maintain feasibility under varying hydrological conditions [42, 43].

Furthermore, hybrid and adaptive algorithms are being used to improve convergence and solution stability. For instance, Ahmadianfar et al. [21] applied an adaptive hybrid DE for hydropower scheduling, while Turgut et al. [44] developed a master-slave algorithm for optimizing release policies under real-time constraints.

Despite the methodological diversity and advances, most reviewed studies rely on offline optimization frameworks. This reveals an important research gap: the lack of real-time adaptability in conventional algorithms, which are often unable to adjust to dynamic inflow conditions or user demands without re-optimization.

To bridge this gap, Reinforcement Learning (RL) has recently been identified as a promising paradigm. Unlike traditional methods, RL enables model-free policy learning through continuous interaction with the environment, adapting operational rules dynamically as new data becomes available. Given the high dimensionality, uncertainty, and nonlinearity of reservoir systems, RL offers a viable extension or alternative to existing optimization frameworks.

In summary, the reviewed body of work demonstrates extensive innovation in reservoir operation modeling, spanning deterministic and stochastic frameworks, single and multi-objective formulations, and hybrid intelligent algorithms. As the field progresses, integrating real-time adaptive learning such as RL with the rigor of metaheuristic optimization presents a promising direction for robust, resilient water resource management.

3. Methodology

Reservoir operation constitutes a complex, multi-objective decision-making process that requires adaptive strategies to manage inflow variability, storage dynamics, and release policies. Conventional optimization approaches such as linear programming (LP), nonlinear programming (NLP), and dynamic programming (DP) have been widely employed. However, these methods typically rely on fixed mathematical models, limiting their adaptability under uncertain and evolving hydrological conditions.

Reinforcement Learning (RL) provides a data-driven framework for reservoir operation by enabling an agent to learn optimal decisions through repeated interactions with its environment. This adaptive trial-and-error mechanism allows policies to evolve in response to changing conditions. In this study, Q-Learning, a model-free RL algorithm, is used to dynamically optimize reservoir release policies, eliminating the need for predefined operating rules or model assumptions.

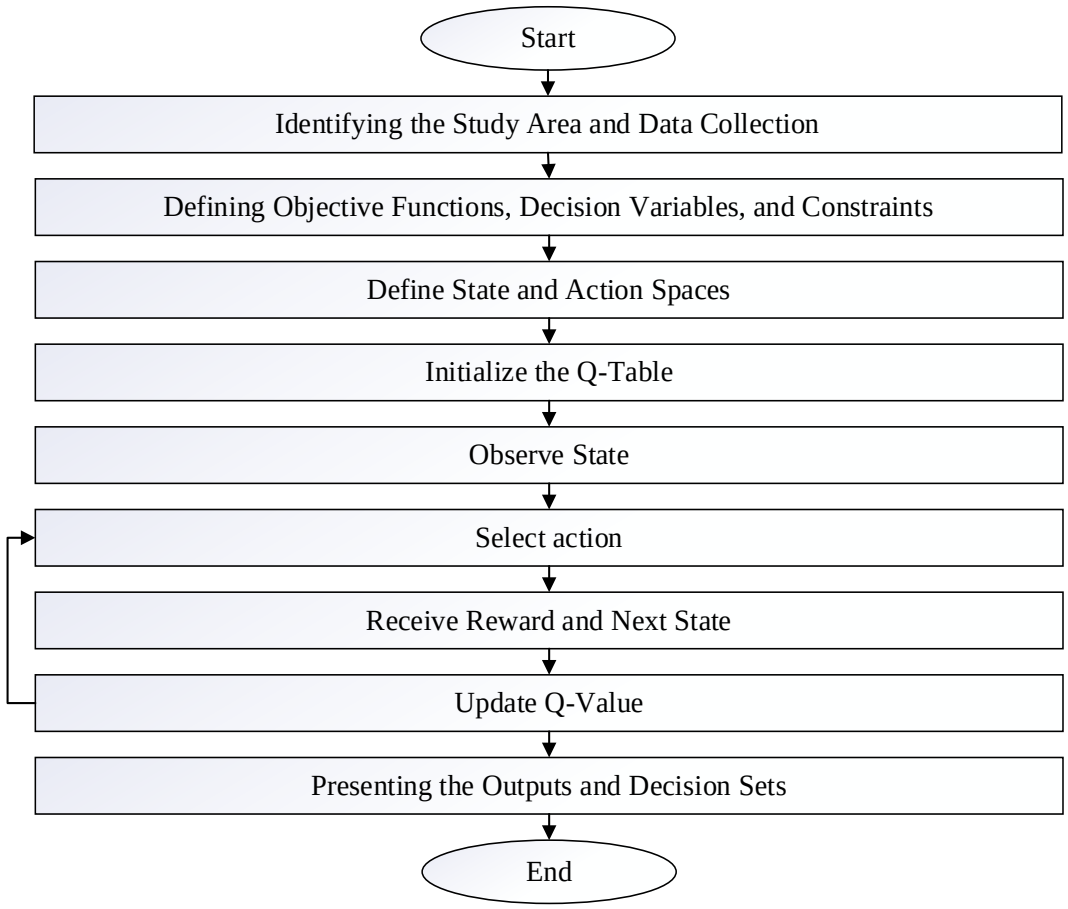

Fig. 1. The flowchart of the proposed methodology of RL application in reservoir operation.

In reinforcement learning, the system's state space represents the current storage level of the reservoir. In this study, the reservoir storage levels range from minimum (s_{min}) to maximum (s_{max}), with discrete intervals representing different states. The action space corresponds to the release decisions, constrained within a predefined range (r_{min} to r_{max}) to maintain operational limits.

State transitions are governed by the interplay between inflow variability, storage updates, and water demand at each time step. This dynamic formulation enables the RL agent to adaptively determine release decisions based on current conditions, allowing it to respond to fluctuations in system states and external inputs. The conceptual framework of the reinforcement learning approach is illustrated in Fig. 2, which summarizes the learning cycle, including environment observation, action execution, reward evaluation, and policy updates.

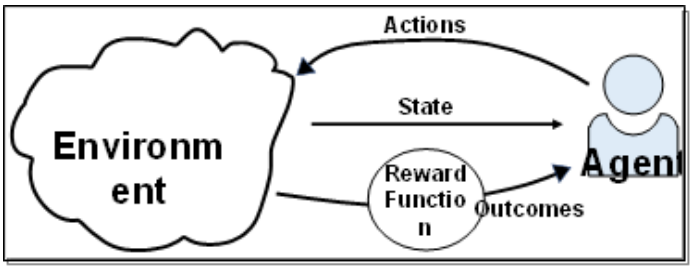

Fig. 2. The main concept of the RL [45].

Recent advancements in artificial intelligence (AI) and machine learning (ML) have introduced data-driven and adaptive strategies for reservoir management. Among these, reinforcement learning (RL) has gained significant attention due to its ability to learn optimal policies through trial-and-error interactions with the environment. In this study, we focus on Q-Learning, a model-free RL algorithm, to optimize reservoir release decisions while enhancing system efficiency and sustainability. Q-Learning is a value-based reinforcement learning method where an agent learns the optimal policy by estimating the expected cumulative reward of state-action pairs. The Q-Learning framework follows these core steps:

1. Initialization:
   - The agent begins with an initial reservoir storage value ($s_{initial}$).
   - A Q-table, representing the expected reward of each state-action pair, is initialized with zeros.
   - Historical or synthetic inflow data and demand sequences are predefined for training and evaluation purposes.
2. Action selection:
   - The agent selects reservoir release actions using an epsilon-greedy strategy, which balances exploration (randomized action selection) and exploitation (choosing the highest $Q - value$ action).
   - Initially, exploration dominates to allow the model to learn efficiently, but as training progresses, exploitation becomes more prominent to refine decision-making.
3. Reward function design:
   - The reward function incentivizes meeting demand while discouraging deviations and violations of system constraints. Neutral or positive rewards are assigned when releases closely match demand. Penalties are imposed when releases exceed or fall short of demand, or when storage or release constraints are violated.
4. Q-Value update (bellman equation):
   - The $Q - values$ are updated iteratively using the Bellman equation, which considers:
   - Immediate reward based on the release decision.
   - Future reward expectations, incorporating a discount factor (γ) to prioritize long-term outcomes.
   - Learning rate (α) to control the magnitude of updates.

   The Q-value update formula is given by:

$$Q_{new}(s_t, a_t) \leftarrow (1-\alpha) \times Q_{old}(s_t, a_t) + \alpha \times (r_t + \gamma \times max\, Q(s_{t+1}, a')) \quad (1)$$

where, t stands for the time step, $Q_{old}(s_t, a_t)$ is the Q-factor in the previous episode for action a_t and state s_t; $Q_{new}(s_t, a_t)$ is the Q-factor in the new episode for action a_t and state s_t; s_t is the state of the system (here, the reservoir condition) in the time step t, and a_t is the action in the time step t; s_{t+1} is the next state is determined based on the selected action a_t; the symbol α represents the learning rate, and it is between 0 and 1; it reflects how significantly the reward signal or r_t influences the update of the value function or Q; γ is the discount rate, it is between 0 and 1, it represents how a decision influences future possibilities and how the value function guides that decision-making process; $max\, Q(s_{t+1}, a')$ is the maximum Q-factor in the s_{t+1} mode for all possible actions, r_t is the value of the instantaneous reward received by the agent for the operation of a_t in s_t mode.

3.1. Mathematical formulation (single-reservoir, monthly time step)

In this section, the main formulation for the reservoir simulation model is presented. The main formulation is presented below.

$$S_{t+1} = S_t + I_t - R_t \quad (2)$$

where, S_{t+1}: Storage volume at the beginning of the month $t+1$. S_t: Storage volume at the beginning of the month t. I_t: Inflow volume into the reservoir during the month t. I_t: Inflow volume into the reservoir during the month t; R_t: Release volume from the reservoir during the month t.

3.2. Exploration vs exploitation mechanism

To promote learning, the model begins with a high probability of exploration, randomly selecting actions in early episodes. As learning progresses, this probability decreases, allowing the agent to increasingly exploit its learned policy. Periodic reintroduction of random actions helps avoid local optima and ensures broader policy robustness.

3.3. Training and convergence criteria

The model is trained over a fixed number of episodes (e.g., 500,000), each simulating reservoir operation across the defined time horizon. Training is considered converged when:

- $Q - values$ stabilize, indicating convergence towards an optimal policy.
- Exploration probability is sufficiently reduced, favoring exploitation.
- Reservoir release performance meets predefined operational benchmarks.

3.4. Implementation details

The RL algorithm is implemented in MATLAB, utilizing:

- Storage state discretization, defining reservoir states at incremental levels within operational bounds.
- Q-table structure, storing state-action values for iterative updates.
- Demand incorporation, ensuring releases are adjusted to meet water requirements dynamically.
- Performance tracking, analyzing learning progress and policy improvements through reward evolution.

3.5. Significance and practical implications

This RL-based approach offers multiple advantages over traditional reservoir operation methods: Dynamic Adaptation: The Q-Learning framework continuously adjusts decisions, improving release efficiency across varying hydrological conditions. Optimization Without Explicit Models: Unlike traditional optimization techniques, Q-Learning does not require explicit mathematical models, making it highly adaptable to data-driven environments. Efficient Water Resource Allocation: By refining release decisions, the methodology enhances water supply reliability, hydropower production efficiency, and environmental sustainability.

4. Case study

The Dez Reservoir, situated in southwestern Iran, is a critical infrastructure element for regional water supply, supporting agricultural irrigation, domestic consumption, and industrial use. Constructed on the Dez River, the reservoir plays a pivotal role in sustaining water availability across Khuzestan Province, where seasonal and climatic variability significantly influence demand. This case study examines the reservoir's hydrological features, operational parameters, and its strategic role in ensuring long-term water security for multiple sectors.

- Geographical and hydrological overview

Located in a semi-arid region, the Dez Reservoir receives its inflows predominantly from rainfall and snowmelt originating in the Zagros Mountains. With a total storage capacity exceeding 3 billion cubic meters, it ranks among the largest reservoirs in Iran. Inflow patterns exhibit substantial seasonal and interannual variability, shaped by precipitation and upstream hydrological dynamics. Effective management of these fluctuations is vital to avoid shortages and maintain a continuous supply for both agricultural and urban demands.

To regulate storage and distribution, the reservoir operates under a structured management framework, adjusting release rates based on agricultural demands and municipal consumption trends. Water allocation models are integrated into reservoir operations to ensure equitable distribution, particularly during dry periods when inflow rates decline.

- Water supply management and distribution

As a cornerstone of Iran’s water infrastructure, the Dez Reservoir supports extensive irrigation systems that serve large-scale agricultural operations. These networks rely on seasonal demand forecasts to guide water allocation, helping sustain crop yields while minimizing reservoir drawdown. In parallel, the reservoir provides essential potable water to urban and industrial sectors through municipal distribution systems. Downstream water treatment facilities ensure the supply of safe drinking water by incorporating filtration and purification processes. During drought events, reservoir managers employ adaptive release strategies to prioritize essential needs and conserve storage volumes.

Municipal water supply remains a key operational priority. The reservoir supports urban water distribution networks, delivering potable water to communities and industries. Water treatment facilities downstream process and distribute clean drinking water, integrating filtration and purification technologies to maintain quality standards.

During drought conditions, reservoir managers implement adaptive strategies, adjusting release patterns to conserve storage

while ensuring essential water needs are met.

For simulation purposes, the reservoir is characterized by a maximum storage capacity of 3,340 million cubic meters (MCM) and a minimum operational threshold of 830 MCM. The initial storage is set to 1,430 MCM, reflecting a mid-range condition. The model enforces a maximum monthly release limit of 1,000 MCM, with the flexibility to withhold releases entirely during low-flow conditions. Historical inflow data reveal considerable variability:

- 5-year average inflow: 5,303 MCM
- 20-year average: 5,990 MCM
- 40-year average: 5,951 MCM

This variability underscores the need for robust and flexible operational policies that can accommodate both short-term fluctuations and long-term hydrological trends.

5. Results and discussion

This section presents a comparative evaluation of simple Ant Colony Optimization (ACO) and Q-Learning algorithms applied to a single-reservoir operation problem over a 60-month planning horizon. Both models were implemented in MATLAB under consistent hydrological inputs, operational constraints, and demand profiles to ensure fairness and reproducibility. The objective was to minimize the total demand deficit while satisfying system constraints related to storage bounds and release capacities. Key performance indicators included cumulative fitness score, total unmet demand, number of constraint violations, and monthly operational trends. Graphical representations of release decisions, storage dynamics, and deficits offer qualitative insights into each algorithm's operational behavior and effectiveness.

5.1. Performance metrics comparison

The comparative analysis relies on system-wide performance indicators derived from each algorithm's output. Table 1 summarizes the key metrics, including fitness score, demand deficit, and constraint violations.

Table 1. Summary of performance metrics.

Metric	ACO	Q-Learning	Unit
Total fitness	752,879.33	4,322.03	Unitless (composite penalty score)
Total demand deficit	1,003.50	4,322.03	Million Cubic Meters (MCM)
Storage violations	32	0	Count
Release violations	0	0	Count

The total fitness score, which combines penalties from demand deficits and constraint violations, reveals a substantial performance gap between the two methods. Q-Learning achieved a significantly lower fitness score (4,322.03) compared to ACO (752,879.33), indicating a more feasible and operationally robust reservoir strategy. The low score for Q-Learning reflects its ability to maintain system constraints while balancing competing objectives.

Interestingly, the total demand deficit was higher under Q-Learning (4,322.03 MCM) than ACO (1,003.50 MCM). At first glance, this might suggest superior demand satisfaction by ACO. However, this interpretation overlooks the broader context: ACO violated the reservoir's storage constraints 32 times during the simulation, each breach contributing heavily to its overall penalty and inflated fitness score. These violations indicate instability in reservoir behavior, compromising the practical feasibility of the solution.

In contrast, Q-Learning maintained zero violations across all episodes, consistently operating within both storage and release limits. Although this came at the cost of some unmet demand, the agent prioritized long-term sustainability and operational reliability as core goals in real-world reservoir management.

Furthermore, both algorithms successfully avoided release violations, demonstrating that release bounds were effectively enforced. This reinforces the notion that the key differentiator between the two lies in how they handle storage dynamics and long-term feasibility, not just raw demand satisfaction.

5.2. Monthly release and storage trends

To evaluate the operational performance of both algorithms over time, monthly data on reservoir releases, storage levels, and unmet demand were analyzed across the 60-month simulation period. The results reveal clear distinctions in the temporal decision-making behaviors of Q-Learning and Ant Colony Optimization (ACO).

Fig. 3 provides a detailed visualization of the operational dynamics generated by the Ant Colony Optimization (ACO) algorithm over the 60-month simulation period. The top panel displays monthly release volumes alongside corresponding demand levels, illustrating that while ACO generally responds to fluctuations in demand, its release decisions are occasionally misaligned due to heuristic-driven exploration or constraint trade-offs.

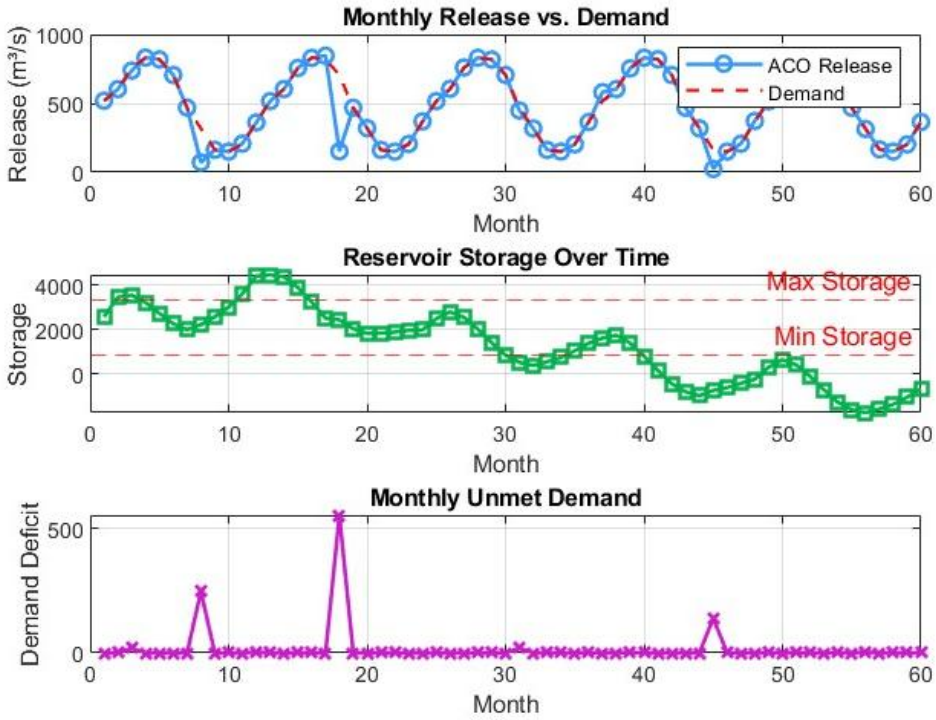

Fig. 3. ACO-based reservoir simulation: monthly dynamics of release, storage, and demand deficit over a five-year horizon.

The middle panel depicts reservoir storage levels, showing considerable variability with multiple exceedances of both the minimum and maximum storage thresholds, clear evidence of constraint violations. The bottom panel presents monthly unmet demand, characterized by intermittent spikes that highlight the system's difficulty in consistently satisfying water needs without breaching operational limits. Collectively, these plots reflect ACO's adaptive but volatile decision-making, which manages to meet demand in many months but often at the expense of violating storage constraints and compromising long-term system feasibility.

In the case of ACO, release decisions exhibited considerable volatility, characterized by frequent oscillations between over-releasing and overly conservative adjustments. This erratic behavior resulted in multiple instances of both storage overshoot and undershoot, ultimately leading to 32 documented violations of the reservoir's operational limits. Although such actions occasionally succeeded in minimizing short-term demand deficits, they undermined the overall stability of the reservoir system and incurred significant penalty costs due to constraint breaches.

In contrast, Q-Learning produced more stable and coherent release patterns. Leveraging an epsilon-greedy strategy and extensive training across 500,000 episodes, the agent progressively refined its policy to account for variations in inflow and evolving storage conditions. As a result, reservoir storage levels remained consistently within the defined operational bounds throughout the simulation period, demonstrating the model's capacity to manage hydrological risk effectively and comply with system constraints.

Fig. 4 highlights the effective performance of the Q-Learning algorithm in managing reservoir operations across a 60-month simulation period. In the top panel, the release trajectory produced by Q-Learning closely aligns with monthly water demand, demonstrating the model's capacity to learn and implement balanced release strategies. This responsiveness stems from the algorithm's reinforcement-based learning structure, which enables the agent to refine its decisions through continuous interaction with the environment.

The middle panel shows that reservoir storage levels remained consistently within operational limits throughout the simulation. This adherence to constraints reflects the model's ability to internalize system rules through repeated training and to maintain feasibility even under fluctuating inflow and demand conditions. The absence of storage violations throughout the entire time horizon is a key indicator of the model's reliability in real-world operational contexts.

In the bottom panel, monthly unmet demand levels remain moderate and well-distributed, suggesting that the model occasionally allowed small deficits in favor of preserving long-term operational stability. This behavior illustrates the agent's capacity to manage trade-offs intelligently, avoiding short-term overreactions and instead favoring sustained performance across the entire planning period.

It is important to note that the version of Ant Colony Optimization used in this study represents one of its simplest forms, implemented here primarily for baseline comparison. The strong performance of Q-Learning, especially in terms of constraint compliance and adaptive release behavior, underscores its potential as a robust and scalable approach for data-driven reservoir operation. Its ability to maintain operational stability while responding flexibly to environmental variability makes it a promising tool for future water resources management applications.

Fig. 5 presents a side-by-side comparison of reservoir operations generated by Q-Learning and a simplified implementation of Ant Colony Optimization (ACO) across three key dimensions: release behavior, storage dynamics, and demand deficit over the 60-month planning horizon. The release pattern produced by Q-Learning shows consistent alignment with monthly demand, highlighting the model's capacity to learn adaptive and balanced strategies that evolve in response to inflow and system state changes.

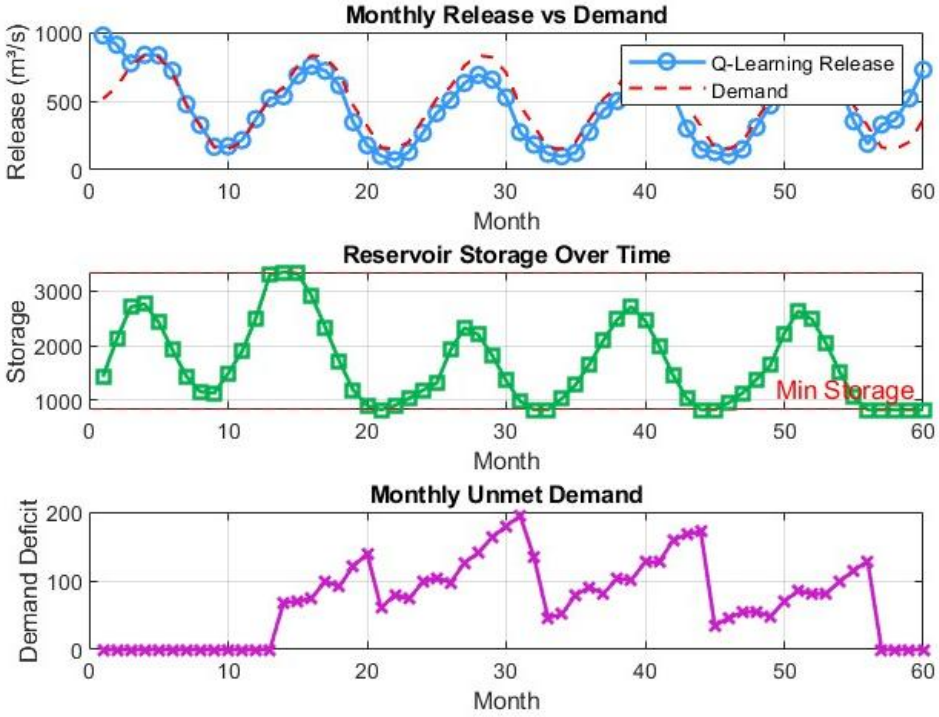

Fig. 4. Q-Learning-based reservoir operation: performance insights from release, storage, and deficit dynamics.

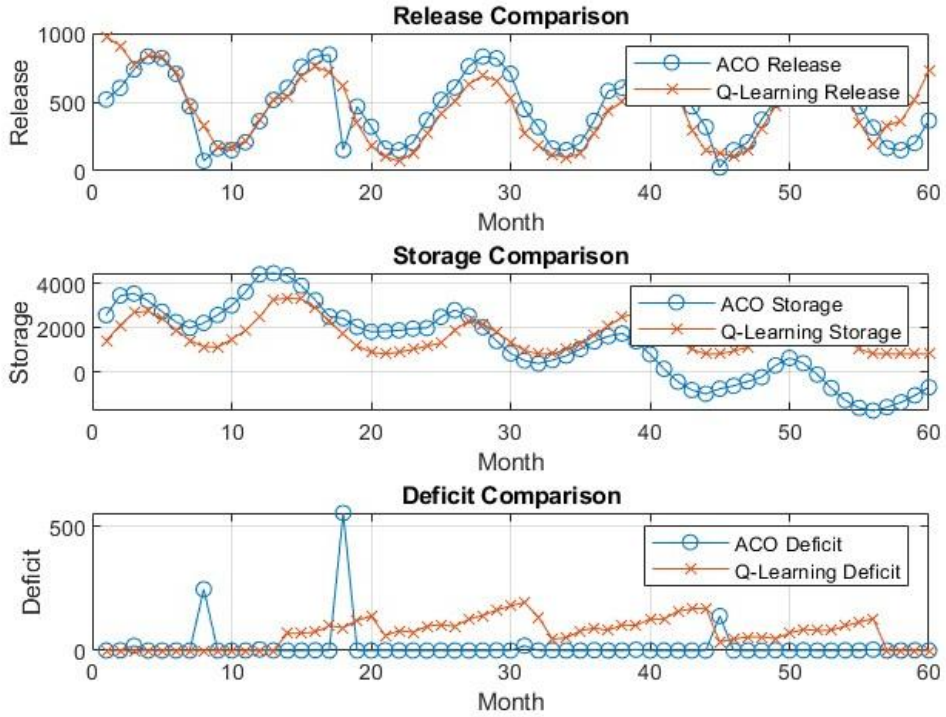

Fig. 5. Side-by-side algorithmic comparison of reservoir operations: ACO vs Q-Learning.

In terms of storage management, Q-Learning maintains reservoir levels well within operational boundaries throughout the simulation period. This reflects the algorithm's effective internalization of system constraints and its ability to avoid violations even under variable conditions. The storage profile demonstrates stability and discipline, indicating the agent's focus on long-term operational feasibility.

The deficit panel further illustrates Q-Learning's strategic behavior. While small deficits occur in certain months, they are

distributed evenly and remain within acceptable limits. This suggests the model occasionally allows controlled shortfalls to preserve broader system integrity over time, a hallmark of sustainable reservoir operation.

It should be noted that the ACO implementation used here serves as a basic benchmark to contrast learning-based decision-making with heuristic search methods. Despite its simplicity, the comparison helps to underscore the key advantage of Q-Learning: its ability to dynamically improve performance through experience, adapt to environmental variability, and maintain consistent compliance with operational rules. Overall, Fig. 5 reinforces Q-Learning's promise as a reliable, adaptive approach for managing reservoir systems under uncertainty.

5.3. Constraint handling and penalty impacts

Effective constraint management is a critical aspect of realistic reservoir operation modeling. In this study, both algorithms incorporated mechanisms to address storage and release constraints, but their strategies and outcomes varied significantly.

Q-Learning handled operational constraints through a built-in reward function that inherently discouraged violations. Over the course of training, the agent learned via repeated interactions and feedback to avoid actions that would lead to infeasible storage or release values. This internalization of system rules resulted in zero storage or release violations during the entire simulation, indicating the algorithm's strength in achieving not only high performance but also operational reliability.

The Ant Colony Optimization approach used here employed a basic penalty structure, where violations of constraints were accounted for by adding penalty terms to the fitness score. While this approach provided a mechanism to discourage infeasible actions, the version of ACO implemented in this study was intentionally kept simple for baseline comparison. As such, the algorithm occasionally prioritized short-term improvements in demand satisfaction at the expense of constraint adherence, leading to elevated fitness penalties due to storage violations.

This contrast highlights one of the key advantages of Q-Learning: its ability to evolve policies that balance immediate objectives with long-term feasibility. Rather than relying solely on external penalties, Q-Learning gradually developed an operational strategy that inherently respected system constraints while maintaining stable and adaptive behavior across varying hydrological conditions.

5.4. Computational efficiency and scalability

In addition to performance and feasibility, computational efficiency and scalability are important considerations in selecting an appropriate reservoir operation algorithm, particularly for real-time or large-scale applications.

The Q-Learning model, though trained over a large number of episodes (500,000 in this study), benefited from a lightweight and structured learning architecture. Its use of matrix-based Q-table representations allowed for efficient updates and rapid convergence tracking. Once training was completed, the learned policy could be executed instantaneously for decision-making, well-suited for real-time operational deployment. Moreover, the model's independence from explicit hydrological equations enhances its adaptability to different system configurations, suggesting strong potential for scalability to more complex, multi-reservoir systems or longer planning horizons.

The Ant Colony Optimization (ACO) approach, implemented here in a basic form for benchmarking purposes, followed a heuristic search process that involved multiple agents (ants) exploring the solution space. This method required repeated pheromone updates and solution evaluations across iterations, which increased computational overhead, particularly as the number of decision variables (e.g., months or release levels) expanded. While more advanced variants of ACO can reduce this burden through parallelization and parameter tuning, the simplified version applied in this study was not optimized for efficiency or scale.

Overall, Q-Learning demonstrated greater potential for practical application in terms of computational performance and scalability. Its structured learning process, adaptability, and low execution cost once trained position it as a promising tool for modern, data-driven water resources management systems.

5.5. Final verdict and implications

The comparative results of this study highlight the strong potential of Q-Learning as a reliable and adaptive tool for reservoir operation. Across all evaluated dimensions, constraint satisfaction, operational stability, computational efficiency, and scalability, Q-Learning consistently delivered feasible and well-balanced release strategies. Its ability to learn from interaction with the environment and evolve robust policies over time makes it especially well-suited for dynamic and uncertain hydrological systems.

The Q-Learning model achieved complete compliance with operational constraints, maintained storage levels within prescribed bounds, and produced release patterns closely aligned with demand. Although moderate unmet demand was observed in some months, these shortfalls were strategically distributed and acceptable within the context of maintaining long-term system stability. Once trained, the algorithm was computationally efficient and highly responsive, demonstrating potential for real-time deployment and scalability to more complex systems, such as multi-reservoir networks.

The Ant Colony Optimization (ACO) algorithm used in this study was implemented in its simplest form to serve as a heuristic-based baseline for comparison. While it showed some ability to reduce short-term demand deficits, it lacked the adaptive learning capabilities needed to consistently balance performance with feasibility. More advanced versions of ACO may perform better under different configurations; however, the results here emphasize the added value of incorporating reinforcement learning into water

resources planning frameworks.

In conclusion, this study reinforces the role of reinforcement learning, particularly Q-Learning, as a promising paradigm for intelligent reservoir management. Its model-free nature, adaptive behavior, and real-time decision-making capability position it as a valuable alternative or complement to traditional and metaheuristic optimization techniques. As climate variability and increasing demand continue to challenge water systems, data-driven and self-improving models like Q-Learning are likely to play a central role in the next generation of sustainable water resources management.

6. Conclusions

This study demonstrated the effectiveness of reinforcement learning, specifically Q-Learning, for optimizing reservoir operations under uncertain and dynamic hydrological conditions. By learning optimal release strategies through iterative interactions with the system, the Q-Learning agent was able to maintain storage and release decisions within prescribed constraints while achieving a high level of adaptability to variable inflows and demand scenarios. Compared to a simplified implementation of Ant Colony Optimization (ACO), the Q-Learning model exhibited superior performance in operational feasibility, stability, and scalability. Although ACO occasionally yielded lower demand deficits, it did so at the cost of constraint violations and operational instability. These results underscore the potential of model-free reinforcement learning approaches in supporting intelligent, data-driven water resources management. Future research may extend this framework to multi-reservoir systems, integrate climate uncertainty, and hybridize RL models with physical simulation tools to enhance realism and generalizability.

Statements & Declarations

Author contributions

Fariborz Masoumi: Conceptualization, Methodology, Formal analysis, Resources, Original Draft, Writing.

Mehdi Jorabloo: Conceptualization, Methodology, Formal analysis, Resources, Original Draft, Writing.

Gholamreza Shobeyri: Conceptualization, Methodology, Formal analysis, Resources, Original Draft, Writing.

Funding

The authors declare that no funds, grants, or other support were received during the preparation of this manuscript.

Declarations

The authors declare no conflict of interes.

References

[1] Emami-Skardi, M. J., Shobeyri, G., Kerachian, R. Analysis of Stakeholder Relationships and Conflicts Using the Conflict Tree Approach. Iran-Water Resources Research, 2023; 18: 57–74. doi:20.1001.1.17352347.1401.18.4.4.8.

[2] Afshar, A., Emami Skardi, M. J., Jerani, F. Pond designing optimization using Multi-Objective ant colony algorithm and swat model. Journal of Environmental Science and Technology, 2015; 16 (Special issue): 121–132.

[3] Masoumi, F., Masoumzadeh, S., Zafari, N., Emami-Skardi, M. J. Optimal operation of single and multi-reservoir systems via hybrid shuffled grey wolf optimization algorithm (SGWO). Water Supply, 2021; 22: 1663–1675. doi:10.2166/ws.2021.326.

[4] Afshar, A., Emami Skardi, M. J., Masoumi, F. Optimizing water supply and hydropower reservoir operation rule curves: An imperialist competitive algorithm approach. Engineering Optimization, 2015; 47: 1208–1225. doi:10.1080/0305215X.2014.958732.

[5] Emami Skardi, M. J., Afshar, A., Saadatpour, M., Sandoval Solis, S. Hybrid ACO–ANN-Based Multi-objective Simulation–Optimization Model for Pollutant Load Control at Basin Scale. Environmental Modeling & Assessment, 2015; 20: 29–39. doi:10.1007/s10666-014-9413-7.

[6] Skardi, M. J. E., Afshar, A., Solis, S. S. Simulation-optimization model for non-point source pollution management in watersheds: Application of cooperative game theory. KSCE Journal of Civil Engineering, 2013; 17: 1232–1240. doi:10.1007/s12205-013-0077-7.

[7] Moradikian, S., Emami-Skardi, M. J., Kerachian, R. A distributed constraint multi-agent model for water and reclaimed wastewater allocation in urban areas: Application of a modified ADOPT algorithm. Journal of Environmental Management, 2022; 317: 115446. doi:10.1016/j.jenvman.2022.115446.

[8] Emamjomehzadeh, O., Kerachian, R., Emami-Skardi, M. J., Momeni, M. Combining urban metabolism and reinforcement learning concepts for sustainable water resources management: A nexus approach. Journal of Environmental Management, 2023; 329: 117046. doi:10.1016/j.jenvman.2022.117046.

[9] Masoumi, F., Masoumzadeh, S., Zafari, N., Javad Emami-Skardi, M. Optimum sanitary sewer network design using shuffled gray wolf optimizer. Journal of Pipeline Systems Engineering and Practice, 2021; 12: 04021055. doi:10.1061/(ASCE(PS.1949-1204.0000597.

[10] Tabari, M. M. R., Azadani, M. N., Kamgar, R. Development of operation multi-objective model of dam reservoir under conditions of temperature variation and loading using NSGA-II and DANN models: a case study of Karaj/Amir Kabir dam. Soft Computing, 2020; 24: 12469–12499. doi:10.1007/s00500-020-04686-1.

[11] Tabari, M. M. R., Safari, R. Development of water re-allocation policy under uncertainty conditions in the inflow to reservoir and demands parameters: a case study of Karaj AmirKabir dam. Soft Computing, 2023; 27: 6521–6547. doi:10.1007/s00500-023-07885-8.

[12] Eyni, A., Skardi, M. J. E., Kerachian, R. A regret-based behavioral model for shared water resources management: Application of the correlated equilibrium concept. Science of The Total Environment, 2021; 759: 143892. doi:10.1016/j.scitotenv.2020.143892.

[13] Emamjomehzadeh, O., Omidi, F., Kerachian, R., Emami-Skardi, M. J., Momeni, M. Water-energy-food-greenhouse gases nexus management in urban environments: A robust multi-agent decision-support system. Sustainable Cities and Society, 2024; 113: 105676. doi:10.1016/j.scs.2024.105676.

[14] Sharifian, H., Emami-Skardi, M. J., Behzadfar, M., Faizi, M. Water sensitive urban design (WSUD) approach for mitigating groundwater depletion in urban geography; through the lens of stakeholder and social network analysis. Water Supply, 2022; 22: 5833–5852. doi:10.2166/ws.2022.206.

[15] Li, C., Zhou, J., Ouyang, S., Ding, X., Chen, L. Improved decomposition–coordination and discrete differential dynamic programming for optimization of large-scale hydropower system. Energy Conversion and Management, 2014; 84: 363–373. doi:10.1016/j.enconman.2014.04.065.

[16] Zhao, T., Cai, X., Lei, X., Wang, H. Improved dynamic programming for reservoir operation optimization with a concave objective function. Journal of Water Resources Planning and Management, 2012; 138: 590–596. doi:10.1061/(ASCE)WR.1943-5452.0000205.

[17] Zeng, X., Hu, T., Cai, X., Zhou, Y., Wang, X. Improved dynamic programming for parallel reservoir system operation optimization. Advances in Water Resources, 2019; 131: 103373. doi:10.1016/j.advwatres.2019.07.003.

[18] Tegegne, G., Kim, Y.-O. Representing inflow uncertainty for the development of monthly reservoir operations using genetic algorithms. Journal of Hydrology, 2020; 586: 124876. doi:10.1016/j.jhydrol.2020.124876.

[19] Al-Aqeeli, Y. H., Mahmood Agha, O. M. A. Optimal Operation of Multi-reservoir System for Hydropower Production Using Particle Swarm Optimization Algorithm. Water Resources Management, 2020; 34: 3099–3112. doi:10.1007/s11269-020-02583-8.

[20] Kim, Y.-G., Sun, B.-Q., Kim, P., Jo, M.-B., Ri, T.-H., Pak, G.-H. A study on optimal operation of gate-controlled reservoir system for flood control based on PSO algorithm combined with rearrangement method of partial solution groups. Journal of Hydrology, 2021; 593: 125783. doi:10.1016/j.jhydrol.2020.125783.

[21] Ahmadianfar, I., Kheyrandish, A., Jamei, M., Gharabaghi, B. Optimizing operating rules for multi-reservoir hydropower generation systems: An adaptive hybrid differential evolution algorithm. Renewable Energy, 2021; 167: 774–790. doi:10.1016/j.renene.2020.11.152.

[22] Emami, M., Nazif, S., Mousavi, S.-F., Karami, H., Daccache, A. A hybrid constrained coral reefs optimization algorithm with machine learning for optimizing multi-reservoir systems operation. Journal of Environmental Management, 2021; 286: 112250. doi:10.1016/j.jenvman.2021.112250.

[23] Moeini, R., Babaei, M. Hybrid SVM-CIPSO methods for optimal operation of reservoir considering unknown future condition. Applied Soft Computing, 2020; 95: 106572. doi:10.1016/j.asoc.2020.106572.

[24] Ehteram, M., Banadkooki, F. B., Fai, C. M., Moslemzadeh, M., Sapitang, M., Ahmed, A. N., Irwan, D., El-Shafie, A. Optimal operation of multi-reservoir systems for increasing power generation using a seagull optimization algorithm and heading policy. Energy Reports, 2021; 7: 3703–3725. doi:10.1016/j.egyr.2021.06.008.

[25] Chong, K. L., Lai, S. H., Ahmed, A. N., Wan Jaafar, W. Z., El-Shafie, A. Optimization of hydropower reservoir operation based on hedging policy using Jaya algorithm. Applied Soft Computing, 2021; 106: 107325. doi:10.1016/j.asoc.2021.107325.

[26] Paliwal, V., Ghare, A. D., Mirajkar, A. B., Bokde, N. D., Feijoo Lorenzo, A. E. Computer modeling for the operation optimization of mula reservoir, Upper Godavari Basin, India, Using the Jaya Algorithm. Sustainability, 2019; 12: 84. doi:10.3390/su12010084.

[27] Latif, S. D., Marhain, S., Hossain, M. S., Ahmed, A. N., Sherif, M., Sefelnasr, A., El-Shafie, A. Optimizing the operation release policy using charged system search algorithm: a case study of Klang Gates Dam, Malaysia. Sustainability, 2021; 13: 5900. doi:10.3390/su13115900.

[28] Zhang, Z., Qin, H., Yao, L., Liu, Y., Jiang, Z., Feng, Z., Ouyang, S. Improved Multi-objective Moth-flame Optimization Algorithm based on R-domination for cascade reservoirs operation. Journal of Hydrology, 2020; 581: 124431. doi:10.1016/j.jhydrol.2019.124431.

[29] Feng, Z.-k., Liu, S., Niu, W.-j., Li, B.-j., Wang, W.-c., Luo, B., Miao, S.-m. A modified sine cosine algorithm for accurate global optimization of numerical functions and multiple hydropower reservoirs operation. Knowledge-Based Systems, 2020; 208: 106461. doi:10.1016/j.knosys.2020.106461.

[30] Yaseen, Z. M., Allawi, M. F., Karami, H., Ehteram, M., Farzin, S., Ahmed, A. N., Koting, S. B., Mohd, N. S., Jaafar, W. Z. B., Afan, H. A., El-Shafie, A. A hybrid bat–swarm algorithm for optimizing dam and reservoir operation. Neural Computing and Applications, 2019; 31: 8807–8821. doi:10.1007/s00521-018-3952-9.

[31] Liu, D., Huang, Q., Yang, Y., Liu, D., Wei, X. Bi-objective algorithm based on NSGA-II framework to optimize reservoirs operation. Journal of Hydrology, 2020; 585: 124830. doi:10.1016/j.jhydrol.2020.124830.

[32] Feng, Z.-k., Niu, W.-j., Zhang, R., Wang, S., Cheng, C.-t. Operation rule derivation of hydropower reservoir by k-means clustering method and extreme learning machine based on particle swarm optimization. Journal of Hydrology, 2019; 576: 229–238. doi:10.1016/j.jhydrol.2019.06.045.

[33] Meng, X., Chang, J., Wang, X., Wang, Y. Multi-objective hydropower station operation using an improved cuckoo search algorithm. Energy, 2019; 168: 425–439. doi:10.1016/j.energy.2018.11.096.

[34] Zhang, R., Zhou, J., Ouyang, S., Wang, X., Zhang, H. Optimal operation of multi-reservoir system by multi-elite guide particle swarm optimization. International Journal of Electrical Power & Energy Systems, 2013; 48: 58–68. doi:10.1016/j.ijepes.2012.11.031.

[35] Raso, L., Bader, J.-C., Weijs, S. Reservoir operation optimized for hydropower production reduces conflict with traditional water uses in the Senegal River. Journal of Water Resources Planning and Management, 2020; 146: 05020003. doi:10.1061/(ASCE)WR.1943-5452.0001076.

[36] Luo, J., Qi, Y., Xie, J., Zhang, X. A hybrid multi-objective PSO–EDA algorithm for reservoir flood control operation. Applied Soft Computing, 2015; 34: 526–538. doi:10.1016/j.asoc.2015.05.036.

[37] Niu, W.-j., Feng, Z.-k., Liu, S. Multi-strategy gravitational search algorithm for constrained global optimization in coordinative operation of multiple hydropower reservoirs and solar photovoltaic power plants. Applied Soft Computing, 2021; 107: 107315. doi:10.1016/j.asoc.2021.107315.

[38] Li, F.-F., Qiu, J. Multi-objective optimization for integrated hydro–photovoltaic power system. Applied Energy, 2016; 167: 377–384. doi:10.1016/j.apenergy.2015.09.018.

[39] Bai, T., Wei, J., Chang, F.-J., Yang, W., Huang, Q. Optimize multi-objective transformation rules of water-sediment regulation for cascade reservoirs in the Upper Yellow River of China. Journal of Hydrology, 2019; 577: 123987. doi:10.1016/j.jhydrol.2019.123987.

[40] Kurek, W., Ostfeld, A. Multi-objective optimization of water quality, pumps operation, and storage sizing of water distribution systems. Journal of Environmental Management, 2013; 115: 189–197. doi:10.1016/j.jenvman.2012.11.030.

[41] Allawi, M. F., Jaafar, O., Mohamad Hamzah, F., Koting, S. B., Mohd, N. S. B., El-Shafie, A. Forecasting hydrological parameters for reservoir system utilizing artificial intelligent models and exploring their influence on operation performance. Knowledge-Based Systems, 2019; 163: 907–926. doi:10.1016/j.knosys.2018.10.013.

[42] Asadieh, B., Afshar, A. Optimization of water-supply and hydropower reservoir operation using the charged system search algorithm. Hydrology, 2019; 6: 5. doi:10.3390/hydrology6010005.

[43] He, Y., Xu, Q., Yang, S., Liao, L. Reservoir flood control operation based on chaotic particle swarm optimization algorithm. Applied Mathematical Modelling, 2014; 38: 4480–4492. doi:10.1016/j.apm.2014.02.030.

[44] Turgut, M. S., Turgut, O. E., Afan, H. A., El-Shafie, A. A novel Master–Slave optimization algorithm for generating an optimal release policy in case of reservoir operation. Journal of Hydrology, 2019; 577: 123959. doi:10.1016/j.jhydrol.2019.123959.

[45] Skardi, M. J. E., Kerachian, R., Abdolhay, A. Water and treated wastewater allocation in urban areas considering social attachments. Journal of Hydrology, 2020; 585: 124757. doi:10.1016/j.jhydrol.2020.124757.